

UNIVERSITY OF WARMIA AND MAZURY IN OLSZTYN

Technical Sciences

14(2)



PUBLISHER UWM

Editorial Board

Stefan Cenkowski (University of Manitoba, Canada), Adam Chrzanowski (University of New Brunswick, Canada), Davide Ciucci (University of Milan Bicocca), Janusz Laskowski (University of Agriculture in Lublin), Lech Tadeusz Polkowski (University of Warmia and Mazury in Olsztyn), Vladimir Tilipalov (Kaliningrad State Technical University, Russia), Alojzy Wasilewski (University of Warmia and Mazury in Olsztyn)

Editorial Committee

Marek Markowski (Editor-in-Chief), Piotr Artiemjew, Ireneusz Białobrzewski, Kamil Kowalczyk, Tomasz Lipiński, Wojciech Sobieski

Features Editors

Piotr Artiemjew, Ireneusz Białobrzewski, Leszek Kaczmarek, Waldemar Kamiński, Wojciech Sobieski

Statistical Editor

Paweł Drozda

Executive Editor

Mariola Jezierska

The Technical Sciences is indexed and abstracted in BazTech (<http://baztech.icm.edu.pl>)

The Journal is also available in electronic form on the web site
<http://wydawnictwo.uwm.edu.pl> (subpage *Czytelnia*)

The print edition is the primary version of the Journal

PL ISSN 1505-4675

© Copyright by Wydawnictwo UWM • Olsztyn 2011

Address

ul. Jana Heweliusza 14
10-718 Olsztyn-Kortowo, Poland
tel.: +48 89 523 36 61
fax: +48 89 523 34 38
e-mail: wydawca@uwm.edu.pl

Contents

Biosystems Engineering

W. Dudda – <i>Relationships between Geometric Parameters in Conical Rotary Graders</i>	135
--	-----

Civil Engineering

J. Kaczmarek, D. Leśniewska – <i>Modelling Events Occurring in the Core of a Flood Bank and Initiated by Changes in the Groundwater Level, Including the Effect of Seepage</i>	143
L.M. Kaczmarek, S. Sawczyński, J. Biegowski – <i>Bathymetry Changes and Sand Sorting During Sedimentation of Waterways. Part 1 – Conservation of Sediment Mass</i>	153
S. Sawczyński, L.M. Kaczmarek, J. Biegowski – <i>Bathymetry Changes and Sand Sorting During Sedimentation of Waterways. Part 2 – Modelling Versus Laboratory Data</i>	171
J. Pawłowicz, M. Świrydow, M. Adamczewska – <i>A Question of Building Materials and Construction Solutions for Revalorization of Frontage Townhouses in the Centre of Jeziorany</i>	193
M. Zagroba, M. Adamczewski, M. Czeberkus – <i>Revalorization of the Historic Town Centre of Jeziorany – Some Design-Related Problems</i>	205

Geodesy and Cartography

M. Bakula, R. Kaźmierczak, G. Grunwald – <i>Analysis of the Possibilities for Applying the Asg-Eupos System Services for Establishing the Detailed Control Networks</i>	217
R. Kaźmierczak, G. Grunwald, M. Bakula – <i>The use of RTCM 2.X Dekoder Software for Analyses of KODGIS and NAWGIS Services of the ASG-EUPOS SYSTEM</i>	229
K. Kowalczyk, J. Rapiński – <i>New Elaboration of Gradient Map of Vertical Crustal Movements in the Territory of Poland</i>	245
K. Kowalczyk, J. Rapiński – <i>Verification of Theoretical Phong Model in Reflector Less Surveys</i>	255
A. Łyszkwicz, A. Bernatowicz – <i>Statistical Analysis of the Fourth Precise Levelling Campaign in Poland</i>	263

Mechanical Engineering

M. Bramowicz – <i>Determination of Residual Pseudo-Chemical Energy and Energy Dissipative During Reversible Martensitic Transformation in $Ni_{52,2}Mn_{21,3}Ga_{26,5}$ Alloy</i>	279
S. Dominikowski, P. Bogacz – <i>Analysis and Comparison of a Joint Connecting Members in a Roof Truss</i>	287
W. Sobieski – <i>The Basic Equations of Fluid Mechanics in form Characteristic of the Finite Volume Method</i>	299
P. Szabracki, T. Lipiński, M. Bramowicz, K. Rychlik – <i>Influence Steel Manufacturing Process X2CrNiMoN25-7-4 on its Structure</i>	315

Spis treści

Inżynieria rolnicza

W. Dudda – Zależności między wielkościami geometrycznymi w stożkowych tryjerach obiegowych	135
--	-----

Inżynieria lądowa i wodna

J. Kaczmarek, D. Leśniewska – Modelowanie zjawisk zachodzących w korpusie wału przeciwpowodziowego pod wpływem zmian poziomu wód gruntowych z uwzględnieniem filtracji	143
L.M. Kaczmarek, Sz. Sawczyński, J. Biegowski – Zmiany batymetrii i segregacja osadów w procesie zapiaszczania torów wodnych. Część 1 – Zasada zachowania masy	153
S. Sawczyński, L.M. Kaczmarek, J. Biegowski – Zmiany batymetrii i segregacja osadów w procesie zapiaszczania torów wodnych. Część 2 – Porównanie wyników modelowania z wynikami pomiarów laboratoryjnych	171
J. Pawłowicz, M. Świrydow, M. Adamczewska – Materiałowo-konstrukcyjne aspekty rewaloryzacji zabudowy pierzejowej śródmieścia Jezioran	193
M. Zagroba, M. Adamczewski, M. Czeberkus – Problematyka rewaloryzacji zabudowy śródmieścia w Jezioranach – wybrane aspekty projektowe	205

Geodezja i kartografia

M. Bakula, R. Kaźmierczak, G. Grunwald – Analiza możliwości wykorzystania serwisów systemu asg-eupos do zakładania szczegółowych osnów geodezyjnych	217
R. Kaźmierczak, G. Grunwald, M. Bakula – Wykorzystanie autorskiego programu RTCM 2.X Dekoder do badań serwisów KODGIS i NAWGIS systemu ASG-EUPOS	229
K. Kowalczyk, J. Rapiński – Nowe opracowania mapy gradientów prędkości pionowych ruchów powierzchni skorupy ziemskiej na obszarze Polski	245
K. Kowalczyk, J. Rapiński – Weryfikacja teoretycznego modelu phonga w pomiarach bezlustrowych	255
A. Łyszczowicz, A. Bernatowicz – Statystyczna ocena dokładności czwartej kampanii niwelacji precyzyjnej w Polsce	263

Inżynieria mechaniczna

M. Bramowicz – Wyznaczenie resztkowej energii sprężystej oraz energii rozpraszanej podczas odwracalnej przemiany martenzytycznej w stopie $Ni_{52,2}Mn_{21,3}Ga_{26,5}$	279
S. Dominikowski, P. Bogacz – Analiza i porównanie połączenia prętów w węzle więzara kratowego dachowego	287
W. Sobieski – Podstawowe równania mechaniki płynów w formie charakterystycznej dla metody objętości skończonych	299
P. Szabracki, T. Lipiński, M. Bramowicz, K. Rychlik – Wpływ procesu wytwarzania stali X2CrNiMoN25-7-4 na jej budowę strukturalną	315

RELATIONSHIPS BETWEEN GEOMETRIC PARAMETERS IN CONICAL ROTARY GRADERS

Waldemar Dudda

Department of Mechanical Engineering and Machine Construction
University of Warmia and Mazury in Olsztyn

Key words: rotary grader, conical working surface, geometry.

Abstract

The objective of this study was to determine the formula for the radius describing the position of a point located on the conical working surface relative to the vertical axis of revolution in circular motion. Diagrams of conical working surface were presented, and a formula for the above radius was determined. The relationship was verified for randomly selected points on the conical surface, using a 3D model.

ZALEŻNOŚCI MIĘDZY WIELKOŚCIAMI GEOMETRYCZNYMI W STOŻKOWYCH TRYJERACH OBIEGOWYCH

Waldemar Dudda

Katedra Mechaniki i Podstaw Konstrukcji Maszyn
Uniwersytet Warmińsko-Mazurski w Olsztynie

Słowa kluczowe: tryjer obiegowy, stożkowa powierzchnia robocza, geometria.

Abstrakt

Praca dotyczy wyznaczenia zależności na promień położenia punktu znajdującego się na stożkowej powierzchni roboczej względem pionowej osi obrotu w ruchu obiegowym. Przedstawiono schematy stożkowej powierzchni roboczej i wyprowadzono ściśle zależność na wspomniany promień. Zweryfikowano uzyskaną zależność na modelu 3D dla dowolnie wybranych punktów leżących na powierzchni stożkowej.

Introduction

Cylinder graders, also known as trieurs, have been long used to remove impurities from grain. In the ongoing search for devices that deliver improved separating efficiency without a deterioration in separation quality, cylinders moving in circular motion were proposed (WIERZBICKI 1981, WIERZBICKI et al. 2000). As the structure of circular motion separators underwent further improvement, the cylindrical working surface was replaced with a horizontal surface in the shape of a beveled cone (JADWISIENCAK 2007). This solution is illustrated in Figure 1. The conical surface revolves around its own axis ξ with angular velocity ω_1 , and it also moves in circular motion in the horizontal plane around point O_2 (vertical axis z) with angular velocity ω_2 . The kinematics and dynamics of a particle of matter (e.g. grain seed – points B and B^* , Fig. 1) on the conical working surface can be determined based on radius R_β which describes the element's position (in circular motion) relative to axis z .

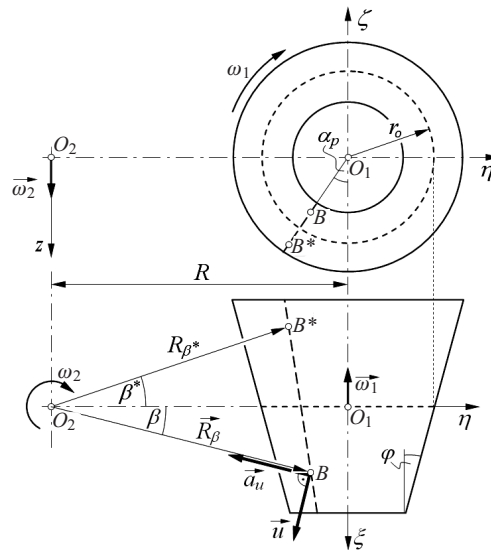


Fig. 1. Geometric parameters of a conical rotary grader

Point B moves in complex motion, therefore, its velocity \vec{v}_B and acceleration \vec{a}_B can be described by the following equations:

$$\vec{v}_B = \vec{u} + \vec{w}, \quad \vec{a}_B = \vec{a}_u + \vec{a}_w + \vec{a}_c \quad (1)$$

where:

\vec{u} – transport velocity,

\vec{w} – relative velocity,
 \vec{a}_u – acceleration of transport,
 \vec{a}_w – relative acceleration,
 \vec{a}_c – Coriolis acceleration.

At given operating parameters ($\omega_2 = \text{const.}$), the velocity and acceleration of transport (Fig. 1) will take on the following form:

$$\vec{u} = \vec{\omega}_2 \times \vec{R}_\beta, \quad \vec{a}_u = \vec{a}_u^n = \vec{\omega}_2 \times (\vec{\omega}_2 \times \vec{R}_\beta) \quad (2)$$

where:

\vec{a}_u^n – normal acceleration of transport (centripetal).

If $\vec{\omega}_2 \perp \vec{R}_\beta$, the velocity and acceleration of transport can be calculated based on the following scalar dependencies:

$$u = \omega_2 \cdot R_\beta, \quad a_u = (\omega_2)^2 \cdot R_\beta \quad (3)$$

In general, R_β should be a function of the grader's geometric parameters which define the position of point B on the conical surface. As shown in Figure 1, radius R_β should be determined by:

- radius R of cone's circular motion (distance between the cone's own axis of revolution ξ and axis z of circular motion),
- radius r_o of cone's intersection with plane $\eta\zeta$ w in mid-length,
- angle α_p at which a seed slides down the surface of the working element,
- angle φ between the cone's element and the cone's own axis of revolution ξ ,
- angle β between the radius of cone's circular motion and radius R_β .

In JADWISIEŃCZAK (2007), R_β has been incorrectly determined, therefore, the objective of this study was to determine the correct relationship describing radius R_β .

Figure 1 presents radii R_β and R_{β^*} and angles β and β^* describing the position of points B and B^* on the opposite sides of plane $\eta\zeta$ (intersecting the cone in mid-length). As demonstrated later, the relationships applicable to R_β and R_{β^*} will differ only in sign (+, -), therefore index (*) will not be used in successive parts of the study.

Geometric relationship

The input values were R , r_o , α_p , φ , β . The searched function will support the determination of the distance between point B and axis z , i.e. $R_\beta = f(R, r_o, \alpha_p, \varphi, \beta)$.

Figure 2 presents the geometric parameters required for determining radius R_β describing the position of point B situated in front of intersecting plane $\eta\zeta$.

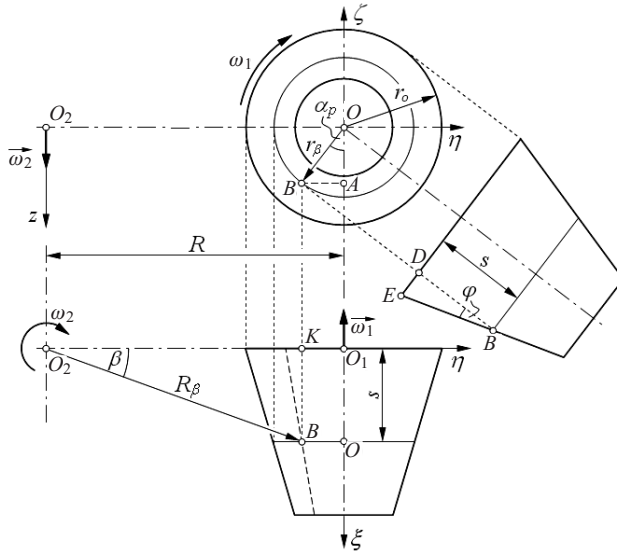


Fig. 2. Cone geometry in the part in front of intersecting plane $\eta\zeta$

Based on triangle EBD, we can deduce that:

$$\text{tg}\varphi = \frac{r_o - r_\beta}{s} \tag{4}$$

therefore, radius r_β describing the location of point B relative to the cylinder's own axis of revolution ξ can be presented as:

$$r_\beta = r_o - s \cdot \text{tg}\varphi \tag{5}$$

Triangle BKO₂ produces the following dependence:

$$s = R_\beta \sin \beta \tag{6}$$

When dependence (6) is substituted in equation (5), the result is:

$$r_\beta = r_o - R_\beta \sin \beta \text{tg}\varphi \tag{7}$$

As demonstrated by Figure 2, distance R between axis z of cylinder's circular motion and the cylinder's own axis of revolution ξ is equal to:

$$R = KO_2 + AB \quad (8)$$

Triangles BKO_2 and ABO produce the following equations:

$$KO_2 = R_\beta \cos \beta, \quad AB = r_\beta \sin \alpha_p \quad (9)$$

therefore, when equations (9) are substituted in formula (8), the result is:

$$R = R_\beta \cos \beta + r_\beta \sin \alpha_p \quad (10)$$

Dependence (7) is substituted in equation (10) to produce:

$$R = R_\beta \cos \beta + r_\beta \sin \alpha_p - R_\beta \sin \beta \operatorname{tg} \varphi \sin \alpha_p \quad (11)$$

After simple transformation, the result is a relationship between radius R_β and point B situated behind intersecting plane $\eta\zeta$:

$$R_\beta = \frac{R - r_o \sin \alpha_p}{\cos \beta - \sin \beta \operatorname{tg} \varphi \sin \alpha_p} \quad (12)$$

Figure 3 presents geometric parameters required for the determination of radius R_β for point B situated behind intersecting plane $\eta\zeta$. For this part of the cone, the following dependence is derived from triangle EBD :

$$\operatorname{tg} \varphi = \frac{r_\beta - r_o}{s} \quad (13)$$

therefore, radius r_β describing the location of point B relative to the cylinder's own axis of revolution ξ can be presented in the following form:

$$r_\beta = r_o + s \cdot \operatorname{tg} \varphi \quad (14)$$

A comparison of Figure 2 and Figure 3 indicates that equation (6) has an identical form in both cases. When equation (6) is substituted in dependence (14), the result is:

$$r_\beta = r_o + R_\beta \sin \beta \operatorname{tg} \varphi \quad (15)$$

Equations (8) and (9) also have an identical form in both cases (comparison of Fig. 2 and Fig. 3). Therefore, dependence (10) will not change, and when dependence (15) is substituted, the result is:

$$R = R_\beta \cos \beta + r_\beta \sin \alpha_p + R_\beta \sin \beta \operatorname{tg} \varphi \sin \alpha_p \tag{16}$$

After a simple transformation of equation (16), the result is a dependence between radius R_β and point B situated behind intersecting plane $\eta\zeta$:

$$R_\beta = \frac{R - r_o \sin \alpha_p}{\cos \beta + \sin \beta \operatorname{tg} \varphi \sin \alpha_p} \tag{17}$$

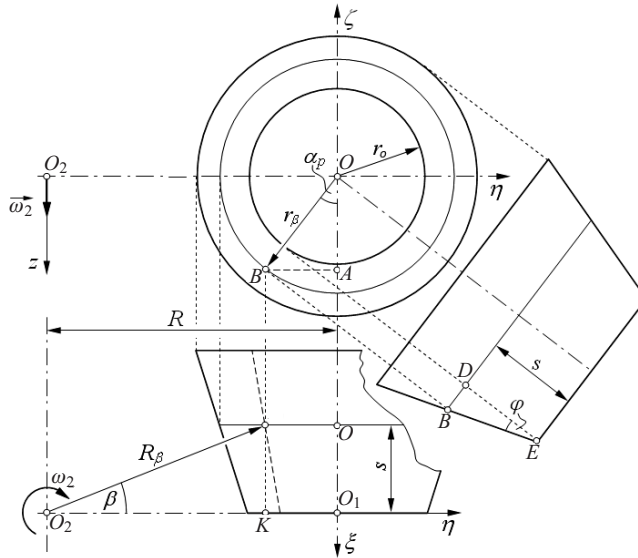


Fig. 3. Cone geometry in the part behind intersecting plane $\eta\zeta$

Equations (12) and (17) differ only in the sign ($-$, $+$) of the denominator. Therefore, both cases can be described by a shared dependence:

$$R_\beta = \frac{R - r_o \sin \alpha_p}{\cos \beta \pm \sin \beta \operatorname{tg} \varphi \sin \alpha_p} \tag{18}$$

Sign ($-$) applies to point B situated in front of intersecting plane $\eta\zeta$, whereas sign ($+$) applies to point B situated behind that plane.

Verification of relationship

A 3D model of the part of the cone in front of intersecting plane $\eta\zeta$ has been developed in the AutoCAD application (Fig. 2). The following model data were input: $R=1000$ mm, $r_o=200$ mm, height of beveled cone = 300 mm, radius of the smaller base = 100 mm (Fig. 4). Points B_1 and B_2 were mapped on the cone's lateral surface at two angles of α_p . Angles φ and β and the corresponding radii $R\beta$ were measured (Fig. 4), and the resulting values were presented in Table 1. The length of radii $R\beta$ determined based on dependence 12 is shown in the last column of Table 1.

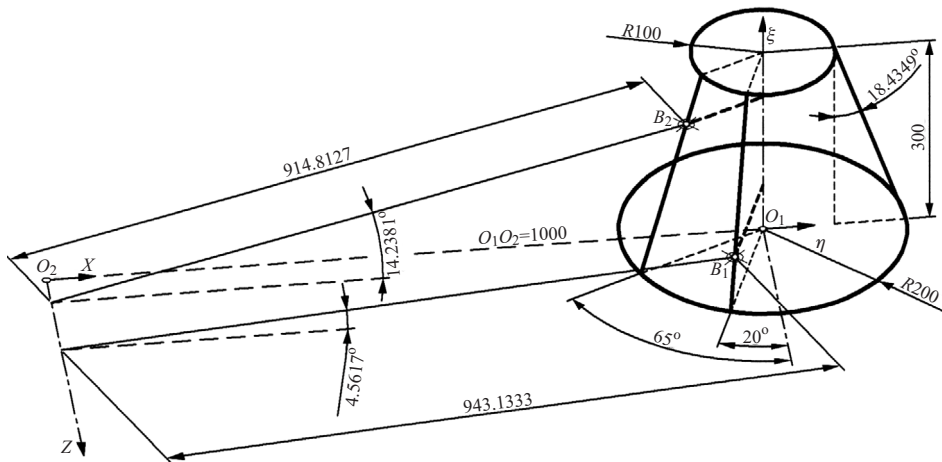


Fig. 4. A 3D model, radius and angle measurements

Geometric parameters for point B

Table 1

Point	Angle [°]			Radius R_β [mm]	
	α_p	φ	β	measured	based on (12)
B_1	20	18.4349	4.5611	943.1333	943.13326
B_2	65		14.2381	914.8127	914.81252

Conclusions

The relationship describing the distance between point B and axis z of cone's circular motion was determined in this study. In section 3, the formula (12) describing radius R_β was verified. The convergence between the measured

values of R_β and the values of R_β derived from equation (12) is determined solely by the rounding-off of the values of trigonometric functions of angles α_p , φ and β . Therefore, it can be concluded that equations (12) and (17) have been formulated correctly.

Translated by ALEKSANDRA POPRAWKA

Accepted for print 6.09.2011

References

- WIERZBICKI K. 1981. *Teoria zachowania się ziarna w cylindrze tryjera z dodatkowym ruchem po okręgu*. Zeszyty Naukowe ART w Olsztynie, Mech. i Bud., 13: 27–42.
- WIERZBICKI K., CHOSZCZ D., KONOPKA S. 2000. *Studies on the kinematics conditions of a cylindrical trieur set in additional rotary motion*. Technical Sciences, 3: 101–110.
- JADWISIEŃCZAK K. 2007. *Analiza procesu rozdziatu mieszaniny ziarnistej w stożkowym tryjerze obiegowym*. Rozprawa doktorska, Uniwersytet Warmińsko-Mazurski w Olsztynie, pp. 1–97.

**MODELLING EVENTS OCCURRING IN THE CORE
OF A FLOOD BANK AND INITIATED BY CHANGES
IN THE GROUNDWATER LEVEL, INCLUDING
THE EFFECT OF SEEPAGE**

Jarosława Kaczmarek¹, Danuta Leśniewska²

¹ Chair of Civil Engineering and Building Constructions
University of Warmia and Mazury in Olsztyn

² Division of Geotechnics
University of Technology in Koszalin

Key words: flood banks, changes in groundwater levels, water seepage, FEM modelling.

A b s t r a c t

The paper presents results of numerical modelling of the response of a flood bank to the rising or lowering water table. The modelling was performed with the finite element method (FEM) in two variants: excluding the effect of groundwater seepage through the flood bank (PLAXIS v. 8) and including groundwater seepage during intervals between increments in the height of the groundwater table (PLAXIS 2D 2010 with a FLOW model).

**MODELOWANIE ZJAWISK ZACHODZĄCYCH W KORPUSIE
WAŁU PRZECIWPOWODZIOWEGO POD WPLYWEM ZMIAN POZIOMU WÓD
GRUNTOWYCH Z UWZGLĘDNIENIEM FILTRACJI**

Jarosława Kaczmarek¹, Danuta Leśniewska²

¹ Katedra Budownictwa i Konstrukcji Budowlanych
Uniwersytet Warmińsko-Mazurski w Olsztynie

² Katedra Geotechniki
Politechnika Koszalińska

Słowa kluczowe: wały przeciwpowodziowe, zmiany poziomu wód gruntowych, przepływ wody w gruncie, modelowanie MES.

A b s t r a k t

W pracy przedstawiono wyniki modelowania numerycznego zachowania się wału przeciwpowodziowego w trakcie podnoszenia i obniżania zwierciadła wody. Modelowanie przeprowadzono metodą elementów skończonych (MES) w dwóch wariantach: bez uwzględnienia przepływu wody w gruncie (PLAXIS wersja 8) oraz z uwzględnieniem przepływu wód gruntowych w okresach między przyrostami wysokości zwierciadła wody (PLAXIS 2D 2010 z modułem FLOW).

Introduction

Understanding and modelling events which occur in the core of a flood bank caused by fluctuations in the groundwater level is the first step towards predicting changes inside flood banks due to different hydrometeorological conditions. In 2008, under the framework of the Scientific Network called *Transport of sediments and contaminants and degradation of environment in rivers, river mouths and marine coastal areas* (TROIANet) and in collaboration with the Institute of Hydroengineering of the Polish Academy of Sciences in Gdańsk, experimental tests on a physical model of the riverward slope of a levee were carried out, including studies on changes in the core of the flood bank caused by rising and lowering the groundwater table level (KACZMAREK, LEŚNIEWSKA 2010, LEŚNIEWSKA, KACZMAREK 2010). These studies were a continuation of some earlier research, completed under the EU 6th Framework Research Project FLOODsite, carried out in 2006–2009 (LEŚNIEWSKA et al. 2007, KACZMAREK et al. 2009), which demonstrated that changes in the groundwater table level could lead to alterations in the structure of a levee, which in extreme cases – alongside other modifications due to such external events as atmospheric precipitation, changing water levels in rivers and water reservoirs protected by flood embankments, might cause levee failure or damage. The current physical experiments on a model of a flood bank are carried out at the Institute of Hydroengineering in Gdańsk under the research project NN 506317039 called *Studies on changes in the microstructure of ground and its influence on processes of water flow and contamination transport in flood banks*.

The preliminary results of the numerical modelling of deformations in a flood embankment under the effect of changing groundwater levels have been presented in the papers by KACZMAREK, LEŚNIEWSKA (2010) and LEŚNIEWSKA, KACZMAREK (2010).

The analysed case

The numerical analysis was carried out for the conditions transferred from one of the experimental tests, in which an incremental rise and fall in the groundwater level were investigated. A change in the groundwater level was constant and equalled ± 20 cm. This case was discussed in some earlier articles, e.g. KACZMAREK, LEŚNIEWSKA 2010, LEŚNIEWSKA, KACZMAREK 2010, except that the previous numerical modelling executed with the software package PLAXIS (version 8) could not take into account the fact that as the water table outside the flood bank rises, it begins to flow through the ground (seepage). This flow

occurs in a finite time and does not stop until the new level of groundwater, which corresponds to the set level of water inside the core of the flood bank, stabilises.

The paper presents results of modelling changes occurring in the core of a levee caused by fluctuations in the level of groundwater – rising or lowering the table groundwater by 20 cm. Based on the model studies, it has been assumed that the final level of groundwater stabilises in five days. Including groundwater seepage in the numerical analysis was possible owing to the FLOW module, dedicated to studying water flow in ground. This model is compatible with the programme PLAXIS (v. 2D 2010). The analysis started with the simplest case – it was assumed that a change in the groundwater table at a given point occurred in a linear fashion, according to the formula:

$$y(t) = y_0 + \Delta y \cdot \frac{t}{\Delta t},$$

where,

y_0 – the current groundwater level for each stage of modelling, in meters,

Δy – a rise or fall in the water level in a set time; in this paper, $\Delta y = \pm 0.2$ m and was identical for all stages of calculations,

Δt – the time interval set for the calculations, during which the assumed change in the groundwater level occurs; in this paper Δt is 5 days, and it was constant for all stages of the calculations.

The numerical simulation was conducted via application of a network of triangular elements with 15 nodes (3 external and 12 internal), which is generated automatically by the PLEXIS programme. The minimum value of the ground compactness was assumed as 0.1 kPA, whereas the other parameters of the materials corresponded to the actual ones, obtained in laboratory analyses of the sand sampled in Lubiatowo, which was used to construct

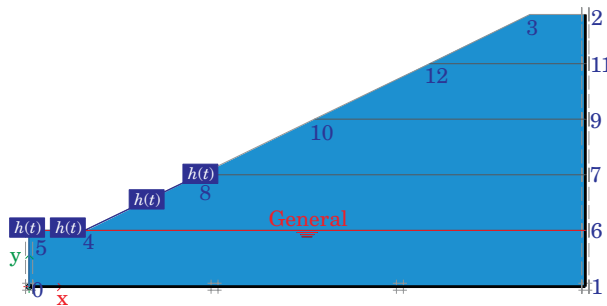


Fig. 1. Impervious boundaries taken for modelling a water flow

the physical model (KACZMAREK, LEŚNIEWSKA 2010, LEŚNIEWSKA, KACZMAREK 2010). In Fig. 1, the thick black line shows the limits of impervious ground as assumed for the modelling.

Analysis of displacement fields

Total displacement fields and maximum values of these displacements obtained from the numerical modelling with the FLOW module and linearly time-changeable water flow in the ground are distinctly different from the ones produced by earlier analyses, in which water seepage was not included (LEŚNIEWSKA, KACZMAREK 2010).

First of all, a change in the directions of displacement resultants is visible in the first phase of the experiment, when the groundwater level was gradually raised, especially during the first stages of this phase (0–20 cm; 20–40 cm) (Fig. 2a and 2b as well as Fig. 2f and 2g). When the groundwater table was raised by steps (with no seepage in the ground), total displacements were directed vertically upwards and their maximum values were contained in the range $[2.37 \cdot 10^{-6} \text{ m}; 40.77 \cdot 10^{-6} \text{ m}]$ (Tab. 1, Fig. 2a–2e). In the analysed case, on the assumption that the water flow is changing linearly, the direction of total displacements for the first stages of groundwater rising is horizontal in the whole area (Fig. 2f and 2g), but for the other three stages (Fig. 2h, 2i and 2j) of the phase when the groundwater table is rising, directions of total displacements are comprised within the range of angles (270° , 360°). It seems that the horizontal direction of displacements is a result of the dominant horizontal water flow component, which appears in the first stages of phase I of the experiment. Inclusion of water seepage caused simultaneous increase of the maximum values of total displacements, which in this case are in the range of $[37.23 \cdot 10^{-6} \text{ m}; 49.65 \cdot 10^{-6} \text{ m}]$, and their detailed values for particular stages of our calculations have been collected in Table 1.

Table 1
Maximum total displacements u calculated for the phase of groundwater table lifting

Groundwater level [m]	Without seepage u [10^{-6} m]	With seepage u [10^{-6} m]
0–0.2	2.37	37.23
0.2–0.4	7.40	37.49
0.4–0.6	16.19	39.39
0.6–0.8	29.06	45.25
0.8–1.0	40.77	49.65

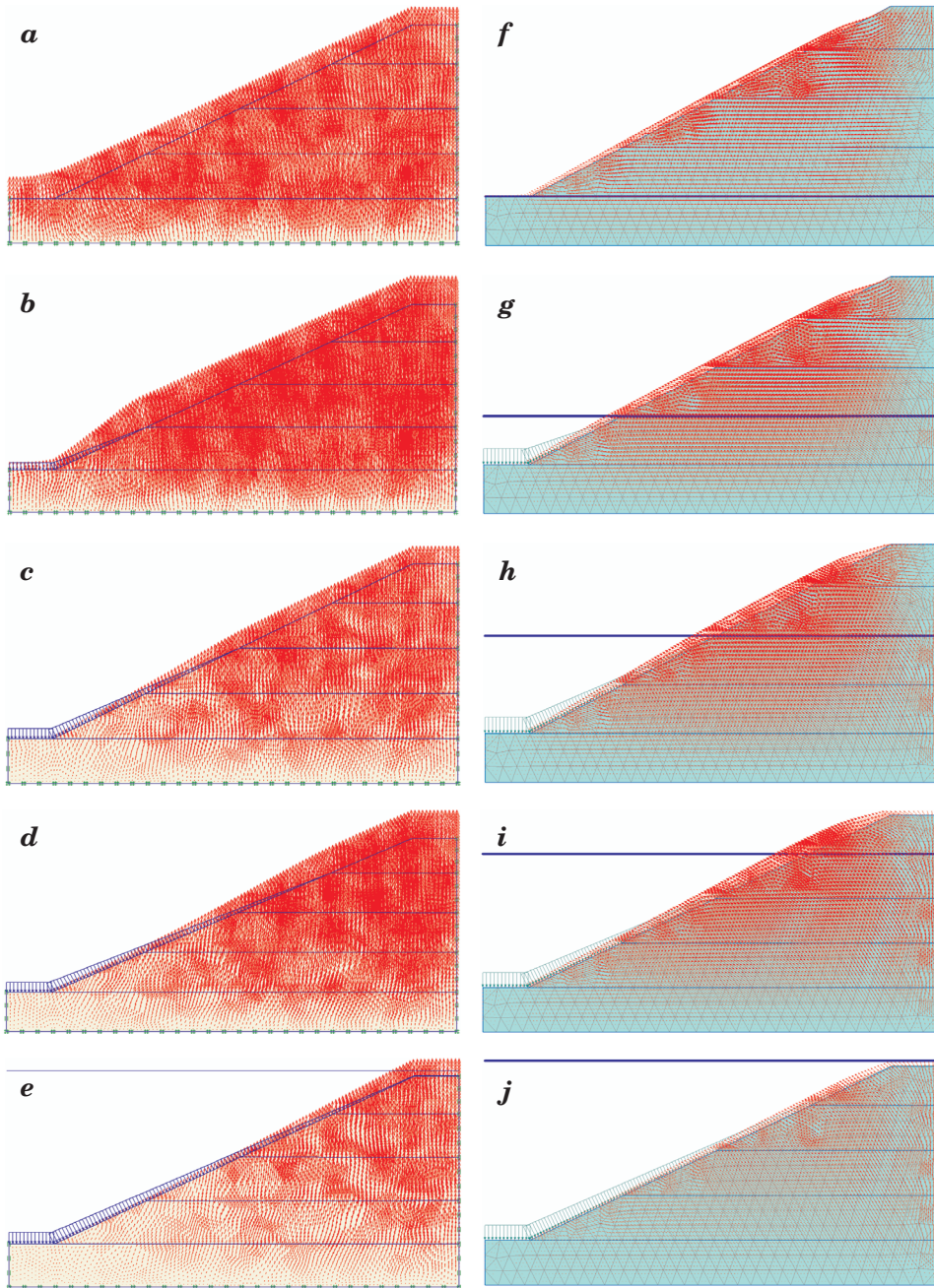


Fig. 2. Total displacements for the water level rising phase. A case of stepwise increase in water table *a-e*, displacements multiplied by 1,000. A case of linearly changing water flow *f-j*, displacements multiplied by 500

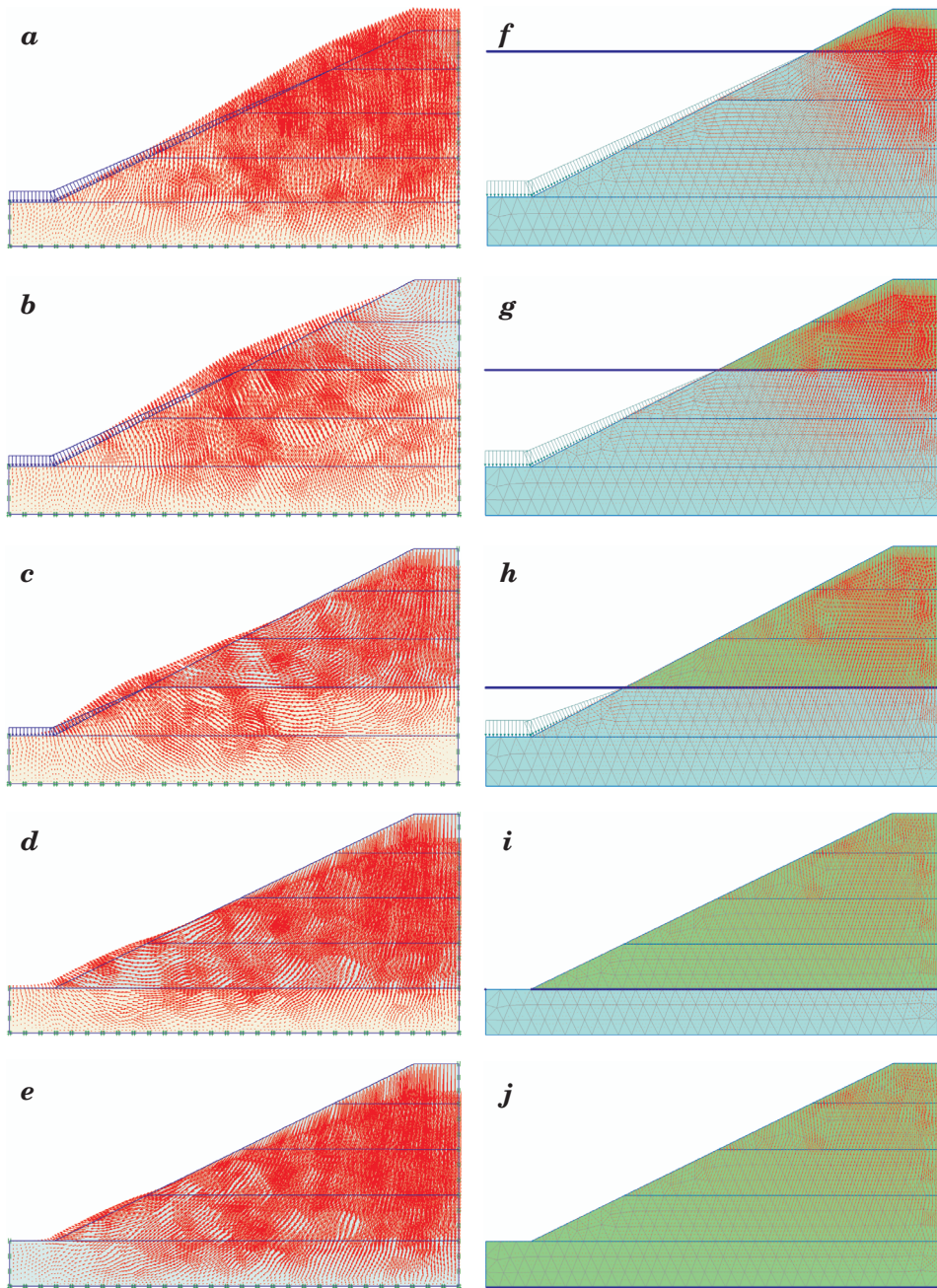


Fig. 3. Total displacements for the water level rising phase. A case of stepwise increase in the water table level *a-e*, displacements multiplied by 1,000. A case of linearly changing water flow *f-j*, displacements multiplied by 500

In the second phase of the experiment, in which the groundwater table was lowered for five days, by 20 cm each time, and the linearly time-dependent changeable water seepage through the ground was included, total displacement fields (Fig. 3f–3j) attained a similar pattern of distribution as when water seepage was not considered in the calculations (Fig. 3a–3e). Both cases, however, are considerably different from each other in the values of maximum displacements, which are in the range of $[20.66 \cdot 10^{-6} \text{ m}; 71.52 \cdot 10^{-6} \text{ m}]$ (Table 2) for the scenario without water seepage through the ground.

Table 2
Maximum total displacements u calculated for the phase of groundwater level lowering

Groundwater level [m]	Without seepage u [10^{-6} m]	With seepage u [10^{-6} m]
1.0–0.8	25.10	20.66
0.8–0.6	16.35	43.61
0.6–0.4	19.41	59.47
0.4–0.2	28.48	68.55
0.2–0	31.44	71.52

It is evident that the inclusion of the simplest scenario of water flow through the ground (stationary in space with linear changeability in time) causes bigger strains inside the flood bank (dislocation of ground) during the phase of both groundwater rising and falling.

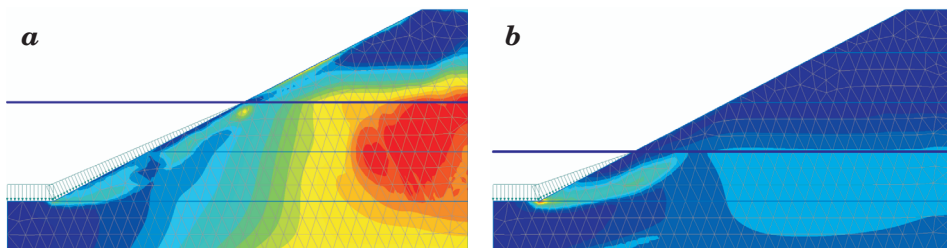


Fig. 4. Increments of non-dilatational strains corresponding to the water level: a – decreasing the water level from 0.8 m to 0.6 m, b – decreasing the water level from 0.6 m to 0.4 m

Besides, in both stages of the groundwater falling phase, we can observe some residual, not fully developed slip lines. In the first stage (decrease from 0.8 to 0.6 m) we can observe localisation of strains, practically running along the borderline of the slope (Fig. 4a – maximum values of increments of strains appear in the area delineated by points (1,5; 0,6), (2,0; 0,65), (2,0; 0,25), (1,45; 0,25)). In the second stage (decrease from 0.6 to 0.4 m) – localisation begins at the toe of the slope and reaches the height of 40 cm (Fig. 4b). The highest values of strain increments are found in the area at the toe of the slope. The biggest changes in increments of non-dilatational strains were recorded for the stage of lowering the water table from 0.8 to 0.6 versus the stage from 0.6 to 0.4 m – between these stages, the above values changed from $1.7 \cdot 10^{-3} \%$ do $7.42 \cdot 10^{-3} \%$. This is more than double versus the case when no groundwater seepage through a levee is included in the analysis.

Analysis of stability

A possible mechanism causing damage to a flood bank was computed for particular stages of the experiment in both phases with the aid of the procedure called $c-\phi$ reduction, which is available in both versions of the programme PLAXIS (Fig. 5).

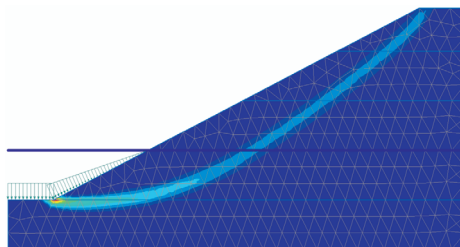


Fig. 5. A theoretical mechanism of damage to a flood bank corresponding to the stage of decreasing the water level from 0.6 m to 0.4 m

The analyses yielded identical values of stability factors for particular stages of the experiment with or without groundwater seepage (Fig. 4). This can possibly indicate that a flow of water through the levee which is relatively slow and linearly changing in time has no influence on the value of a stability factor although it affects the extent of deformation of the levee.

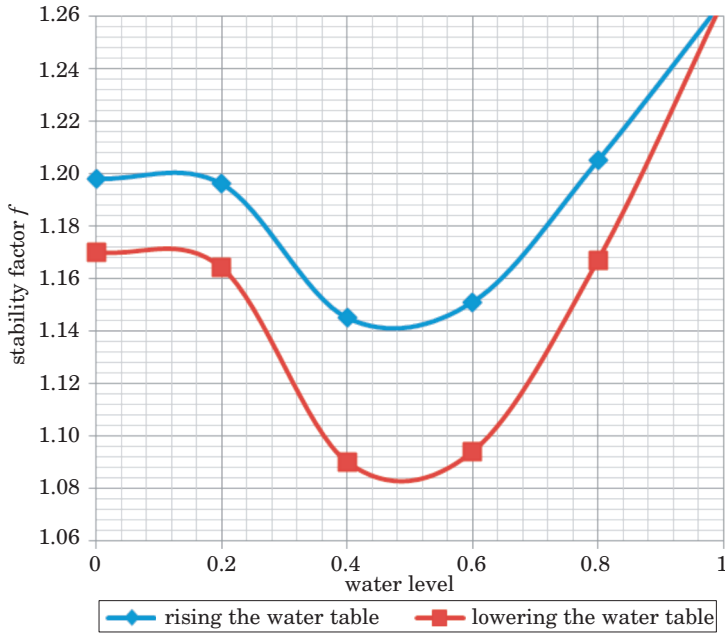


Fig. 6. The changing value of the stability factor of the levee's slope for both phases of the experiment: rising and lowering the water table

Conclusions

The present results of numerical modelling of linearly time-dependent changeable water flow through the ground are a further step in our attempt to reproduce numerically the results of the experiments conducted under the Research Network TROIANet and as part of the research project NN 506317039 *Studies on changes in the microstructure of ground and its influence on processes of water flow and contamination transport in flood banks*.

The paper compares results of numerical modelling with and without including a flow of water through the ground (a flow that changes linearly in time, at a constant time period assumed for establishing a stable groundwater level for all the stages). The results suggest that the adopted water flow model significantly changes directions of displacement in the first phase of water level rising, and that in all the stages of the analysed experiment it changes values of total displacements. However, the stability factors, computed for each stage of the experiment, do not change. In order to find out the best fit for the results of numerical modelling and physical experiment, it is necessary to verify more realistic water flow models and to determine which parameters are significant for the stability of a flood bank and which can be omitted.

Acknowledgement

The work described in this publication was supported by the Polish Ministry of Science and Higher Education through the grant to the budget of the Scientific Network “*TROIANet*”, Contract 57/E-84/BWSN-0114/2008 and through the research project Nr NN 506 31 70 39.

Translated by JOLANTA IDŹKOWSKA

Accepted for print 30.09.2011

References

- KACZMAREK J., LEŚNIEWSKA D. 2010. *A flood embankment under changing water level conditions – a comparison of a physical and a numerical model*. Technical Sciences, 13: 53–63.
- KACZMAREK J., BOGACZ P., LEŚNIEWSKA D. 2009. *Wpływ zmian położenia zwierciadła wody na deformacje wału przeciwpowodziowego*. Inżynieria i Budownictwo, 12: 679–680.
- LEŚNIEWSKA D., BOGACZ P., KACZMAREK J., ZARADNY H. 2007. *Air trapping phenomenon and cracking. FLOODsite. Raport T04 07*.
- LEŚNIEWSKA D., KACZMAREK J. 2010. *Wpływ zmian położenia zwierciadła wody na stateczność odwodnej skarpy wału przeciwpowodziowego – modelowanie fizyczne i numeryczne*. Inżynieria Morska i Geotechnika, 6: 719–723.
- PLAXIS 2D 2010 – Podręcznik użytkownika.

**BATHYMETRY CHANGES AND SAND SORTING
DURING SEDIMENTATION OF WATERWAYS.
PART 1 – CONSERVATION OF SEDIMENT MASS**

***Leszek M. Kaczmarek^{1,2}, Szymon Sawczyński²,
Jarosław Biegowski¹***

¹ Institute of Hydroengineering, Polish Academy of Sciences in Gdańsk

² The Chair of Civil Engineering and Building Structures
University of Warmia and Mazury in Olsztyn

Key words: sediment transport, conservation of sediment mass, bathymetry changes, sediment velocity, silting up.

A b s t r a c t

In this paper, an equation has been derived from the principle of mass conservation which enables us to produce mathematical description of changes in the seabed bathymetry in time and space. A detailed analysis of this equation has been made in the context of dependence between transport intensity and thickness of densely packed sand grains in sediment being in motion. For the condition when sediment transport is in hydrodynamic equilibrium, i.e. when the flux of sediments falling on the bed is offset by the flux of sediments lifted from the bed, it has been suggested to describe this dependence in the form of a linear function, a proposal which later was verified experimentally. In the mathematical description of changes in the seabed bathymetry, a clear distinction has been made between sediment transport in the positive, onshore direction and transport in the negative, offshore direction, associated, respectively, with sediment transport during the wave crest and wave trough phases.

**ZMIANY BATYMETRII I SEGREGACJA OSADÓW W PROCESIE ZAPIASZCZANIA
TORÓW WODNYCH. CZĘŚĆ 1 – ZASADA ZACHOWANIA MASY**

Leszek M. Kaczmarek^{1,2}, Szymon Sawczyński², Jarosław Biegowski¹

¹ Instytut Budownictwa Wodnego PAN w Gdańsku

² Katedra Budownictwa i Konstrukcji Budowlanych
Uniwersytet Warmińsko-Mazurski w Olsztynie

Słowa kluczowe: transport osadów, zasada zachowania masy, zmiany batymetrii, prędkość rumowiska, zapiaszczanie.

Abstrakt

Na podstawie zasady zachowania masy wyprowadzono równanie służące do matematycznego opisu zmian batymetrii dna w czasie i przestrzeni. Szczegółowo przeanalizowano równanie ze względu na zależność między natężeniem transportu a miąższością gęsto upakowanych ziaren będącego w ruchu rumowiska. Dla warunku, kiedy transport osadu znajduje się w równowadze hydrodynamicznej, tj. kiedy strumień osadów opadających na dno jest równoważony strumieniem osadów podrywanych z dna, zaproponowano opis tej zależności w postaci funkcji liniowej, którą następnie potwierdzono wynikami z eksperymentu laboratoryjnego. Przedyskutowano także efekty związane z nieliniową postacią tej zależności. W opisie matematycznym zmian batymetrii dna wyraźnie podzielono transport osadów na transport w kierunku dodatnim – dobrzegowym, i ujemnym – odrzegowym, związany z transportem rumowiska odpowiednio w fazie grzbietu i doliny fali.

Introduction

It is extremely important to predict accurately bathymetric changes in the seabed near an approach canal to a harbour so as to be able to maintain its navigable depth. Changes in the bathymetry of the seabed in time and space are usually described using equations derived from the principle of mass conservation.

The review written by NICHOLSON et al. (1997) states that morphodynamic models use classical shock capturing schemes for bed level simulations. JOHNSON and ZYSERMAN (2002) applied a modified second-order accurate Lax-Wendroff scheme. This scheme, however, is burdened with a numerical dispersion error, which is reflected by additional oscillations in the results of numerical calculations. As JOHNSON and ZYSERMAN showed (2002), spatial oscillations generated by numerical schemes are caused by the dependence of the celerity of the bed level oscillations on the bed level, which are a result of the non-linear relationship between the sediment transport rate and the bed level.

Some of the numerical schemes applied to simulation of changes in the bed level have been discussed by LONG et al. (2008), who analyzed the accuracy and stability of these schemes. Their discussion seems to suggest that the best scheme for simulation of sediment transport is a fifth-order Euler-Weno scheme, which relies on the upwinding concept, also implemented in this paper. The Euler-Weno scheme is shown to have significant advantages over schemes with artificial viscosity and filtering process. It is highly recommended especially for phase-revolving sediment transport models, when the sediment transport rate is postulated to be split into parts associated with the bedform propagation in the positive and negative x -directions.

This paper suggests that there is a linear relationship between the sediment transport rate and the thickness of the layer of densely packed, moving sand grains, which consequently enables us to apply the first-order upwind

scheme for solving an equation which describes changes in the seabed bathymetry in time and space. Moreover, additional effects connected with the non-linearity of this dependence are discussed. Noteworthy is the suggestion that there is a linear relationship between sediment transport and the bed level. The latter relationship continues to be viewed as a non-linear one.

Part 2 of the article describes a three-layer model of transport of sediments with sand grains of various size, derived by KACZMAREK (1999) from the principle of the conservation of water and sediment flow in the nearbed layer. It has been demonstrated that this model is applicable (alongside the equation derived from the mass conservation principle, described in this part) to mathematical description of changes in bathymetry and changes in the distribution of grain size composition of sediments which constitute the seabed near an approach waterway to a harbour under given wave and current conditions.

Conservation of sediment mass

Using Euler coordinates, a continuity equation derived from the mass conservation principle is determined for control volume V limited by closed control space A . The amount of mass contained in the thus determined, immobile space can change in time due to a sediment flow through the control space (cf., for example, MITOSEK, 2001, PUZYREWSKI, SAWICKI, 2000). A change in the mass enclosed in the V space, dependent on the change in the density ρ_r of sediment (treated as fluid) in time dt , equals:

$$\iiint_V \frac{\partial \rho_r}{\partial t} dt dV \quad (1)$$

where

$$\rho_r = \rho_s C \quad (2)$$

$$\rho_s = \frac{m_s}{V_s} \quad (3)$$

$$C = \frac{V_s}{V_p + V_s} \quad (4)$$

$$\rho_r = \rho_s C = \frac{m_s}{V_s} \frac{V_s}{V_p + V_s} = \frac{m_s}{V_p + V_s} \quad (5)$$

In dependences (1)-(5), the following denotations were introduced:

ρ_s – ground skeletal density [kg/m³],

C – volume concentration [m³/m³],

m_s – ground skeletal mass [kg],

V_s – ground skeletal volume [m³],

V_p – volume of pores [m³].

The mass of sediment which flowed though surface A in a given time, equal to the difference in the mass flowing into the control volume and flowing out of that volume, is:

$$-\iint \rho_r \mathbf{u} d\mathbf{A} dt = -\iint \rho_r u_n dA dt \quad (6)$$

where

$d\mathbf{A}$ is a vector of the value equal to the dA field, normal to this surface and oriented outside the area.

Should the sign “minus” be omitted, the integral would signify the loss of sediment from control volume V . The scalar product of the velocity vector and surface vector is equal to the product of the component velocity u_n normal to this surface and the field of an area dA .

Having compared the expressions (1) and (6) and after simplification by dt , the general, integral form of the continuity equation is obtained:

$$\iiint_V \frac{\partial \rho_r}{\partial t} dV + \iint_A \rho_r u_n dA = 0 \quad (7)$$

From dependence (2) and assuming that $\rho_s = \text{const.}$, equation (7) can be transformed to:

$$\iiint_V \frac{\partial C}{\partial t} dV + \iint_A C u_n dA = 0 \quad (8)$$

When including Gauss-Ostrogradsky theorem, the following form of the continuity equation is obtained:

$$\iiint_V \frac{\partial C}{\partial t} dV + \iint_A \text{div}(C\mathbf{u}) dV = 0 \quad (9)$$

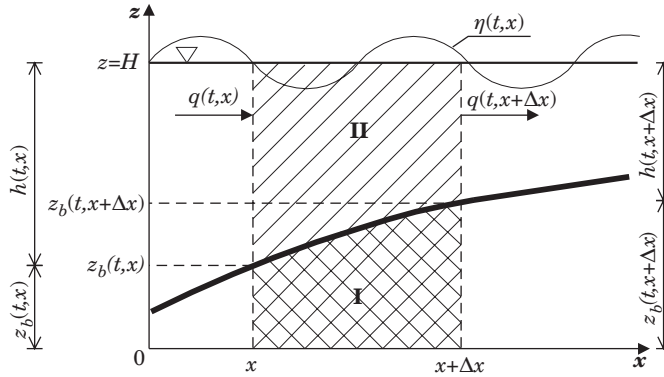


Fig. 1. Diagram of the analyzed area

Next, assuming the control volume as shown in Figure 1, i.e. analyzing the plane bed concept, and assuming the constant level of filling up $H = \text{const.}$, and bearing in mind that $z_b + h = H$, one can obtain:

$$\int_0^{\Delta x} dx \left[\int_0^H \frac{\partial C}{\partial t} dz + \int_0^H \frac{\partial}{\partial x} (Cu) dz \right] = 0 \quad (10)$$

which can be rewritten as:

$$\int_0^H \frac{\partial C}{\partial t} dz + \int_0^H \frac{\partial}{\partial x} (Cu) dz = 0 \quad (11)$$

In the motion of water caused by surface waves $\eta(t,x)$, instantaneous values of the velocity and concentration, in Euler's set, can be written in the following form:

$$u = \langle u \rangle + \tilde{u} \quad (12)$$

$$C = \langle C \rangle + \tilde{C} \quad (13)$$

where

$\langle \dots \rangle = \frac{1}{T} \int_0^T (\dots) dt$ is the averaged value in a wave period (T) whereas \tilde{u} and \tilde{C} stand for the oscillation component of, respectively, velocity and concentration.

By substituting dependences (12) and (13) to equation (11), and then averaging this equation over a wave period, the following is obtained:

$$\int_0^{\eta} \frac{\partial \langle C \rangle}{\partial t} dz + \int_0^{\eta} \frac{\partial}{\partial x} (\langle u \rangle \langle C \rangle + \langle \tilde{u} \tilde{C} \rangle) dz = 0 \quad (14)$$

Taking into consideration that:

$$\frac{\partial}{\partial x} \langle \tilde{u} \tilde{C} \rangle = U_s \frac{\partial \langle C \rangle}{\partial x} \quad (15)$$

where

U_s is known under the name of Stokes drift (cf. FREDSE and DEIGAARD 1992) and

$$U_L = \langle u \rangle + U_s \quad (16)$$

where

U_L is the Lagrangian-type averaged velocity, equation (14) can be rewritten to:

$$\int_0^{\eta} \frac{\partial \langle C \rangle}{\partial t} dz + \int_0^{\eta} \frac{\partial}{\partial x} (U_L \langle C \rangle + \langle \tilde{u} \tilde{C} \rangle) dz = 0 \quad (17)$$

on the assumption that when there are no vertical currents, by virtue of the mass conservation equation for water $\frac{\partial}{\partial x} U_L = 0$.

Assuming that the vast majority of sediment is transported near the bed as bedload and sheet flow, respectively, and assuming that for $z = \eta$ concentration $\langle C \rangle$ is negligibly small, equation (17), according to Leibniz integration law, can be written as:

$$\frac{\partial}{\partial t} \int_0^{\eta} \langle C \rangle dz + \frac{\partial}{\partial x} \int_0^{\eta} (U_L \langle C \rangle) dz = 0 \quad (18)$$

Solving equation (18) for the control volume as in Figure 1, we obtain:

$$\frac{\partial}{\partial t} \int_0^{z_r} \langle C^I \rangle dz + \frac{\partial}{\partial t} \int_{z_r}^{\eta} \langle C^{II} \rangle dz + \frac{\partial}{\partial x} \int_0^{z_r} (U_L^I \langle C^I \rangle) dz + \frac{\partial}{\partial x} \int_{z_r}^{\eta} (U_L^{II} \langle C^{II} \rangle) dz = 0 \tag{19}$$

where:

- z_r – reference level and in Fig. 1 it was assumed to be at the bed level $z_b = z_r$, although obviously another choice is possible, too,
- U_L^I, C^I – sediment velocity and concentration in the sub-layer I (Fig. 1), respectively,
- U_L^{II}, C^{II} – sediment velocity and concentration in the sub-layer II (Fig. 1), respectively.

From equation (19) it can be concluded that the total sediment transport concentration per volume can be described with the following relationship:

$$\int_0^{z_r} C^I U_L^I dz + \int_{z_r}^{\eta} C^{II} U_L^{II} dz = q(t, x) \tag{20}$$

which means that equation (19) can be rewritten to the form:

$$\frac{\partial}{\partial t} \int_0^{z_r} C^I dz + \frac{\partial}{\partial x} \int_{z_r}^{\eta} C^{II} dz + \frac{\partial q}{\partial x} = 0 \tag{21}$$

Should we assume that the sediment concentration $C^I = (1 - n_p)$ in the layer $0 \leq z \leq z_r$ is constant, then for $z_r = z_b$ from equation (21) we obtain:

$$(1 - n_p) \frac{\partial z_b}{\partial t} + \frac{\partial}{\partial t} \int_{z_b}^{\eta} C^{II} dz + \frac{\partial q}{\partial x} = 0 \tag{22}$$

where

$$n_p = \frac{V_p}{V_p + V_s} \tag{23}$$

denotes the porosity of sediment.

Equation (22) can be named the equation of sediment transport. It can be a useful mathematical tool for describing bathymetric changes of the seabed in time and space. As shown above, the transport equation was derived from the mass conservation principle. The expression $(1 - n_p) z_b + \int_{z_b}^{\eta} C^H dz$ corresponds quantitatively to the total volume of sediment per level surface unit of the sediment lying on the bed (first component of the expression) or suspended (second component). If the volume of the suspended sediment can be omitted, then equation (22) can be written as:

$$\frac{\partial z_b}{\partial t} + \frac{1}{(1 - n_p)} \frac{\partial q}{\partial x} = 0 \quad (24)$$

Sediment transport in equilibrium with load hydrodynamics

As mentioned before, in our discussion on the sediment transport equation, the bed level is usually taken as a reference level, which means that $z_r = z_b$. Of course, it is possible to take another level for reference. In this paper, for example, it is proposed to assume that $z_r = z_m$, where z_m stands for the thickness of densely packed sand grains in sediment which is moving.

Because it is assumed that intensive transport of sediment takes place during a storm, it can be expected that under such hydrodynamic conditions the bed remains flat (devoid of any bed forms) and locally horizontal. In this case, the value z_b can be replaced by z_m , which denotes the thickness of the layer of densely packed sand grains of moving sediment. The propagation velocity of this layer should not depend on the value of z_m because concentration $(1 - n_p)$ in the layer of densely packed sand grain in the moving sediment is constant. As demonstrated by KACZMAREK and OSTROWSKI (2002), in the layer of sediment where the velocity of the transported sediment is a function of the depth, the concentration also depends on the depth coordinate z .

Let z_m^+ and z_m^- stand, respectively, for the thickness of the cells $z_m^+ \times dx^+ \times 1$ and $z_m^- \times dx^- \times 1$, which are eroded from the profile transverse to the shore (direction x) in time dt due to the transport of sediment q_x^+ and q_x^- directed, respectively, on- and offshore:

$$z_m^+ = \frac{1}{(1 - n_p)} \frac{q_x^+ \cdot dt}{dx^+} \quad (25)$$

$$z_m^- = \frac{1}{(1 - n_p)} \frac{q_x^- \cdot dt}{dx^-} \quad (26)$$

where

$$z_m = z_m^+ + z_m^- \tag{27}$$

and

$$z_b(x,t + dt) = z_b(x,t) + \frac{\partial z_m}{\partial t} dt \tag{28}$$

The equilibrium conditions appear in the whole area of cells except near their edges. It can be assumed that the total amount of the sediment in motion, dragged or suspended (mainly in the contact layer near the bed) is picked up directly from the bed and equals the amount of the sediment moving in the bed as densely packed grains. It also means that sediment transport promptly adjust itself to the flow conditions and, therefore, the bed “responds” immediately to the given hydrodynamic conditions.

The following assumptions are derived:

$$1. \text{ for } 0 \leq z \leq z_m \left\{ \begin{array}{l} (1 - n_p) = \langle C^I \rangle \\ U_L^I = U_{L_1} \end{array} \right. \tag{29}$$

2. for $z_m < z \leq \eta$ we can write:

$$\int_{z_m}^{\eta} U_L \langle C \rangle dz = \bar{U}_L \int_{z_m}^{\eta} \langle C \rangle dz = U_{L_1} \int_{z_m}^{\eta} \kappa \langle C \rangle dz = U_{L_1} \int_{z_m}^{\eta} \langle C_1 \rangle dz = \int_{z_m}^{\eta} U_L^II \langle C^II \rangle dz \tag{30}$$

where

$$\frac{\bar{U}_L}{U_{L_1}} = \kappa \text{ and } \langle C_1 \rangle = \kappa \langle C \rangle \tag{31}$$

From the relationship (30), it can be concluded that:

$$U_L^II = U_{L_1} \text{ and } \langle C^II \rangle = \langle C_1 \rangle \tag{32}$$

At this point, it is worth noticing that progressive speed U_{L_1} is identifiable with the speed of propagation of the mass centre of a bed form z_m thick, which is moving but not changing its shape under the effect of the surface transport of sediment at speed \bar{U}_L . This progressive motion of a bed form of the thickness z_m can be compared to the movement of a sand dune, which is set in motion as a result of the surface motion of sand grains caused by a wind. The nature of this motion implies mixing of the grains involved in the motion and the ones

which are at rest in the bed layer of the thickness of $2z_m$ (KACZMAREK et al. 2004). It is so because as a flow of sediments fills up half the control volume of the length $dx/2$ during time dt , during the same time, a flow of sediment empties the other half of the control volume (likewise, of the length $dx/2$). If the bed level is to remain unchanged, for instance, than the flow entering the control volume and the flow leaving it should be equal. Thus, by virtue of equations (25) and (26), these flows, depending on the direction, are equal, respectively, $q_x^{+/-} dt = (1 - n_p) 2z_m^{+/-} dx^{+/-}/2$.

As the sediment transport is in equilibrium with load hydrodynamics, it is therefore postulated that:

$$(1 - n_p) z_m = \int_{z_m}^{\eta} \langle C_1 \rangle dz \quad (33)$$

Considering relationships (29) and (32), equation (19) can be presented as follows:

$$(1 - n_p) \frac{\partial z_m}{\partial t} + \frac{\partial}{\partial t} \int_{z_m}^{\eta} \langle C_1 \rangle dz + (1 - n_p) U_{L_1} \frac{\partial z_m}{\partial x} + U_{L_1} \frac{\partial}{\partial x} \int_{z_m}^{\eta} \langle C_1 \rangle dz = 0 \quad (34)$$

Next, by including relationship (33), we obtain:

$$2(1 - n_p) \frac{\partial z_m}{\partial t} + 2(1 - n_p) U_{L_1} \frac{\partial z_m}{\partial x} = 0 \quad (35)$$

which consequently leads to the following equations:

$$\frac{\partial z_m}{\partial t} + U_{L_1} \frac{\partial z_m}{\partial x} = 0 \quad (36)$$

and

$$\frac{\partial}{\partial t} \int_{z_m}^{\eta} \langle C_1 \rangle dz + U_{L_1} \frac{\partial}{\partial x} \int_{z_m}^{\eta} \langle C_1 \rangle dz = 0 \quad (37)$$

By including the decomposition of the velocity U_{L_1} into $U_{L_1}^+$ and $U_{L_1}^-$ and the thickness z_m into z_m^+ and z_m^- , the following can be obtained:

$$q_x^+ = (1 - n_p) U_{L_1}^+ z_m^+ = U_{L_1}^+ \int_{z_m^+}^{\eta} \langle C_1 \rangle^+ dz \quad (38)$$

$$q_x^- = (1 - n_p) U_{L_1}^- z_m^- = U_{L_1}^- \int_{z_m^-}^{\eta} \langle C_1 \rangle^+ dz \quad (39)$$

where

$$\langle \dots \rangle^+ = \frac{1}{T} \int_0^{T_c} (\dots) dt,$$

$$\langle \dots \rangle^- = \frac{1}{T} \int_{T_c}^T (\dots) dt,$$

T - wave period,

T_c - wave crest duration period.

By substituting relations (38) and (39) into equation (36), we obtain the following equations:

$$\frac{\partial z_m^+}{\partial t} + U_{L_1}^+ \frac{\partial z_m^+}{\partial x^+} = \frac{\partial z_m^+}{\partial t} + \frac{1}{(1 - n_p)} \frac{\partial q_x^+}{\partial x^+} = 0 \quad (40)$$

$$\frac{\partial z_m^-}{\partial t} + U_{L_1}^- \frac{\partial z_m^-}{\partial x^-} = \frac{\partial z_m^-}{\partial t} + \frac{1}{(1 - n_p)} \frac{\partial q_x^-}{\partial x^-} = 0 \quad (41)$$

Next, taking advantage of relations (27) and (28), we obtain the final equation in the form:

$$\frac{\partial z_b}{\partial t} + \frac{1}{(1 - n_p)} \left(\frac{\partial q_x^+}{\partial x^+} + \frac{\partial q_x^-}{\partial x^-} \right) = 0 \quad (42)$$

If the wave is propagating over an inclined bed, we should include the fact that:

$$\frac{\partial q_x^+}{\partial x^+} \neq \frac{\partial q_x^-}{\partial x^-} \quad (43)$$

Relation (43) indicates that in order to achieve the right solution of the sediment transport equation (43) in the case of linear relations (25) and (26), it is necessary to divide the volume of transport into two parts: q_x^+ and q_x^- . In fact, the values q_x^+ and q_x^- should be interpreted as the volume of transported sediment in hydrodynamic equilibrium, averaged for a wave period T , in the wave crest and trough, respectively, and q_x should be taken as a resultant sediment transport averaged for a wave period T (net transport rate).

In a 2-D case, equation (42) can be presented in a generalized form:

$$\frac{\partial z_b}{\partial t} + \frac{1}{(1 - n_p)} \left(\frac{\partial q_x^+}{\partial x^+} + \frac{\partial q_x^-}{\partial x^-} + \frac{\partial q_y}{\partial y} \right) = 0 \quad (44)$$

where,

q_y stands for the volume of longshore transport.

The volume of the longshore transport is divided into two parts because this transport is not connected with unidirectional flow, which would depend on the angle between the wave propagation direction and the direction of the profile transverse to the shore. It is assumed that positive values are taken to express the volume of transport if the sediment is transported according to the positive direction of y axis.

It can be noticed that the equilibrium between the sediment transport in the layer of densely packed sand grains in the moving sediment and the transport in the layer above means that bed disturbances (z_m^+ and z_m^- respectively) propagate without changing the shape. Obviously, this does not mean that – according to relations (27) and (28) – the bed level z_b disturbances move likewise without changing the shape. In other words, because the sediment transport rate is a non-linear function z_b , this equation of mass conservation is also physically a non-linear equation of conservation with respect to the bed level.

Comparison with experimental data

Our considerations about sediment transport under equilibrium conditions, i.e. about the linearity of equations (25) and (26), seem to be confirmed by the results of an experiment conducted at the Institute of Hydroengineering

of the Polish Academy of Sciences in Gdańsk in 1996 (cf. KACZMAREK 1999). In a wave flume continuously filled up, regular (tests 1, 2, 3, 4, 11 and 12) and irregular (tests 5, 6, 7, 8, 9, 10) waves were generated. The bed consisted of natural sand of the representative diameter $d_{50}=0.22$ mm. One of the objectives of the experiment was to determine the amount of sediment transported mainly in the bedload layer onshore and offshore, by measuring the amounts of sediment flowing into a sand trap, which was composed of two cells. Because the generated wave conditions corresponded to the ripple regime, the measurements were not taken until the time necessary for the establishment of the equilibrium conditions had elapsed. The experiment was run several times for each set of hydrodynamic parameters. In total, 141 such measurements were made for 12 tests.

Our comparison of the results of the measurements of sediment transport rates ($q_x^+ + |q_x^-|$) with the results of the measurements of the thickness ($z_m^+ + z_m^-$) of densely packed grains in moving sediment are shown in Figure 2, where the average values of the experimental measurements are presented. The mathematic tool used while modelling the sediment transport rates was a three-layer model of sediment transport, which has been developed for several years now at the Polish Academy of Sciences Institute of Hydroengineering in Gdańsk (cf. KACZMAREK 1999). A detailed description of this model is contained in Part 2 of this article. In our calculations, it was assumed that the grain-size distribution of the sediment corresponded to the measured grain-size distribution curve.

The dependence of the calculated values of ($q_x^+ + |q_x^-|$) on the averaged measured values of the thicknesses ($z_m^+ + z_m^-$) shows a distinctly linear

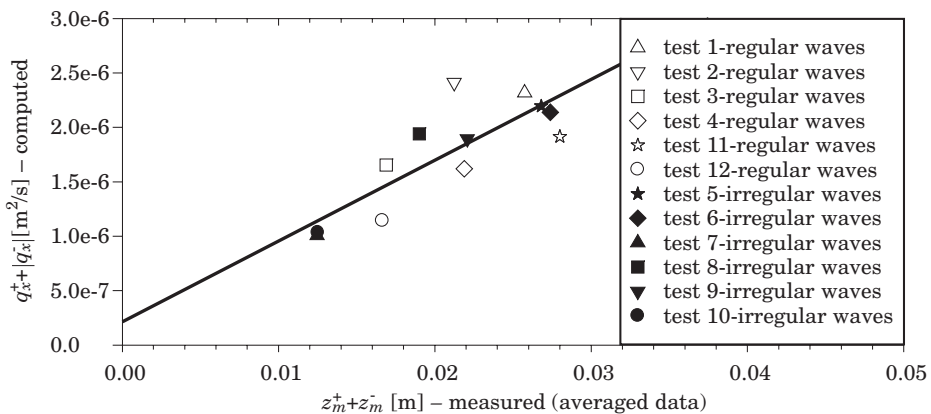


Fig. 2. Comparison of the results of modelling sediment transport rates with averaged measurements of thickness obtained from the experiment carried out at the Polish Academy of Sciences Institute of Hydroengineering in 1996

character. Thus, by virtue of equations (38) and (39), it should be noted that the expressions in the form of $(1 - n_p) U_{L_1}^-$ and $(1 - n_p) |U_{L_1}^-|$, respectively, represent the coefficient of proportionality of a straight line. In turn, the straight line crossing with the axis of ordinates (y-axis) (Fig. 2) seems to indicate the fact that the linear relation holds true only for such intensity of sediment transport which enables us to determine, for a given time dt , at a length of a sand trap $dx=L_{ST}$, the minimum thickness $(z_{m0}^+ + z_{m0}^-)$. In other words, for the rate of transport lower than the transport resulting from the crossing of the straight line with the axis of ordinates, the sand trap will not be filled up.

By virtue of equations (25) and (26), it can also be written:

$$B_{ST} (q_x^+ + |q_x^-|) dt = (1 - n_p)(z_m^+ + z_m^-) L_{ST} B_{ST} \quad (45)$$

where

B_{ST} is the width of a sand trap.

Using definition (31) and dependences (38) and (39), equation (45), once shortened by B_{ST} , can be transformed as follows:

$$\begin{aligned} (q_x^+ + |q_x^-|) dt &= (1 - n_p) \kappa \left(\int_{z_m^+}^{\eta} \langle C^+ \rangle dz + \int_{z_m^-}^{\eta} \langle C^- \rangle dz \right) L_{ST} \\ &= (1 - n_p) (\kappa - 1)(z_{m0}^+ + z_{m0}^-) L_{ST} + (1 - n_p)(z_{m0}^+ + z_{m0}^-) L_{ST} \end{aligned} \quad (46)$$

and then:

$$(q_x^+ + |q_x^-|) = (1 - n_p) (\kappa - 1)(z_{m0}^+ + z_{m0}^-) \frac{L_{ST}}{dt} (q_{x0}^+ + |q_{x0}^-|) \quad (47)$$

For comparison of the results of the calculations with the measurements, it is convenient to present equation (47) in the form:

$$(q_x^+ + |q_x^-|)_{\text{comp}} - (q_{x0}^+ + |q_{x0}^-|) = (1 - n_p) (z_m^+ + z_m^-)_{\text{meas.}} \frac{L_{ST}}{dt} \quad (48)$$

Non-linear effects

If the rate of sediment transport is to be described with non-linear relations with respect to z_m , the sediment transport is not in equilibrium with load hydrodynamics. This corresponds to a situation where a total amount of the sediment transported in suspension consists of part $\langle C_1 \rangle$, which is in equilib-

rium with load hydrodynamics and part $\langle C_2 \rangle$, which is transported in the form of inert mass. With respect to the bed accumulation, the exchange between the sediment transported in suspension $\langle C_2 \rangle$ and in the bed leads to the deposition process, whereas when the bed is eroded, the sediment is picked up by a current. Thus, we can write that:

$$\begin{cases} \langle C^I \rangle = (1 - n_p) & \text{and } \langle C^{II} \rangle = \langle C_1 \rangle + \langle C_2 \rangle \\ U_L^I = U_{L_1} & \text{and } U_L^{II} = U_{L_1} + U_{L_2} \end{cases} \quad (49)$$

Considering dependences (49) and (37), equation (19) can also be written:

$$\begin{aligned} (1 - n_p) \frac{\partial z_m}{\partial t} + \frac{\partial}{\partial t} \int_{z_m}^{\eta} \langle C_2 \rangle dz + (1 - n_p) U_{L_1} \frac{\partial z_m}{\partial x} + U_{L_1} \frac{\partial}{\partial x} \int_{z_m}^{\eta} \langle C_2 \rangle dz + \\ + \frac{\partial}{\partial x} \int_{z_m}^{\eta} U_{L_2} \langle C_1 \rangle dz + \frac{\partial}{\partial x} \int_{z_m}^{\eta} U_{L_2} \langle C_2 \rangle dz = 0 \end{aligned} \quad (50)$$

where

$$q = (1 - n_p) U_{L_1} z_m + U_{L_1} \int_{z_m}^{\eta} \langle C_2 \rangle dz + \int_{z_m}^{\eta} U_{L_2} \langle C_1 \rangle dz + \int_{z_m}^{\eta} U_{L_2} \langle C_2 \rangle dz \quad (51)$$

Let ∇_D denote the rate of sediment deposition, and ∇_E stand for the rate of sediment entrainment into the flow, then:

$$\frac{\partial}{\partial t} \int_{z_m}^{\eta} \langle C_2 \rangle dz = \nabla_E - \nabla_D \quad (52)$$

However, if in our considerations the suspended load contribution $\langle C_2 \rangle$ to the total sediment volume stored in the bed can be neglected (cf. LONG et al. 2008), then – taking advantage of dependence (28), equation (50) can be simplified to the form:

$$(1 - n_p) \frac{\partial z_b}{\partial t} + \frac{\partial q}{\partial x} = 0 \quad (53)$$

In equation (53), the sediment transport rate q consists of two parts (in respect of the thickness z_m):

– linear

$$q_x^L = q_x = (1 - n_p) U_{L1} z_m \quad (54)$$

and

– non-linear

$$q^{nL} = U_{L1} \int_{z_m}^{\eta} \langle C_2 \rangle dz + \int_{z_m}^{\eta} U_{L2} \langle C_1 \rangle dz + \int_{z_m}^{\eta} U_{L2} \langle C_2 \rangle dz \quad (55)$$

Because equation (53) contains a non-linear fragment described by dependence (55), the first order upward scheme cannot be applied in order to obtain the right solution. LONG et al. (2008) suggested using a fifth-order Euler-Weno scheme to solve this equation, simultaneously applying the decomposition of the sediment transport rate q into two parts q^+ and q^- .

In a contrary situation, when sediment is transported only as suspended, inert matter, possibly exchangeable with the sediment lying in the bed, thus causing either deposition of sediment or the picking up of sediment by a current, we can write:

$$\begin{cases} \langle C^I \rangle = (1 - n_p) & \text{and } \langle C^H \rangle = \langle C_2 \rangle \\ U_L^I = 0 & \text{and } U_L^H = U_{L2} \end{cases} \quad (56)$$

Considering relations (52) and (56) as well as (28), equation (50) can be written as:

$$(1 - n_p) \frac{\partial z_b}{\partial t} + \frac{\partial q}{\partial x} + \nabla_E - \nabla_D = 0 \quad (57)$$

where

$$q = q^{nL} = \int_{z_m}^{\eta} U_{L2} \langle C_2 \rangle dz \quad (58)$$

The above shows the non-linear part (in respect of z_m) of the sediment transport rate. In a non-linear case, it is not necessary to divide transport q into two parts q^+ and q^- . Furthermore, it should be mentioned that the component describing “storage” of sediment in the bed ($\nabla_E - \nabla_D$) can play

a more important role when local, spatially more rapid changes in the intensity of transport q occur, for example in the vicinity of constructions (WHITEHOUSE 1998).

Summary

The purpose of this paper has been to analyze the equation which describes changes in the bathymetry of the bed in time and space, derived from the principle of mass conservation. The analysis of the equation was carried out, *inter alies*, for the hydrodynamic equilibrium conditions, when a flow of sediments falling on the bed is balanced by a flow of sediments picked up from the bed, for which a linear dependence was derived between the sediment transport rate and the thickness of the layer of densely packed sand grains in the sediment in motion. This dependence enables us to apply the first-order upwind scheme to calculations of changes in the bed's bathymetry in time and space. However, in order to correctly solve the equation, it is necessary to divide the sediment transport into the positive direction – onshore – and negative one – offshore. The onshore transport takes place during the wave crest duration while the offshore transport appears during the wave trough time.

The linear form of the dependence between the sediment transport rate and thickness of the layer of densely packed grains, suggested in this paper, has been experimentally confirmed by the results of the experiment conducted in a laboratory of the Polish Academy of Sciences Institute of Hydroengineering in 1996.

This article constitutes a theoretical basis for mathematical description of changes in bathymetry in time and space, which will take into consideration changes in the grain size distribution in sediments which make up the bed. Applicability of the model has been demonstrated in Part 2, where a laboratory experiment run under wave and current conditions was used as a case for modelling changes in bathymetry, changes in the grain size distribution of sediments in the bed as well as vertical profiles of concentrations of suspended sediments near a canal which serves as a model of an approach fairway to a harbour.

References

- FREDSØE J., DEIGAARD R. 1992. *Mechanics of coastal sediment transport*. Advanced Series on Ocean Engineering, vol. 3, World Scientific, Singapore.
- KACZMAREK L.M. 1999. *Moveable Sea Bed Boundary Layer and Mechanics of Sediment Transport*. IBW PAN, Gdańsk.
- KACZMAREK L.M., OSTROWSKI R. 2002. *Modelling intensive near-bed sand transport under wave-current flow versus laboratory and field data*. Coastal Engineering, 45(1): 1–18.
- KACZMAREK L.M., BIEGOWSKI J., OSTROWSKI R. 2004. *Modelling cross-shore intensive sand transport and changes of grain size distribution versus field data*. Coastal Engineering, 51(5–6): 501–529.
- SAWCZYŃSKI Sz., KACZMAREK L.M., BIEGOWSKI J. 2011. *Bathymetry changes and sand sorting during sedimentation of waterways: Part 2 – Modelling versus laboratory data*. Technical Sciences, 14(2).
- JOHNSON H.K., ZYSERMAN J.A. 2002. *Controlling spatial oscillations in bed level update schemes*. Coastal Engineering, 47(1): 77.
- LONG W., KIRBY J.T., SHAO Z. 2008. *A numerical scheme for morphological bed level calculations*. Coastal Engineering, 55(2): 167–180.
- MITOSEK M. 2001. *Mechanika płynów w inżynierii i ochronie środowiska*. Wydawnictwo Naukowe PWN, Warszawa.
- NICHOLSON J., BROKER I., ROELVINK J.A., PRICE D., TANGUY J.M., MORENO L. 1997. *Intercomparison of coastal area morphodynamic models*. Coastal Engineering, 31(1–4): 97–123.
- PUZYREWSKI R., SAWICKI J. 2000. *Podstawy mechaniki płynów i hydrauliki*. Wydawnictwo Naukowe PWN, Warszawa.
- WHITEHOUSE R.J.S. 1998. *Scour at Marine Structures*. Thomas Telford, London.

**BATHYMETRY CHANGES AND SAND SORTING
DURING SEDIMENTATION OF WATERWAYS.
PART 2 – MODELLING VERSUS LABORATORY DATA**

***Szymon Sawczyński¹, Leszek M. Kaczmarek^{1,2},
Jarosław Biegowski²***

¹ The Chair of Civil Engineering and Building Structures
University of Warmia and Mazury in Olsztyn

² Institute of Hydroengineering, Polish Academy of Sciences in Gdańsk

Key words: graded sediment, sediment transport, bed grain size distribution changes, bathymetry changes, sediment velocity, sorting, sedimentation.

Abstract

A theoretical, three-layer model of non-uniform sediment transport has been applied in our analysis of the sedimentation of navigable waterways tested under laboratory conditions. This model distinguishes three layers of moving sediment and, additionally, includes an assumption that sediment is not sorted out in the bedload layer but vertical grading occurs only when grains are lifted up in the contact layer. Above that layer, in the outer flow region, the grain size distribution of sediment remains unchanged. Moreover, it has been assumed that during the wave crest phase, sediment is transported in the bedload and contact layers as well as in the outer flow layer under the influence of a resultant current directed, as described in the present article, in the same direction as the propagating surface wave. During the wave trough phase, sediment transport occurs in the bedload and contact layers. The mathematical description of changes in the bed level (bathymetry), contained in this paper, divides sediment transport into the one in the positive direction, during the wave crest phase, in the wave propagation direction, and the one in the negative direction, during the wave trough phase, reverse to the wave propagation direction. The results obtained from modelling changes in bathymetry compared with the results from a laboratory experiment conducted in a wave flume under the wave and current conditions yielded satisfactory coincidence. The effect of including changes in the grain size distribution into the calculations proved to be highly significant. The calculations demonstrated that the applied model could be a useful tool for both predicting changes in the bathymetry in approach waterways to harbours and determining grain size distribution of sediment which fills up a waterway or the rate of sedimentation of a waterway.

ZMIANY BATYMETRII I SEGREGACJA OSADÓW W PROCESIE ZAPIASZCZANIA TORÓW WODNYCH. CZĘŚĆ 2 – PORÓWNANIE WYNIKÓW MODELOWANIA Z WYNIKAMI POMIARÓW LABORATORYJNYCH

Szymon Sawczyński¹, Leszek M. Kaczmarek^{1,2}, Jarosław Biegowski²

¹ Katedra Budownictwa i Konstrukcji Budowlanych
Uniwersytet Warmińsko-Mazurski w Olsztynie

² Instytut Budownictwa Wodnego PAN w Gdańsku

Key words: sortowaie osadów, transport osadów, zmiany rozkładów uziarnienia, zmiany batymetrii, prędkość rumowiska, sortowanie, zapiaszczanie.

Abstrakt

Do analizy zapiaszczania torów wodnych w warunkach laboratoryjnych wykorzystano trójwarstwowy model teoretyczny transportu osadów niejednorodnych granulometrycznie. Model ten wyszczególnia trzy warstwy ruchu rumowiska, przy czym założono, że w warstwie wleczenia osady nie są sortowane, a pionowe sortowanie odbywa się tylko w procesie podrywania ziaren w warstwie kontaktowej. Ponad tą warstwą – w zewnętrznym obszarze, rozkład granulometryczny osadu pozostaje niezmienny. Ponadto założono, że w fazie grzbietu fali osady są transportowane w warstwach wleczenia i kontaktowej oraz zewnętrznej – pod wpływem wypadkowego prądu, skierowanego w tę samą stronę, co propagująca fala powierzchniowa. W fazie doliny fali transport rumowiska odbywa się tylko w warstwach wleczenia i kontaktowej. W opisie matematycznym zmian poziomu dna (batymetrii) podzielono transport osadów na transport w kierunku dodatnim, odbywający się w czasie trwania grzbietu fali, w kierunku propagacji fali i kierunku ujemnym, odbywający się w kierunku przeciwnym w czasie trwania doliny fali. Wyniki modelowania zmian batymetrii w porównaniu z wynikami pochodzącymi z eksperymentu laboratoryjnego przeprowadzonego w kanale falowym w warunkach falowo-prądowych dały zadowalającą zgodność. Wpływ uwzględniania w obliczeniach zmian rozkładów uziarnienia osadów okazał się niezwykle istotny. Przeprowadzone obliczenia pokazały, że zastosowany model obliczeniowy może być użytecznym narzędziem służącym do prognozowania zarówno zmian batymetrii w obrębie torów podejściowych do portów, jak i w określaniu rozkładów granulometrycznych osadów wypełniających tor wodny, a także tempa zapiaszczania torów wodnych.

Introduction

For maintaining the right navigable depth of fairways and planning dredging works, it is crucial to be able to predict accurately amounts of transported bed load and the rate at which approach waterways to harbours are silted up. It is equally important to understand well the mechanisms which cause motion of sediments of different grain size structure, and to be able to predict transported load of particular fractions of sediment as well as to know the actual grain size distribution of sediment in a given fairway. Such knowledge may prove valuable when planning and conducting silting-up works

needed for artificial nourishment of shores, when trying to determine the effectiveness of seashore protection schemes, etc. In many cases, silt material is dredged from a waterway and then used to strengthen the shore near a harbour. Then, it is very useful to know the grain size structure of the sand because if too fine silt is used for reinforcing the banks, a situation may arise when artificial seashore nourishment will turn into a useless and unprofitable operation because the sand previously dug out from the seabed and laid on the shores will be washed away very quickly.

This article is a continuation of Part 1, where – based on the mass conservation principle – elementary derivation was presented of an equation applied to describing changes in the seabed bathymetry in time and space. A detailed analysis of this equation was performed in respect of the dependence between the transport rate and thickness of densely packed grains in moving sediment. Based on the theoretical considerations, verified by the results obtained in a laboratory experiment, it was suggested to describe this dependence in the form of a linear function for the so-called hydrodynamic equilibrium condition.

In the paper, we discuss the applicability of the three-layer model of non-uniform sediment transport, as developed by KACZMAREK (1999) according to the principle of conservation of water and sediment momentum in the nearbed layer, to solving specific engineering problems – with sedimentation of a waterway as a case example – and comparing the results to another laboratory experiment carried out in a flume canal at the Delft Hydraulics (VAN RIJN 1986).

Sand transport

Momentum equation in the bedload layer

In the discussed model of the transport of sediment with particles different in size, it has been proposed to use a mathematical model to describe interactions between water and sediment as well as mutual interactions between sediment grains in the whole interaction area, from the immobile bed to the formation of “a carpet” of sediments, up to suspended sediments. According to the description presented by KACZMAREK (1999) for uniform sediment under pure oscillatory flow conditions and by KACZMAREK and OSTROWSKI (2002) for flows under the wave and current conditions and by KACZMAREK et al. (2004) for graded sediments, the area in which sediment moves can be divided into three layers: 1) bedload layer, 2) contact load layer and 3) outer flow region.

Employing Sayed and SAVAGE'S (1983) dependences for viscous stresses and for the stresses due to Coloumb friction, for conditions when the transport of sediments is in hydrodynamic equilibrium, i.e. the flow of sediments falling on the bed is offset by the flow of sediments picked up from the bed, a set of equations has been proposed that describes the celerity and concentration of sediments in the bedload layer, which can be presented in the form:

$$\alpha^0 \left(\frac{c_b - c_0}{c_m - c_b} \right) \sin \phi \sin 2\psi + \mu_1 \left(\frac{\partial u_b}{\partial z'} \right)^2 = \rho u_f^2 \quad (1)$$

$$\begin{aligned} \alpha^0 \left(\frac{c_b - c_0}{c_m - c_b} \right) (1 - \sin \phi \sin 2\psi) + (\mu_0 + \mu_2) \left(\frac{\partial u_b}{\partial z'} \right)^2 \\ = \left(\frac{\mu_0 + \mu_2}{\mu_1} \right) \Big|_{c=c_0} \rho u_f^2 + (\rho_s - \rho)g \int_0^{z'} c_b dz' \end{aligned} \quad (2)$$

The factors μ_0 , μ_1 and μ_2 are functions of the concentration of sediment c , determined by the formulas:

$$\frac{\mu_1}{\rho_s d^2} = \frac{0.03}{(c_m - c_b)^{1.5}} \quad (3)$$

$$\frac{\mu_0 + \mu_2}{\rho_s d^2} = \frac{0.02}{(c_m - c_b)^{1.75}} \quad (4)$$

where:

$c_m (= 0.53)$ – maximum concentration of sediment at rest when grains closely adhere to one another,

c_b – sediment concentration,

u_b – velocity of sediment in the bedload layer,

c_0 – concentration of sediment at the theoretical bed level ($c_0 = 0.32$),

$\alpha^0 / \rho_s g d = 1.0$,

ρ_s – density of skeletal ground,

ρ – density of water,

d – diameter of sediment grains,

ϕ – quasi-static inner friction angle,

$$\psi = \frac{\pi}{4} - \frac{\phi}{2}.$$

Due to strong interactions between particles of each fraction in the bedload layer, it was assumed that all fractions moved at the same speed $u_{br}(z',t)$ and had identical concentration $c_{br}(z',t)$ at a given level z' . From this assumption, it has been concluded that sediment in the bedload layer is not being sorted out, which then enables us to describe the transport of sediment using a representative particle diameter $d_r = d_{50}$. Thus, having the representative diameter d_r , we can determine the effective coarseness $k_e = k_{er}$ from the formula proposed by KACZMAREK (1999):

$$k_{er} = 47.03 d_r \theta_{2.5}^{-0.658} \quad (5)$$

in which, as NIELSEN (1992) demonstrated

$$\theta_{2.5} = 0.5 f_{2.5} \psi_1 = 0.5 f_{2.5} \frac{(\alpha_{1m} \varpi)}{(s-1)gd_r} \quad (6)$$

and

$$f_{2.5} = \exp \left[5.213 \left(\frac{2.5 d_r}{\alpha_{1m}} \right)^{0.194} - 5.977 \right] \quad (7)$$

where

g – acceleration of gravity,

$\alpha_{1m} = U_{1m}/\varpi$ – horizontal amplitude of the nearbed wave motion,

U_{1m} – maximum orbital velocity near the bed,

$s = \rho_s/\rho$ – relative density,

$\varpi = 2\pi/T$ – orbital frequency,

T – wave period.

Next, from FREDSE'S (1984) integral model, instantaneous friction velocities $u_r(t)$ on the bed surface are determined. From equations (1) – (4) we obtain instantaneous values of the velocity $u_{br}(z',t)$ and concentration $c_{br}(z',t)$ of the sediments in the bedload layer of the thickness δ_{br} . The z' axis is orientated positively downwards from the theoretical bed level. The first reference point, where the sediment velocity $u_{br}(z',t)$ is equal to zero, is denoted as the coordinate δ_{br} , which describes the thickness of the bedload layer. Noteworthy is the fact that the model adopted to describe changes in the bedload layer removed one of the major simplifications until now broadly applied to the modelling of ungraded sediment transport, namely the presented model assumes that interactions between fractions are so strong that consequently finer fractions are slowed down by coarser ones and eventually all fractions move at the same speed. Thus, simple summation of transport rates of all the

fractions in sediment, treated here as uniform deposit, is not applicable to transport processes in this layer, which means that:

$$n_i q_{bi} \neq n_i q_{br} \quad (8)$$

where

n_i – percentage of a given sediment fraction in the whole mixture.

The above conclusion coincides with many laboratory observations (cf. HASSAN et al. 2001, and KACZMAREK et al. 2004).

We should, however, remember that a current causing erosion (due to shearing) of the bed in a cell does not cause changes in the distribution of grain sizes.

Thus, the bedload transport rate in the shoreward x -direction q_{bx}^+ is equal to:

$$q_{bx}^+ = \frac{1}{T} \int_0^{T_c} \left(\int_0^{\delta_{br}^+} u_{br}^+(z',t) c_{br}^+(z',t) dz' \right) dt \quad (9)$$

whereas the bedload transport rate in seaward x -direction q_{bx}^- is:

$$q_{bx}^- = \frac{1}{T} \int_0^T \left(\int_0^{\delta_{br}^-} u_{br}^-(z',t) c_{br}^-(z',t) dz' \right) dt \quad (10)$$

where

T_c and T are wave crest and wave periods, respectively.

Momentum equation in the contact layer

In the contact layer, turbulent pulsations and chaotic collisions between sand grains cause big differences in the transport of particular fractions of the sediment. In the contact layer, two sub-layers were distinguished, characterized by different mechanisms of current exchange. Near the bed – in the sub-layer where decompositions of the velocity of the i -th fraction of sediments quite evidently reveal slip velocity u_{br} – in this sub-layer, there are very strong interactions between particular fractions, caused by chaotic, mutual collisions between sediment grains. Although further away from the bed, interactions between the fractions become weaker, the concentration of the i -th fraction is

big enough to muffle turbulences, which depend on the grain diameter d_i . It can, therefore, be expected that each i -th fraction moves at its own speed $u_{ci}(z,t)$ and is characterized by its own concentration $c_{ci}(z,t)$. In this model, these instantaneous distributions of speed and concentration for the i -th fraction are determined from the equations suggested by KACZMAREK (1999), when the variable of the skin friction velocity $u_{fi}'(t)$ in the wave period is known:

$$\left[\frac{3}{2} \left(\alpha \frac{d_i}{w_{si}} \frac{du_{ci}}{dz} \frac{2}{3} \frac{s + c_M}{c_D} + \beta \right)^2 d_i^2 c_{ci}^2 (s + c_M) + l^2 \right] \left(\frac{du_{ci}}{dz} \right)^2 = u_{fi}'^2(t) \quad (11)$$

$$\left[\frac{3}{2} \left(\alpha \frac{d_i}{w_{si}} \frac{du_{ci}}{dz} \frac{2}{3} \frac{s + c_M}{c_D} + \beta \right)^2 d_i^2 \frac{du_{ci}}{dz} c_{ci} + l^2 \frac{du_{ci}}{dz} \right] \frac{du_{ci}}{dz} = -w_{si} c_{ci} \quad (12)$$

where,

c_D – resistance factor,

c_M – added mass factor,

l – mixing length, expressed as $l = \kappa z'' = 0.4z'$,

κ – Karman constant,

with the z axis directed upward.

DEIGAARD (1993) assumed that $(s + c_M) = 3.0$, while $c_D = 1.0$. Values of the proportionality factors α_s and β_s are unknown and must be determined by scaling the computational model. The value $u_{fi}'(t)$ is determined from FREDSE'S model (1984), including the assumption formulated by NIELSEN (1992) that the effective skin roughness k'_{ei} is defined by the relation $k'_{ei} = 2.5d_i/30$. The marginal conditions for all the fractions are identical, i.e.

$$u_{ci}(z = 2.5d_i/30, t) = u_{br}(z' = 0, t) \quad (13)$$

$$c_{ci}(z = 2.5d_i/30, t) = c_{br}(z' = 0, t) = 0.32 \quad (14)$$

Including the effective skin roughness, determined for the representative diameter $k'_{er} = 2.5d_r = 2.5d_{50}$, and using FREDSE'S integral model (1984), the upper boundary of the contact layer – shared by all the fractions – is determinable (δ_{cr}).

As has been demonstrated by Kaczmarek (1999), this thickness can be determined by the dependence $\delta_{cr} = \delta_1'/2$, in which δ_1' corresponds to the thickness of the near-wall layer – found from FREDSE'S (1984) solution for $k'_{er} = 2.5d_r = 2.5d_{50}$ – at the moment of the maximum (during wave period T) orbital velocity near the bed.

It is worth noticing that the velocities and concentrations of coarser fractions within the contact layer as computed in the proposed model, are larger than the values these fractions would have attained had the bed been uniform and composed of just one corresponding fraction. This accelerated speed in a mixture is a result of mutual interactions between fractions, where coarser fractions are accelerated by finer ones. The above effect has been demonstrated by several researchers, for example de MEIJER et al. (2002). The laboratory observations reported by these authors prove that coarser fractions of sediment are transported more intensively in an ungraded mixture than in uniform sediment.

As mentioned earlier, instantaneous values of the speed and concentration of sediment for the i -th fraction in the presented model are derived from equations (11) and (12). In turn, values of the sediment mixture concentration averaged for the wave period T can be obtained as follows:

$$C_c(z) = \sum_{i=1}^n n_i \left(\frac{1}{T} \int_0^T c_i(z, t) dt \right) \quad (15)$$

whereas the percentage content k_i of the i -th fraction can be computed from:

$$k_i(z) = \frac{\langle c_{ci}(z, t) \rangle n_i}{C_c(z)} \quad (16)$$

where:

$$\langle c_{ci}(z, t) \rangle = \frac{1}{T} \int_0^T c_{ci}(z, t) dt \quad (17)$$

By knowing the percentage content of k_i of the i -th fraction on each level (z) within the contact layer at each step in the computations, it is easy to calculate the grain-size distribution as well as the representative value $d_{50}(z)$ in the suspended sediment found in this layer.

Recapitulating, it should be emphasized that in the presented model of sediment transport both in the contact and bedload layers, simple summation of transport rates of particular fractions, treated as uniform sediment, is not applicable.

Thus, also in this case, the contribution of the i -th fraction to the transport of the whole mixture $n_i q_{ci}$ does not equal to the “independent” transport $n_i q_i$, which means that $n_i q_i \neq n_i q_{ci}$.

Finally, the contact load transport in the shoreward x direction q_{cx}^+ for the mixture can be written as:

$$q_{bx}^+ = \sum_{i=1}^N n_i \left(\frac{1}{T} \int_0^{T_c} \left(\int_0^{\delta_{cr}} u_{ci}^+(z,t) c_{ci}^+(z,t) dz \right) dt \right) \quad (18)$$

while, the contact load transport rate in the seaward x -direction q_{cx}^- as:

$$q_{bx}^- = \sum_{i=1}^N n_i \left(\frac{1}{T} \int_{T_c}^T \left(\int_0^{\delta_{cr}} u_{ci}^-(z,t) c_{ci}^-(z,t) dz \right) dt \right) \quad (19)$$

Outer flow region

In the outer layer, we encounter certain difficulties while striving to describe correctly the time-variable profile of concentrations of suspended sediment. Higher above the bed, researchers indicate that there is no agreement in the phase between theoretical models and experimental results (DAVIES et al. 1997). Thus, in order to obtain a time-averaged value of the concentration $c_0(z)$ of a mixture of suspended sediment, the dependence in the following form is applied (cf. RIBBERINK and AL-SALEM 1994):

$$\langle C_0(z) \rangle = \langle C_0(z = \delta_{cr}) \rangle \left(\frac{\delta_{cr}}{z} \right)^{\alpha_1} \quad (20)$$

where, the concentration on the reference level is determined as time-averages of the results obtained for the contact layer:

$$\langle c_0(z = \delta_{cr}) \rangle = \sum_{i=1}^N \langle c_{ci}(z = \delta_{cr}, t) \rangle n_i \quad (21)$$

The exponent of the α_1 power has an unknown value, which is determinable from experimental data. As shown by BIEGOWSKI (2006), by selecting $\alpha_1 = 0.6$, the best coincidence is attained between results of calculations and data from field trials and laboratory experiments conducted in a large-scale flume canal. We should add that for $\alpha_1 = \text{const.}$ it is impossible to speak about any vertical sorting of sediments in a mixture, which means that the grain size distribution in the outer layer remains unchanged. Further, the sediment transport rates in the outer flow zone are determined using the following simplified formulas:

$$q_{ox}^- = \int_{\delta_{cr}}^h U_{ox}^-(z) \langle C_0(z) \rangle dz \quad (22)$$

$$q_{oy} = \int_{\delta_{cr}}^h U_{oy}(z) \langle C_0(z) \rangle dz \quad (23)$$

where

h is the water height and velocities $U_{ox}^-(z)$ and $U_{oy}(z)$ are the velocities of a current induced in the nearshore zone of the sea, respectively to the reverse current (offshore) and longshore current, generated by waves which propagate at an angle to the shore's transverse profile.

Conservation of the sediment mass

The equation derived from the principle of mass conservation, as shown in detail in Part 1, can be presented for a 2-D case in the following form:

$$\frac{\partial z_m}{\partial t} + \frac{1}{(1 - n_p)} \left(\frac{\partial q_x^+}{\partial x^+} + \frac{\partial q_x^-}{\partial x^-} + \frac{\partial q_y}{\partial y} \right) = 0 \quad (24)$$

where:

q_y – the longshore sediment transport rate,

q_x^+ – the onshore sediment transport rate,

q_x^- – the offshore sediment transport rate,

z_m – thickness of the layer of sediment grains being in motion and densely packed.

In the space (j, k) of the shore's transverse profile, the layer z_m changes over a time period Δt . Erosion or accumulation happens because of changes in the transport rates q_x^+ and q_x^- over the length Δx as well as q_y over the length Δy . Taking advantage of the upwind numerical scheme, equation (24) can be written with the help of finite differences in the form:

$$\begin{aligned} \Delta(z_m)_{j,k} = & \frac{\Delta t}{\Delta x} [(q_x^+)_{j,k} + |(q_x^-)_{j,k}| - (q_x^+)_{j-1,k} - |(q_x^-)_{j+1,k}|] \\ & + \frac{\Delta t}{\Delta y} [|(q_y)_{j,k}| - |(q_y)_{j,k-1}|] = \end{aligned}$$

$$\begin{aligned}
&= \frac{\Delta t}{\Delta x} [(q_{bx}^+)_{j,k} + (q_{cx}^+)_{j,k} + |(q_{bx}^-)_{j,k}| + |(q_{cx}^-)_{j,k}| + |(q_{0x}^-)_{j,k}| - (q_{bx}^+)_{j-1,k} \\
&\quad - (q_{cx}^+)_{j-1,k} - |(q_{bx}^-)_{j+1,k}| - |(q_{cx}^-)_{j+1,k}| - |(q_{0x}^-)_{j+1,k}|] \\
&\quad + \frac{\Delta t}{\Delta y} [(q_{0y})_{j,k}| - |(q_{0y})_{j,k-1}|]
\end{aligned} \tag{25}$$

where

q_{bx} – rate of the transport of sediment in the bedload layer in the direction of axis x [m^2/s],

q_{cx} – rate of the transport of sediment in the contact layer in the direction of axis x [m^2/s],

$q_{0x(y)}$ – rate of the transport of suspended sediment in the direction of axis $x(y)$ [m^2/s].

Dependence (25) describes the thickness of the eroded or accumulated layer without including the porosity of sediments. Hence, in order to account for the effect of porosity on the thickness $\Delta(z_m)_{j,k}$ the result obtained should be multiplied by $(1-n_p)$.

All the transport rate components in equation (25) have positive values, which means that the values with a preceding „+” sign cause an increase in the depth, i.e. erosion of the bed, whereas the ones preceded with a „-” sign cause a decrease in the depth, that is the accumulation of the bed in a given point (j,k) .

The thickness of the eroded or accumulated layer for each i -th fraction of the sediment of which the bed is composed can be determined in the following way:

$$\begin{aligned}
\Delta(z_m)_{j,k}^i &= \frac{\Delta t}{\Delta x} [(q_{bx}^+)_{j,k}^i + (q_{cx}^+)_{j,k}^i + |(q_{bx}^-)_{j,k}^i| + |(q_{cx}^-)_{j,k}^i| + |(q_{0x}^-)_{j,k}^i| - (q_{bx}^+)_{j-1,k}^i \\
&\quad - (q_{cx}^+)_{j-1,k}^i - |(q_{bx}^-)_{j+1,k}^i| + |(q_{cx}^-)_{j+1,k}^i| - |(q_{0x}^-)_{j+1,k}^i|] \\
&\quad + \frac{\Delta t}{\Delta y} [(q_{0y})_{j,k}^i| - |(q_{0y})_{j,k-1}^i|]
\end{aligned} \tag{26}$$

where

$$\Delta(z_m)_{j,k} = \sum_{i=1}^N \Delta(z_m)_{j,k}^i \tag{27}$$

Predictably, in time Δt , the grain size distribution in the control volume changes from $n_{j,k}^i$ ($\sum n_{j,k}^i = 1$) to $m_{j,k}^i$ ($\sum m_{j,k}^i = 1$) according to the formula (cf. KACZMAREK et al. 2004):

$$m_{j,k}^i = \frac{n_{j,k}^i (h_m)_{j,k} - \Delta(z_m)_{j,k}^i}{(h_m)_{j,k} - \Delta(z_m)_{j,k}} \quad (28)$$

In equation (28), the value of $(h_m)_{j,k}$ describes the thickness of the mixing layer, as it is in that layer that the grain size distribution changes from $n_{j,k}^i$ to $m_{j,k}^i$ in time Δt . This change is induced by the difference in the rates of transport of particular fractions over the lengths Δx and Δy .

As has been demonstrated by KACZMAREK et al. (2004), we can assume that in the time period Δt half the transported sediment over a plane seabed in the analyzed area is scattered and suspended in the contact and outer flow layers (j,k), whereas the other half remains in the bedload layer and is mixing with the sediments flowing from other areas. The thickness of the mixing layer, therefore, takes the form of:

$$(h_m)_{j,k} = 2 \frac{\Delta t}{\Delta x} [(q_{bx}^+)_{j,k} + (q_{cx}^+)_{j,k} + |(q_{bx}^-)_{j,k}| + |(q_{cx}^-)_{j,k}| + |(q_{0x}^-)_{j,k}|] + 2 \frac{\Delta t}{\Delta y} [|q_{0y}|_{j,k}] \quad (29)$$

The laboratory tests have revealed that the thickness of the mixing layer ranges from 2 cm (SISTERMANS 2001) to 5 cm (CHATELUS et al. 1998).

It is interesting to note that a change in the grain size distribution in the mixing layer $(h_m)_{j,k}$ from $n_{j,k}^i$ to $m_{j,k}^i$ does not depend on discretization in time or space because (assuming for simplification that $\Delta x = \Delta y$) all the components in the numerator and denominator in equation (28) contain the element $\Delta t/\Delta x$. A change in the grain size distribution, therefore, depends exclusively on the difference in the sediment transport rates.

Let us assume that in the analyzed control volume of the thickness $(h_m)_{j,k}$ erosion occurs (the value of $\Delta(z_m)_{j,k}$ is positive), then after the time Δt , it will cause the appearance of “a carpet of sediments” of the thickness $\alpha_{j,k}$:

$$\alpha_{j,k} = (h_m)_{j,k} - \Delta(z_m)_{j,k} \quad (30)$$

Thus, after the time Δt , i.e. during the time moment $(t + \Delta t)$, a new grain size distribution in a new mixing layer of the thickness $(h_m)_{j,k}$ will be composed of the distribution $m_{j,k}^i$ found in the „carpet of sediments” of the thickness $\alpha_{j,k}$ and the distribution $(n_s)_{j,k}^i$, which characterizes the sediment in the parental bed:

$$[n(t + \Delta t)]_{j,k}^i = \frac{\alpha_{j,k} m_{j,k}^i + [(h_m)_{j,k} - \alpha_{j,k}](n_s)_{j,k}^i}{(h_m)_{j,k}} \quad (31)$$

If, in contrast, we assume that sediment is accumulated in the analyzed area (the value $\Delta(z_m)_{j,k}$ is negative), then the new grain size distribution after the time Δt will be composed of the distribution $m_{j,k}^i$ alone, which will be found in the „carpet of sediments” of the thickness $\alpha_{j,k}$.

Finally, by taking into consideration the porosity of sediment n_p , we obtain the dependence which describes changes in the bed bathymetry in time and space, which take into account changes in the grain size distribution of the sediments of which the seabed is composed:

$$h_{j,k}(t + \Delta t) = h_{j,k}(t) + \frac{1}{1 - n_p} \Delta(z_m)_{j,k} \quad (32)$$

Delft Hydraulics laboratory experiment

Some of the laboratory measurements have been carried out at the Delft Hydraulics (VAN RIJN 1986), a research centre situated in northern Holland, in a flume canal 17.0 m long, 0.3 m wide and 0.5 m deep (Fig. 1). The aim of the experiment was to determine changes in bathymetry under given wave and current conditions and to establish vertical profiles of suspended sediment concentrations. The total duration of the trial was 10 hours.

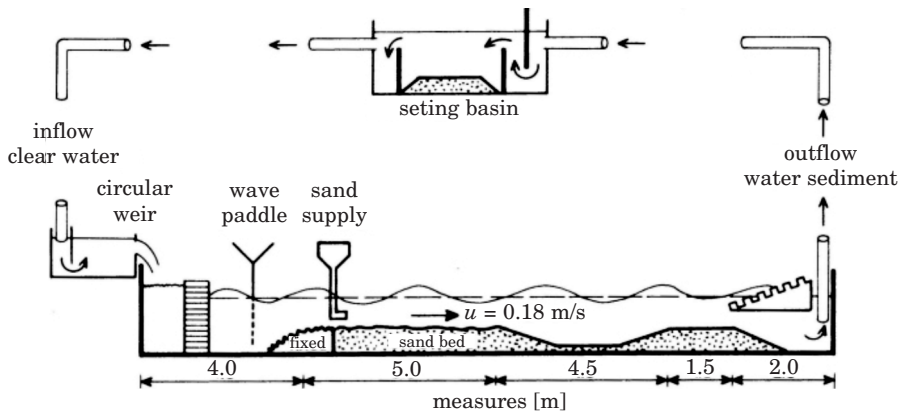


Fig. 1. The design of the experiment

Source: VAN RIJN (1986).

The bed consisted of a layer of fine sand ($d_{50} = 100 \mu\text{m}$, $d_{90} = 130 \mu\text{m}$) about 0.2 m thick. The incline of the canal's edge was 1:10. Sediment was supplied evenly from the inflow side of the canal so as to maintain constant (balanced) conditions. Regular waves of the height of 0.08 m and wave period 1.5 s were generated, and the current was set according to the direction of wave propagation. During the experiment, concentrations of sediment were measured in vertical profiles at five sites located along the canal (Fig. 2). Table 1 presents some of the basic parameters of the experiment.

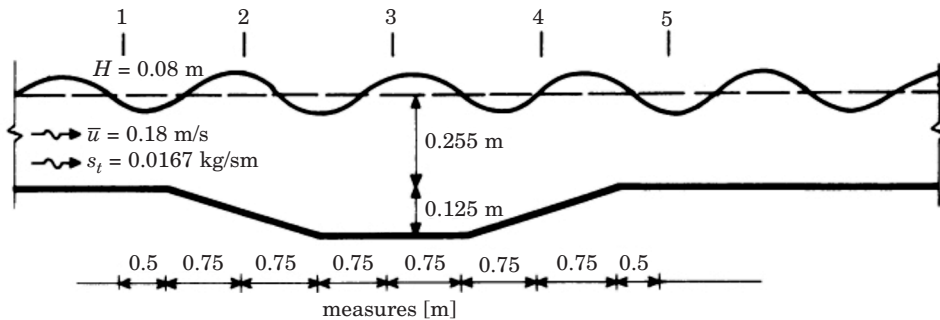


Fig. 2. Location of the measurement sites along the canal

Source: VAN RIJN (1986).

Table 1

Basic parameters of the experiment at the Delft Hydraulics

Parametr	Value
Water depth h_0	0.255 [m]
Mean current velocity u_0	0.18 [m/s]
Wave height H	0.08 [m]
Wave period T	1.5 [s]
Transport of suspended sediment $q_{s.o}$	0.167 [kg/sm]
Diameter of grains of the sediment in bed d_{50} ; d_{90}	0.10; 0.13 [mm]
Diameter of grains of the suspended sediment d_s	0.08 – 0.011 [mm]
Fall velocity of suspended grains w_s	0.005 – 0.010 (mean: 0.007) [m/s]
Density of sediment ρ_s	2650 [kg/m ³]
Density of fluid ρ_w	1000 [kg/m ³]
Porosity of sediment n_p	0.4 [-]

Model results versus laboratory data

Modelling distributions of the vertical concentration of sediments

The scope and course of the experiment (cf. Figs 1 and 2) conducted at the Delft Hydraulics (VAN RIJN 1986) implicates a theoretical solution to a two-dimensional problem, i.e. it forces researchers to add the simplification $(q_{0y})_{j,k} = (q_{0y})_{j,k-1}$ to differential equations (25) and (29) due to the lack of a longshore current in the above experiment. Besides, in equations (25) and (29), the values $(q_{0x}^-)_{j,k}$ and $(q_{0x}^-)_{j+1,k}$ need to be substituted, respectively, with the values $(q_{0x}^+)_{j,k}$ and $(q_{0x}^+)_{j+1,k}$ because in the above experiment the current in the outer layer was directed in accordance with the propagation of waves, whereas equations (25) and (29) are based on the assumption that the current flows offshore, as is typical of the shore zone.

In the mathematical modelling of the vertical concentration of suspended sediments, two available parameters, d_{50} and d_{90} , were used as input data for analyzing the grain size distribution of sediment. By knowing these data, it was possible to draw a grain-size curve, presented in Fig. 3. Due to the very narrow range of diameters of the fine sediment used in the experiment, three representative diameters were taken, which correspond to the lower values of the diameter ranges, shown in Fig. 3 as a histogram. The lower values of these ranges correspond to the mesh in the control sieves.

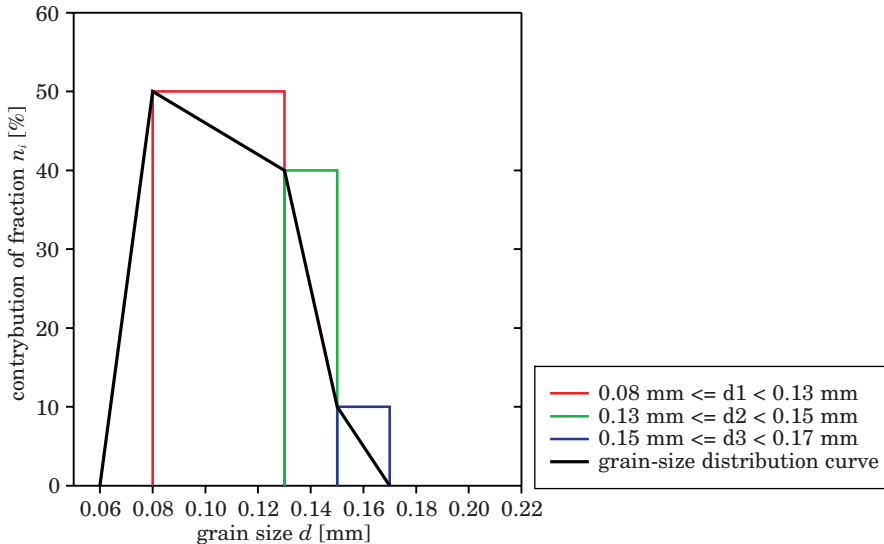


Fig. 3. The histogram of sediment grain size distribution used for calculations, acc. to parameters d_{50} and d_{90}

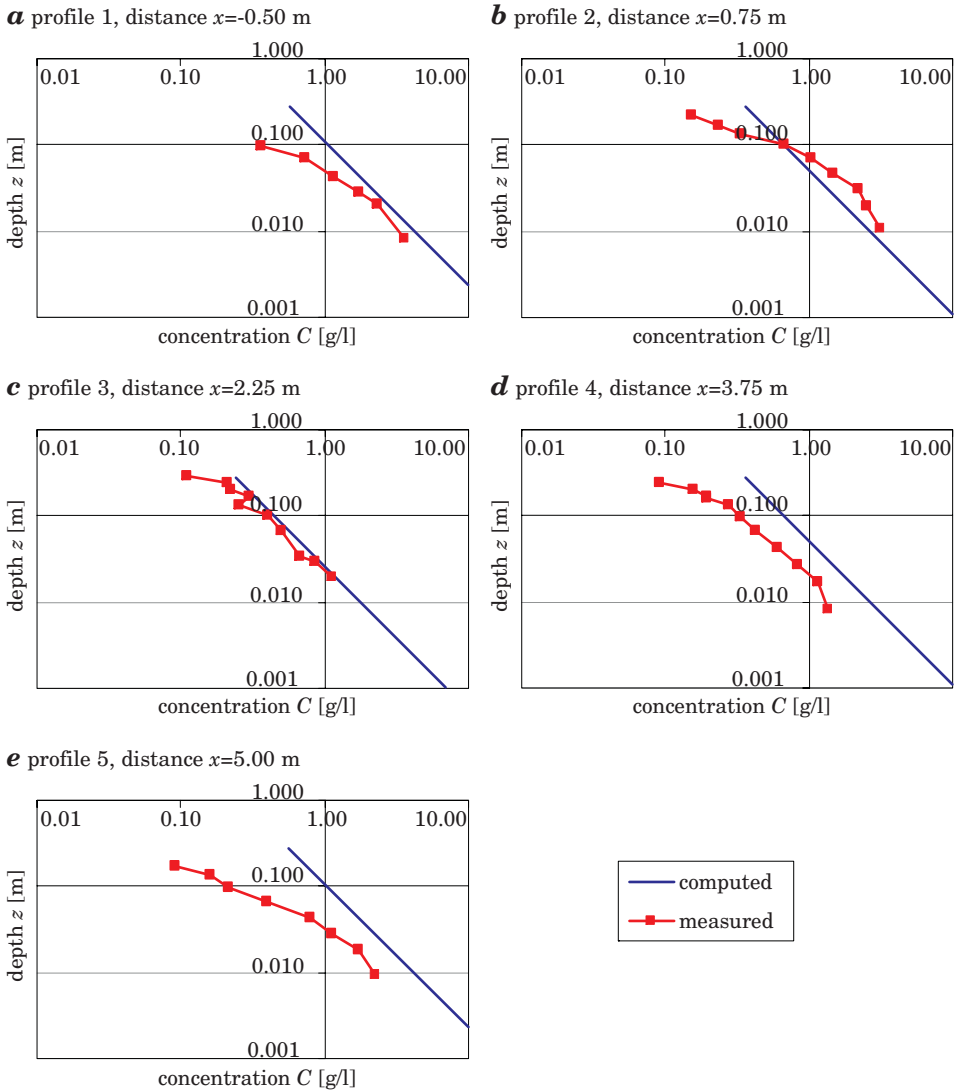


Fig. 4. Comparison of computed vertical profiles of suspended sediment concentrations for a regular wave with the ones measured during the experiment in five profiles set along the canal

The mathematical modelling of the vertical concentration of suspended sediments was completed for a symmetrical, regular (sinusoidal) wave. The calculated vertical concentration distributions were then compared with the results obtained during the experiment at five cross-sections located along the canal (Fig. 2). The measurement data from the experiment enabled us to

analyze the vertical concentration distributions within the range of weak hydrodynamic conditions, where the dimensionless friction (Shield's parameters – see Eq. 6) ranged between $0.13 < \theta_{2.5} < 0.23$. The values of Shield's parameter indicate that the bed was rippled.

Figure 4 compares graphically the computed vertical profiles of suspended sediment concentrations for a regular wave with the data obtained from experimental measurements taken in five perpendicular profiles set along the canal.

Figure 4 shows that at a distance very close to the bed, the concentration of sediments was not measured because the measuring devices were set up at some further distance from the bed due to the ripples between 0.01 and 0.02 m high (VAN RIJN 1986), which covered the bed.

The coincidence of the results of computations attained with the proposed theoretical model with the experimental data can be said to be satisfactory.

Modelling changes in the bathymetry and grain size distribution of sediments which made up the bed

Changes in the bed bathymetry were modelled in two stages, i.e. excluding changes in the grain size distribution induced by sediment transport from the considerations and taking such changes into account.

The results of modelling changes in the bathymetry without taking into consideration changes in grain size distribution are shown in Figure 5. It was assumed that the bed consisted of uniform sediment. Calculations were performed for two cases, i.e. when the bed consisted exclusively of grains 0.08 mm in diameter and when the bed was composed of grains of the diameter 0.13 mm. Because finer fractions are more intensively transported than coarser ones, the result of modelling finer sediment “escapes” beyond the scope of measurements. For coarser fractions, a change in the bathymetry is evidently slower. Let us take a representative diameter, e.g. $d_{50} = 0.10$ mm, then the consequent result of modelling will be comprised within the range of solutions obtained for the fractions 0.08 and 0.13 mm but will not agree with the experimental results, either.

Attempts to calibrate own computational models in order to “adjust” results of modelling with experimental results have been made by various research centres involved in the international project SANDPIT (VAN RIJN 2005). Models have been scaled for two approaches, *A* and *B* (WALSTRA 2005). The *A* problem dealt with attempts to adjust results of computations based on the measured values of transport loads, whereas the *B* approach relied on observations of the morphology of the bed. Results of modelling are presented for both approaches in Figure 6 (*A* approach) and Figure 7 (*B* approach).

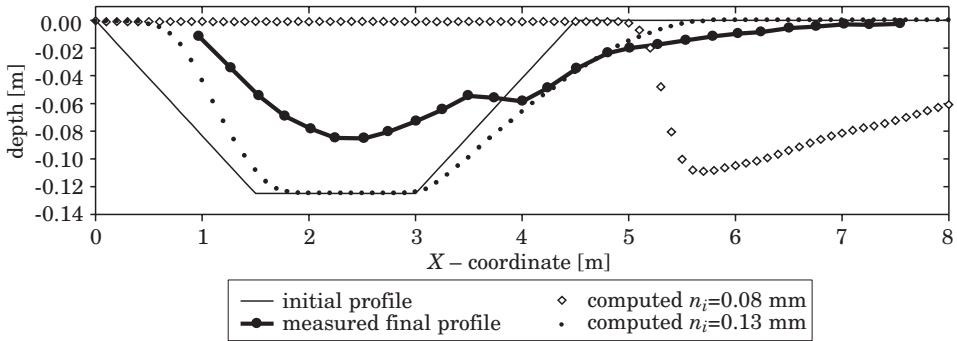


Fig. 5. Changes in the bed profile after time $T = 10$ h. Comparison with the results of modelling for non-uniform sediment

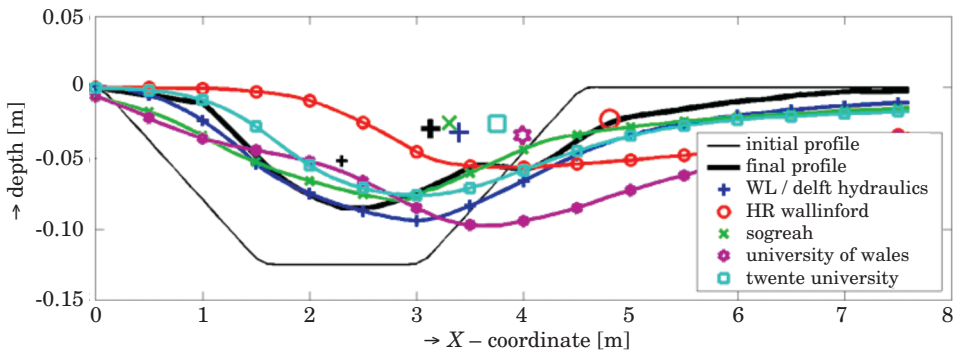


Fig. 6. Changes in the bed profile in time $T = 10$ hrs. A approach – calibration of models based on measured transport

Source: WALSTRA (2005).

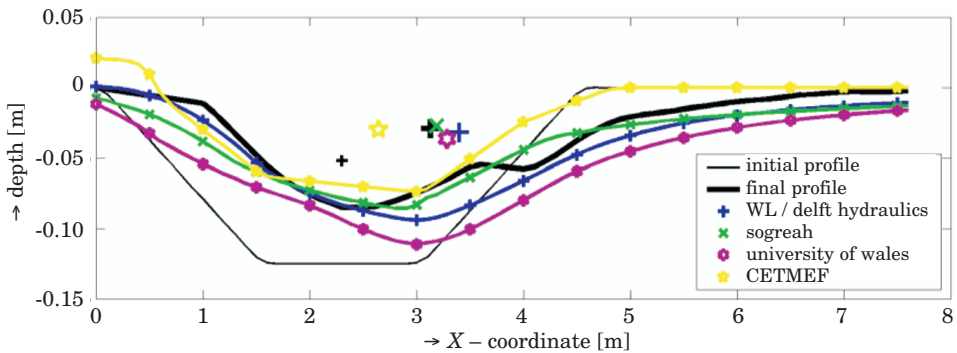


Fig. 7. Changes in the bed profile in time $T = 10$ hrs. B approach – calibration of models based on observations of the bed's morphology

Source: WALSTRA (2005).

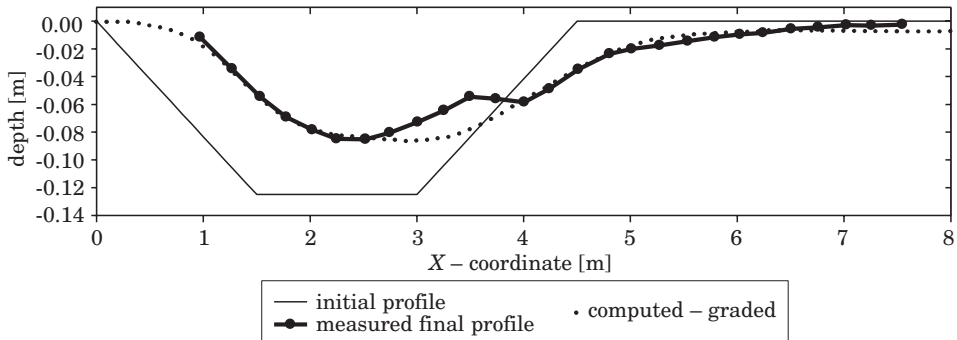


Fig. 8. Changes in the bed profile after time $T = 10$ hrs. Comparison of the results of modelling for non-uniform sediment (including changes in the grain size distribution) with measurements

Comparison of the results of modelling changes in the bathymetry according to the theoretical model presented in this paper for non-uniform sediment, including changes in the grain size distribution is shown graphically in Figure 8. The calculations were performed for three diameters (Fig. 3). As seen from the diagram, the coincidence between modelling the results and measurements was very close.

Figure 9 shows calculated changes in the grain size distribution in the bed sediment after time $T = 10$ h, in a longitudinal profile. In sites where sediment accumulated, a high increase in the share of finer fractions is observable, alongside a decrease in the coarser ones. the situation is reverse in eroded areas. This fact can be explained by more intensive transport of fine than coarse fractions.

Based on Figs 5, 8 and 9, a fundamental difference can be noticed in the reconstruction of the bed's profile due to transport of non-uniform and

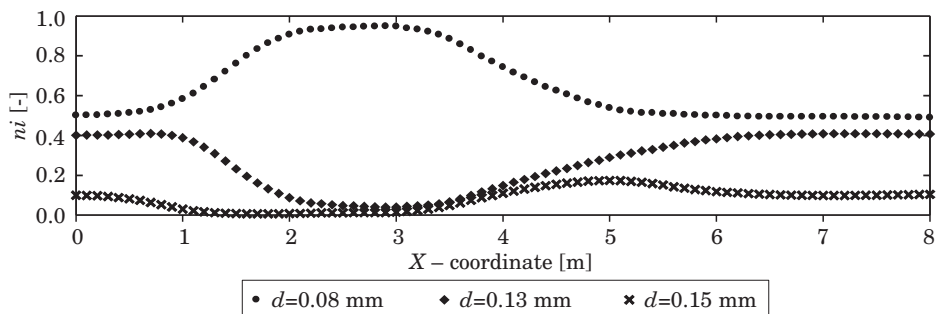


Fig. 9. Results of the modelling of grain size distribution changes after time $T = 10$ hrs

uniform sediments, including the influence of changes in the grain size distribution of sediments along the whole canal. It becomes evident that grading of sediments plays an important role in both sediment transport and sedimentation of a canal, not only in respect of the rate of sedimentation but also the character of changes in the canal's structure.

The agreement between the computational and experimental results can be treated as satisfactory, which proves that the computational model reflects well changes in the bed bathymetry and describes changes in grain size distribution of sediments. This, in turn, implies that the model enables us to predict accurately sedimentation of waterways.

Summary

The purpose of this paper has been to compare the results of modelling changes in the bed bathymetry around and inside a canal, constructed previously, during its sedimentation with the results yielded by a laboratory experiment, conducted in a wave flume under wave and current conditions. The calculations concerning the bed's morphology accounted for the time and space-related changeability of the grain size distribution of transported sediments. Further, the results of computations of the distribution of vertical concentrations of suspended sediments at different depths were compared. It was demonstrated that the effect of changes in the grain size distribution of sediments occurring during the process of sedimentation of waterways is extremely important. It was also revealed that the process of sorting out of sediments should be included in the modelling of changes in the bed bathymetry occurring in time and space. The mathematical model used in the calculations was a three-layer model of transport of sediments composed of non-uniform particles, derived by Kaczmarek (1999) according to the principle of conservation of water and sediment motion amounts in the nearbed layer.

The results of modelling of the changes on the bed bathymetry, presented in this paper, alongside vertical profiles of concentrations of suspended sediments agreed very well with the results produced by a laboratory experiment. Thus, the presented model of sediment transport can be recommended as a useful tool, which seems applicable to making prognoses about changes in the bed's bathymetry within waterways or to determination of grain size distribution of sediments which fill up a waterway as well as the rate of sedimentation of approach fairways to harbours.

References

- BIEGOWSKI J. 2006. *Dynamika osadów morskich o niejednorodnym uziarnieniu w świetle teorii i eksperymentu*. praca doktorska. IBW PAN.
- CHATELUS Y., KATOPODI I., DOHMEN-JANSSEN M., RIBBERINK J.S., SAMOTRAKIS P., CLOIN B., SAVIOLI J.C., BOSBOOM J., O'CONNOR B.A., HEIN R., HAMM L. 1998. *Size Gradation Effects in Sediment Transport*. Proc. 26th ICCE, ASCE, Reston VA, 2435–2448.
- DAVIES A.G., RIBBERINK J.S., TEMPERVILLE A., ZYSERMAN J.A. 1997. *Comparisons between sediment transport models and observations made in wave and current flows above plane beds*. Coastal Engineering, 31: 163–198.
- DEIGAARD R. 1993. *Modelling of sheet flow: dispersion stresses vs. the diffusion concept*. Prog. Rep. 74, Inst. Hydrodyn. and Hydraulic Eng., Tech. Univ. Denmark, pp. 65–81.
- FREDSOE J. 1984. *Turbulent boundary layer in combined wave-current motion*, J. Hydraulic Eng., ASCE, 110(HY8): 1103–1120.
- HASSAN W.N., KROEKENSTOEL D.K., RIBBERINK J.S. 2001. *Size-gradation effect on sand transport rates under oscillatory sheet-flows*. Proc. Coastal Dynamics '01, ASCE, Reston VA, ss. 928–937.
- KACZMAREK L.M. 1999. *Moveable Sea Bed Boundary Layer and Mechanics of Sediment Transport*. IBW PAN, Gdańsk.
- KACZMAREK L.M., OSTROWSKI R. 2002. *Modelling intensive near-bed sand transport under wave-current flow versus laboratory and field data*. Coastal Engineering, 45(1): pp. 1–18.
- KACZMAREK L.M., BIEGOWSKI J., OSTROWSKI R. 2004. *Modelling cross-shore intensive sand transport and changes of grain size distribution versus field data*. Coastal Engineering, 51(5–6): 501–529.
- KACZMAREK L.M., SAWCZYŃSKI SZ., BIEGOWSKI J. 2011. *Bathymetry changes and sand sorting during silting up of the channels. Part 1. Conservation of sediment mass*. Technical Sciences, 14(1).
- NIELSEN P. 1992. *Coastal bottom boundary layers and sediment transport*. Advanced Series on Ocean Engineering, 4, World Scientific, Singapore.
- DE MEIJER, R.J., BOSBOOM J., CLOIN B., KATOPODI I., KITOU N., KOOMANS R.L., MANSO F. 2002. *Gradation effects in sediment transport*. Coastal Engineering, 47: 179–210.
- RIBBERINK J.S., AL-SALEM A. 1994. *Sediment transport in oscillatory boundary layers in cases of rippled beds and sheet flow*. Journal Geoph. Res., 99(C6): 12707–12727.
- RIJN L.C. VAN 1986. *Sedimentation of dredged channels by currents and waves*. Journal of Waterway, Port, Coastal and Ocean Engineering, ASCE, 112(5).
- RIJN L.C. VAN, SOULSBY R.L., HOEKSTRA P., DAVIES A.G. 2005. *SANDPIT, Sand Transport and Morphology of Offshore Mining Pits*. Aqua Publications, The Netherlands.
- SAYED M., SAVAGE S.B. 1983. *Rapid gravity flow of cohesionless granular materials down inclined chutes*. J. Applied Mathematics and Physics (ZAMP), 34: 84–100.
- SISTERMANS P.G.J. 2001. *Multi-fraction net sediment transports by irregular waves and a current*. Proc. Coastal Dynamics '01, ASCE, Reston VA, pp. 918–927.
- WALSTRA D.J.R., CHESHER T., DAVIES A.G., RIBBERINK J., SERGENT P., SILVA P., VITTORI G., WALTHER R., RIJN L.C. VAN 2005. *Intercomparison of the State of the Morphological Models*. In: *SANDPIT Sand Transport and Morphology of Offshore Mining Pits*. Eds. Rijn L.C. van, Soulsby R.L., Hoekstra P., Davies A.G. Aqua publications, The Netherlands, ISBN 90-800356-7-X.

**A QUESTION OF BUILDING MATERIALS
AND CONSTRUCTION SOLUTIONS FOR
REVALORIZATION OF FRONTAGE TOWNHOUSES
IN THE CENTRE OF JEZIORANY**

***Joanna Pawłowicz¹, Michał Świrydow²,
Marta Adamczewska²***

¹ Chair of Civil Engineering and Building Constructions

² Students from the *Kreska* Club of Young Architects and Urban Designers affiliated with the Chair of Civil Engineering and Building Constructions
University of Warmia and Mazury in Olsztyn

Key words: revalorization and conservation of historical buildings, building materials, foundations, wall structures, intermediate floor structures, rafter framings, Jeziorany.

Abstract

In this paper, Jeziorany, a small town in the Province of Warmia and Mazury, serves as an example for discussing questions on building materials and construction solutions used in rows of townhouses dating back to the turn of the 17th and 18th century as well as in buildings raised in the town centre in the 1980s. Types of rafter framings, walls and foundations have been presented alongside a description of the building materials used when Jeziorany was rebuilt after a great fire which ravaged the town in 1783.

**MATERIAŁOWO-KONSTRUKCYJNE ASPEKTY REWALORYZACJI ZABUDOWY
PIERZEJOWEJ ŚRÓDMIEŚCIA JEZIORAN**

Joanna Pawłowicz¹, Michał Świrydow², Marta Adamczewska²

¹ Katedra Budownictwa i Konstrukcji Budowlanych

² Studenci z Koła Naukowego Młodych Architektów i Urbanistów „Kreska” działającego przy Katedrze Budownictwa i Konstrukcji Budowlanych
Uniwersytet Warmińsko-Mazurski w Olsztynie

Słowa kluczowe: rewaloryzacja, konserwacja zabytków, materiały budowlane, fundamenty, konstrukcje mурowe, stropy, więźby dachowe, Jeziorany.

Abstrakt

Na przykładzie niewielkiego miasta Jeziorany (woj. warmińsko-mazurskie) wykazano rozwiązania materiałowe i konstrukcyjne w zabudowie pierzejowej z przełomu wieków XVII i XVIII oraz w budynkach z lat 80. XX wieku. Przedstawiono rodzaje więźb dachowych, konstrukcji murowych oraz fundamentów, a całość uzupełniono opisem materiałów stosowanych w trakcie odbudowy Jezioran po pożarze, który w roku 1783 strawił je niemal doszczętnie.

Introduction

Since the earliest times, people have been engaged in raising constructions of different types, frequently showing great determination and amazing results. Old architecture can be regarded as art. As one admires a combination of different architectural schools and craftsmanship solutions seen in historic buildings, an inevitable question arises – how such a building was constructed in the former time and – more importantly – exists in the present day.

Jeziorany is a small town, with a population of less than 3.5 thousand. It lies in the eastern part of Warmia, on the Symsarna River. Apart from the river, there are also a few lakes situated in the environs of Jeziorany. The town was founded by the Bishop of Warmia, Herman of Prague, in 1310, but it had to wait 28 years before it was granted a charter. There are several listed buildings in Jeziorany, a town endowed with a long and interesting history. The town used to have a timber fortress, which in the 14th century was replaced by a brick castle – an identical copy of the castle in Działdowo (CZUBIEL, DOMAGAŁA 1969).

Originally, all the buildings in Jeziorany were made of timber, which often caused fires. After one such fire, which ravaged most of the castle and much of the town, the castle was demolished and the recovered building materials were used to raise a new building, which today houses the Councils of the Town and the Commune of Jeziorany. The whole town was reconstructed as a brick one, which in those times was a rare solution as brick was not a plentiful material. However, the most severe damage was inflicted to the town during the Second World War. Today, the post-war reconstruction and modern buildings seem to dominate in Jeziorany so that in many cases the beauty of the old architecture has become a backdrop for the contemporary one (ACHREMCZYK 1997).

The spatial layout of the town relies on a chequered pattern of streets, running perpendicularly towards the centrally located market square – a pattern which until the present day is clearly distinguishable. The town centre contains the most important edifices, such as the Town Hall, the castle and St Bartholomew Church raised in the Gothic style.

The residential area consisted of compact blocks of townhouses, which – owing to their historic ornaments – make Jeziorany an attractive although partly dilapidated town (Fig. 1, 2). Nonetheless, much of the historic architecture of the town has survived until our days (ZAGROBA 2009).



Fig. 1. A compact row of houses along one side of the main market square
Source: the authors.



Fig. 2. A compact row of houses along one side of the main market square
Source: the authors

Foundations

As the town was set up in the Middle Ages, the foundations were laid from the material popular in that time, such as insaturable stone and cement-lime mortar. These foundations have remained in good condition until the present time. However, their simple construction meant that they could bear only small buildings, such as simple townhouses, which are a dominant type of houses in the town. Figure 3 shows an example of stone foundations. Such foundations were made in a simple way, namely stones were laid at the bottom of a foundation trench and compacted with a wooden peg; afterwards, a layer of breakstone was placed over the stones and poured over with cement and lime mortar. Layer after layer were made until a desired height of the foundation base is reached (Architektura Sakralna Pomorza Zachodniego, 17.02.2011).

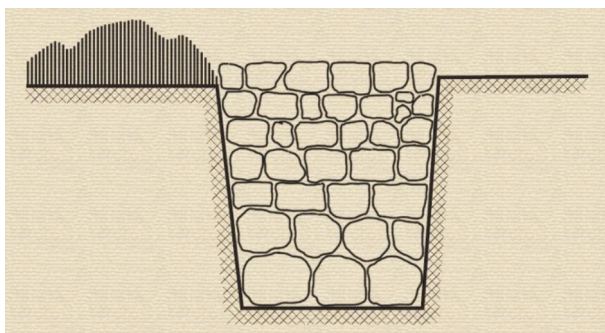


Fig. 3. A stone foundation

Source: Architektura Sakralna Pomorza Zachodniego, 17.02.2011.

Walls

The walls of the buildings in Jeziorany were made according to the then dominant construction technology. Solid clay brick was used, and outer walls were at least 1.5 brick thickness, which was both because of the construction requirements and lack of other insulation materials.

Among many possible brickwork bonds, the most common were the English (Fig. 4) and the Flemish bond (Fig. 5). Gypsum or lime mortar was used for making joints between bricks.

By laying the first course of bricks as headers and starting the second one with a queen brick (3/4 of a brick) followed by stretchers, a characteristic pattern called an anvil was obtained (Fig. 4). When the first course consisted of headers, the second started with a queen brick (3/4 of a brick), followed by a header and next a stretcher, a characteristic pattern of a cross appeared (Fig. 5).

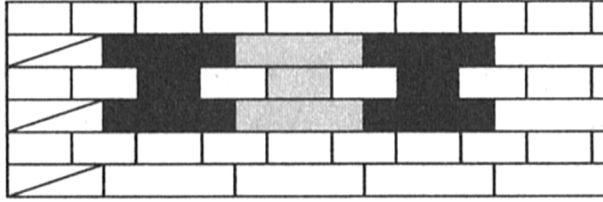


Fig. 4. The English brick bond Source: LICHOLA (2008).

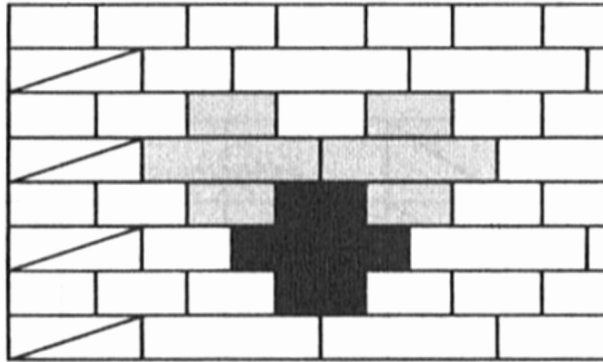


Fig. 5. The Flemish brick bond

Source: LICHOLA (2008).

Floors

Floors were constructed from the basic materials then available, such as timber. Floor constructions comprised timber floors with sound boarding (Fig. 6) or beam-frame floors (Fig. 7). Timber floors are easy to make, even in the wintertime, and provide high thermal insulation. The span of such floors should not exceed 6 meters and the joists should be spaced at a maximum distance of 1.2 meter. The floors were between 18 and 30 cm thick.

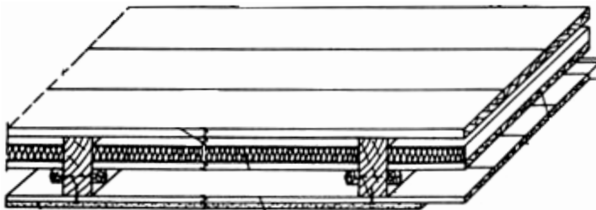


Fig. 6. A floor with sound boarding

Source: LICHOLA (2008).

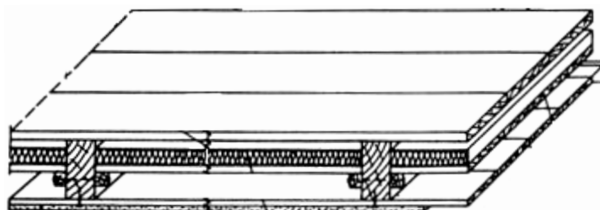


Fig. 7. A beam-frame floor

Source: LICHOLA (2008).

The floor with sound boarding has intermediate boards on which an insulation layer, which in the past meant pugging in the past, is placed. In the beam-frame floor, the insulation layer is laid directly on the sub-ceiling.

Roof structures

Most of the historic buildings in Jeziorany have pitched roofs. Pitched roofs were preferred for practical reasons (utilizable space in attics) and the climate (shedding rainwater and snow).

The small size of the townhouses and short spans of the outer walls enforced carpenters to make simple roofs. Most of the roofs are therefore gable, jerkin head gable (Fig. 8) or mansard structures (Fig. 9).

Most roofs are covered with clay tiles, which were very popular in East Prussia owing to rich resources of the raw material (clay). The most common roof structures (able to bear a heavy load of clay roof tiles) were collar beam roofs or strutted (Fig. 10) collar beam roofs (Fig. 11) with or without angle struts.



Fig. 8. A Jerkin head gable roof

Source: the authors.



Fig. 9. A mansard roof

Source: the authors.

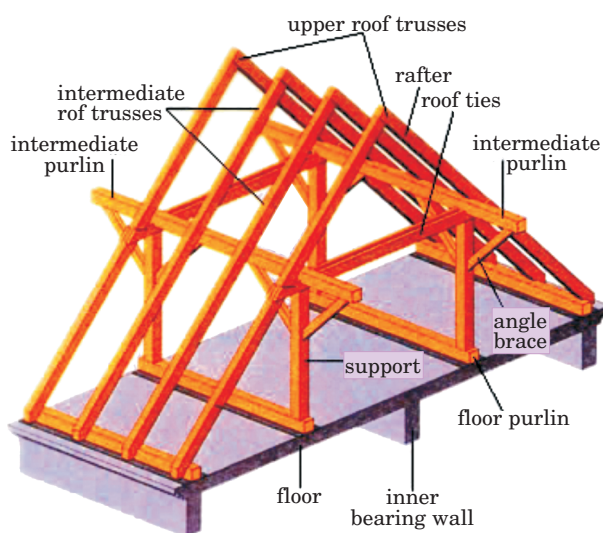


Fig. 10. A strutted collar beam roof

Source: Dachowy.pl, 15.07.2010.

In the later times, such as the 19th and 20th century, other, more complex roof construction were built. The townhouses were designed under the influence of such styles as the Neoclassicism, Pseudo-Classicism or Neo-Gothic (Fig. 12, 13) (Architektura Mieszkalna. Gmina Jeziorany, 14.02.2011).

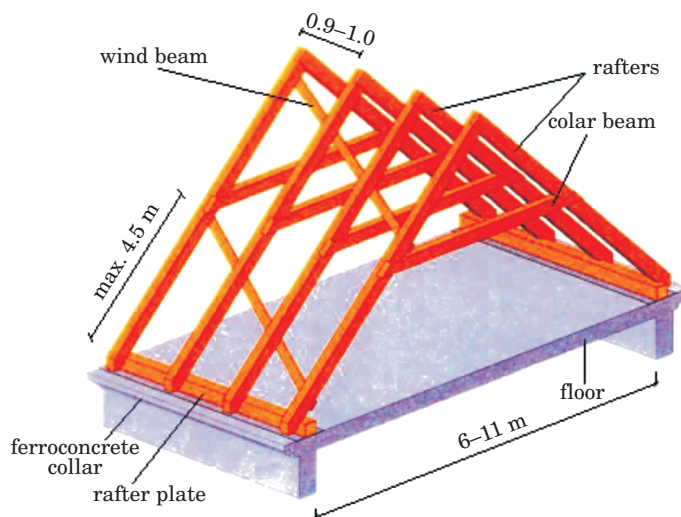


Fig. 11. A collar beam roof

Source: Dachowy.pl, 15.07.2010.



Fig. 12. A neo-Gothic "castle"

Source: the authors.



Fig. 13. Neoclassicism

Source: the authors.

Building materials

The buildings raised in Jeziorany, like in other historic town, were constructed from locally available materials. Brick, timber and stone were the basic building materials in the former days of Jeziorany.

Stone was used to make foundations. The outer walls, partition walls and stairs were built of brick. Timber was needed for constructing wooden-framed structures such as intermediate floors, stairs and roofs.

When renovating old buildings, apart from the building materials, the right colours of facades that should be selected. Using delicate, pastel colours, sometimes in contrasting combinations, as well as a rich variety of plants that should be an indispensable element of an urban landscape (PAWŁOWICZ 2006), will have a positive influence on the spatial management of Jeziorany, a town with a long and rich history.

Some examples of outstanding historic buildings in Jeziorany

Among some more interesting listed buildings in the town, noteworthy is the one that today houses the Councils of the Town and the Commune of Jeziorany (Fig. 14). It stands on a site where – prior to the fire of 1783 – stood a fortified castle (Fig. 15). Its stone foundations are the only remaining trace of the castle of the Bishops of Warmia. The walls are made from solid clay bricks and the roof construction – because of quite big spans between the walls – is a strutted collar beam roof with angle struts.



Fig. 14. The Councils of the Town and Commune in Jeziorany

Source: the authors.



Fig. 15. A sketch of the Castle of the Bishops of Warmia

Source: Jeziorany online 21.07.2010.

Another interesting building, dating back to the mid-14th century is the Gothic Church of St Bartholomew (Fig. 16). It was erected in the second half of the 14th century and is a classic example of a hall church with a one-storey high vestry built in medieval Warmia. The walls of the church are built of solid brick, laid in the Polish bond, on a low wall base made of field boulders. It is a five-bay church with two side aisles. The church has late-Gothic stellar vaults, which make up a pattern consisting of sixteen fields and over the nave and six ones over the side aisles. The vaults are supported by eight-sided pillars. The two sides of the gable wall facing the west are topped with pinnacles, while the gable walls of the vestry and the porch are crow-stepped ones with pinnacles on top of each crow step and decorated with lancet arched blind arcades. Analogously, lancet arched blind arcades divide the church spire into four storeys. The church door at the bottom of the spire is crowned by a lancet arch and has a recessed portal. Likewise, the portal leading from the nave to the vestry is lancet arched, recessed and fitted with a door featuring transverse slats crossing diagonally

and a 19th century door knocker in the shape of the head of a dog, which is a remaining element of the former decoration of the church and a rare example of the medieval fine art foundry. The church is classified as a second-class historic building (Jeziorany online, 21.07.2010).



Fig. 16. St Bartholomew's Church

Source: the authors.

Final remarks

The goal of revalorisation of historic buildings and conservation areas is to restore their practical and aesthetic values and to adjust the new buildings to the context of the historic surroundings. One should also bear in mind the traditional materials used in a given area. However, economic considerations are

another aspect of revalorisation of historic buildings when selecting some materials rather than others (ORŁOWICZ, SZAFRANKO 2004, SZAFRANKO 2000).

In Jeziorany, the dominant building materials are stone, different types of ceramic products, timber and plaster based on lime and sand mortar. In any action undertaken for the sake of regaining the former grandeur of the town, one should emphasize the use of traditional materials and wherever the so-called infill building has to be added, it should be designed in such a way as to complement the existing architecture. The right choice of building materials and colours for facades of buildings is an important component of revalorisation. The proposed colours should be subdued and matching the existing surroundings (ZAGROBA 2010).

Translated by JOLANTA IDŹKOWSKA

Accepted for print 23.09.2011

References

- ACHREMCZYK S. 1997. *Historia Warmii i Mazur*. Olsztyn.
- Architektura Mieszkalna. Gmina Jeziorany. <http://www.domwarminski.pl/content/view/94/147/> (14.02.2011).
- Architektura Sakralna Pomorza Zachodniego, www.architektura.pomorze.pl (17.02.2011).
- Budownictwo Ogólne. Elementy budynków-podstawy projektowania*. 2008. Ed. L. LICHOLA. Tom 3. Arkady.
- CZUBIEL L., DOMAGAŁA T. 1969. *Zabytkowe ośrodki miejskie Warmii i Mazur*. Pojezierze, Olsztyn. www.dachowy.pl, www.dachowy.pl (15.07.2010).
- Jeziorany online. Zabytki Jezioran. <http://www.jeziorany.com.pl/?id=zabytki> (21.07.2010).
- ORŁOWICZ R., SZAFRANKO E. 2004. *Wybrane techniczno-ekonomiczne aspekty napraw spękanych murów*. Przegląd Budowlany, marzec: 23–26.
- PAWŁOWICZ J. 2006. *Zieleń osiedlowa w rewitalizacji środowiska mieszkaniowego*. In: *Problemy rewitalizacji w gospodarce przestrzennej XXI wieku*. Ed. W. Czarnecki. Wydawnictwo Wyższej Szkoły Finansów i Zarządzania w Białymstoku 2006, pp. 183–188.
- SZAFRANKO E. 2000. *Ekonomiczne aspekty remontów w budownictwie mieszkaniowym*. IX Konferencja naukowo-techniczna „Problemy remontowe w budownictwie ogólnym i obiektach zabytkowych” Wrocław 7–9 grudnia, 459–465.
- ZAGROBA M. 2009. *Problemy funkcjonalno-przestrzenne w małych i średnich miastach Warmii*. In: *Specyfika odnowy małych i średnich miast w Polsce*. Ed. J. Poczobut. Stowarzyszenie Forum Rewitalizacji, Kraków, pp. 167–173.
- ZAGROBA M. 2010. *Historyczne układy przestrzenne małych miast Warmii i ich rola we współczesnym funkcjonowaniu obszarów śródmiejskich*, Technical Sciences, 13.

REVALORIZATION OF THE HISTORIC TOWN CENTRE OF JEZIORANY – SOME DESIGN-RELATED PROBLEMS

Marek Zagroba¹, Maciej Adamczewski², Marcin Czeberkus²

¹ Chair of Civil Engineering and Building Constructions

² Students from the *Kreska* Club of Young Architects and Urban Designers affiliated
with the Chair of Civil Engineering and Building Constructions
University of Warmia and Mazury in Olsztyn

Key words: architecture, urban studies, revalorization of historic buildings, revitalization, preservation of listed buildings and conservation areas.

Abstract

This paper deals with the question of revalorization (rehabilitation) of some fragments of the centre of a small town. The objective has been to discuss how two public squares in the centre of Jeziorany, such as the Old Town Market Square and Castle Square, are planned to be renovated. Both squares need to be re-arranged, modernized and given a special status. The concept of their renewal contains some ideas for the future use and management of these squares and for the shaping of the rows of buildings which flank them¹. The suggested solutions, once achieved, will prevent the progressing degradation of listed buildings and their surroundings, which in turn will improve the spatial order in the renewed area.

PROBLEMATYKA REWALORYZACJI ZABUDOWY ŚRÓDMIEŚCIA W JEZIORANACH – WYBRANE ASPEKTY PROJEKTOWE

Marek Zagroba¹, Maciej Adamczewski², Marcin Czeberkus²

¹ Katedra Budownictwa i Konstrukcji Budowlanych

² Studenci z Koła Naukowego Młodych Architektów i Urbanistów „Kreska” działającego
przy Katedrze Budownictwa i Konstrukcji Budowlanych
Uniwersytet Warmińsko-Mazurski w Olsztynie

Słowa kluczowe: architektura, urbanistyka, rewaloryzacja, rewitalizacja, konserwacja zabytków.

¹ This report contains some details from designs prepared by students associated in the *Kreska* Club of Young Architects and Urban Designers, the UWM in Olsztyn and selected elements of designs from B. Sc. dissertations prepared by Maciej Adamczewski and Marcin Czeberkus at the Chair of Civil Engineering and Building Constructions under the supervision of Marek Zagroba, Ph. D., M. Sc. (Arch).

Abstrakt

W pracy opisano zagadnienie rewitalizacji fragmentów przestrzeni śródmieścia małego miasta. Celem opracowania było przedstawienie planowanych zmian w przestrzeni dwóch placów publicznych w centrum Jezioran – rynku staromiejskiego oraz placu Zamkowego. Są to przestrzenie wymagające uporządkowania, modernizacji oraz nadania odpowiedniej rangi. Koncepcja rewitalizacji zawiera propozycje zagospodarowania placów oraz kształtowania zabudowy pierzejowej. Realizacja proponowanych rozwiązań zapobiegnie postępującej degradacji zabytkowych obiektów oraz terenów w ich otoczeniu, co doprowadzi do poprawy ładu przestrzennego.

Introduction

Jeziorany is a small town in Warmia, lying in the central part of the Province of Warmia and Mazury. It is the capital of the commune of Jeziorany (*gmina Jeziorany*). The town was founded in 1310 and granted a charter in 1338. Apart from the well-preserved medieval pattern of the streets, other material remnants of the town's history are St Bartholomew Church in the Gothic style, with an antique pipe organ, the Chapel of the Holy Cross, the 18th century Baroque Gatehouse, a Lutheran church and fragments of a castle raised by the Bishops of Warmia, such as vaulted cellars, on which the present-day building of the Town Council in Jeziorany stands.

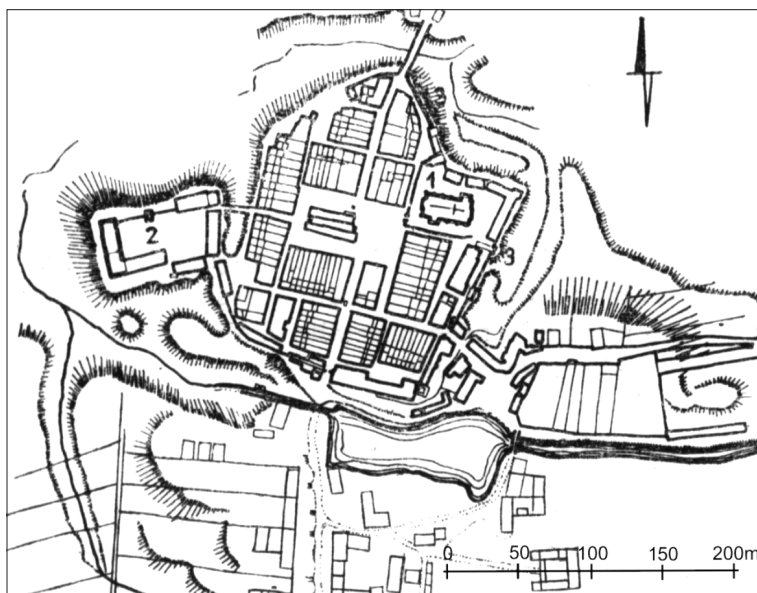


Fig. 1. The street plan of the centre of Jeziorany in the 1950s

1. St Bartholomew Church, 2 – the castle of the 14th – 19th century (today, the Town Council),
- 3 – fortified walls of the 14th century

Source: Czubieli L., Domagała T. (1969, s. 154).

Unfortunately, many historic buildings have not survived until our time. Among the causes is the fact that over the course of the centuries the town changed hands several times, being owned by Poland, Prussia, France or Sweden. But the major cause of destruction were repeated fires, for example in 1783 the town was ravaged by a great fire, which started when a lightning struck. Practically speaking, the whole town, including the castle, fell into ruin.

Revalorization (restoring the former value) as well as broadly understood revitalization of fragments of urban space are at present very popular solutions applied to the existing urban structure. Revalorization and revitalization comprise many technical aspects, and revitalization additionally includes some economic and social undertakings, whose aim is to improve the spatial order and to aid development of degraded areas. For small and often neglected towns, it is particularly important to be able to restore adequate functions of the town centre. This paper focuses on the spatial aspect of revitalization, and the actual reconstruction of two squares in the centre of Jeziorany. The renewal project encompassed the Old Town Market Square and Castle Square.

The design concept – the Old Town Market

Jeziorany is one of the many small towns which suffered much damage during the World War Two, later compounded by the post-war urban zoning, reconstruction and lack of adequate conservation of listed buildings. The sad consequences are evident on and around the Old Town Market Square in the way this space is managed today and how the buildings flanking the square have been reconstructed. The structure of the Old Town has been destroyed partly because some pre-war buildings have not been rebuilt and partly because they have been replaced by new buildings which completely disagree with the historic part of the town (Figs 2 and 3).

A road has bisected the square into a loosely arranged car park and a green area surrounded by streets. Today, the square seems oversized compared to the frontage houses, which is due to the lack of the Town Hall (which burnt down during the Swedish Deluge).

The preliminary stage when planning a revalorization project for the town centre consisted of analyzing iconographic materials documenting the former and present buildings around the square (Fig. 4) and making a photographic inventory of the current situation.



Fig. 2. Fragment of the west frontage of the Old Town Market Square
Photo: M. Zagroba.



Fig. 3. Fragment of the north frontage of the Old Town Market Square
Photo: M. Zagroba.



Fig. 4. The pre-war buildings on the Old Town Market Square in Jeziorany
Source: The Archives of the Municipal Office in Jeziorany.

The arrangement of the townhouses with their roof ridges parallel to the streets, the small-scale houses and narrow land plots, the rhythm of doors and windows as well as historicizing details have all superimposed the way in which the new buildings completing gaps between the existing ones have been designed and the ones which disagree with the historic houses have been re-designed. Most of the proposed changes concern the west frontage of the square and new buildings in the north frontage. The designed architectural solutions draw on the historic buildings, and are therefore an attempt at connecting the rows of houses along each side of the market square (Figs 5, 6).



Fig. 5. The buildings along the north frontage of the square – the current situation



Fig. 6. The buildings along the north frontage of the square – a revalorization concept
 Source: A concept for the revalorization of buildings in the town centre of Jeziorany. The design made by students associated in the the *Kreska* Club of Young Architects and Urban Designers, the UWM in Olsztyn, in 2010.

In addition to the suggested designs of houses, a new surface of the square and some street furniture have been proposed. By suggesting to pave the surface with small stone blocks and cobbles it is hoped to achieve the benefits attributed to using natural building materials. Besides, some interesting patterns on the paved surface can be created.

Among the street furniture, noteworthy is the irregular layout of the walls of the town hall, as a memento of the former building. This solution carries a symbolic meaning and important information.

The town centre can be viewed as a landmark, and when small towns or villages are involved, like Jeziorany, this function is highlighted by the presence of offices, a church, shops and services. The renewal of the buildings around the market square is of great importance to the whole structure of Jeziorany. Through a harmonious combination of contemporary houses with listed buildings we can highlight the small-town character of Jeziorany.

The design concept for Castle Square

Castle Square occupies another part of the town centre in Jeziorany. It lies near the Old Town Market Square and likewise needs to be re-arranged in order to gain an appropriate status (Fig. 7). Castle Square is important for the whole town because of the Town Council, which stands here, on the foundations of the former medieval castle. The concept of the renewal of the square encompasses suggested modernization of the square, the Town Council building and the rows of houses along the sides of the square.

The function of the square has changed over the years. Originally, it was a castle ward; today it is mainly a car park for the council staff and customers.



Fig. 7. Castle Square in Jeziorany – the current situation

Photo: M. Adamczewski.

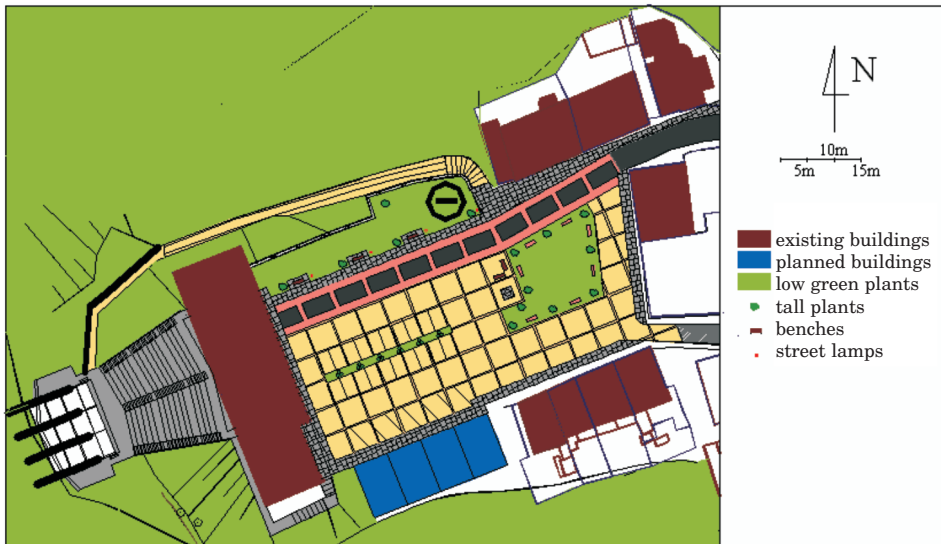


Fig. 8. A management concept for Castle Square in Jeziorany

When re-designing the square, the current accessibility requirements were taken into consideration as well as the need to preserve its role as a stately space. One-way traffic was suggested alongside some car parks in the central and southern part of the square. The road surface and footpaths are to be paved with stone blocks and cobbles in colours resembling the actual tint and texture of stone used for paving roads in the past (Fig. 8). The pattern of the square surface puts emphasis on a broken axis leading from the market place to the Town Council, which helps to associate the two public spaces.

Elements of street furniture have been included in the management plan. Drawing on the historical iconographic documents, it has been suggested to reconstruct a well in the middle of the square and a fortified building, such as a keep, in the northern part of the area. It is also presumed that the square will be illuminated at night. There will be some historically styled benches placed on the square.

Moving on from the market place towards Castle Square, we notice a protruding fragment of the row of buildings along the north side of the square. It consists of residential houses, one- or two-storey tall, with gable and pediment roofs, and with partly habitable or completely unused attics (Fig. 9). The revalorization of these building should include converting the attics into habitable space, adding more light to the existing interiors, tampering with the facades by changing the colour of the walls, bringing some order to the whole composition and completing the missing architectural ornaments.



Fig. 9. Castle Square – the north frontage

Photo: M. Adamczewski.

By converting the attics into habitable lofts, the residents will be offered more living space and the roofs will be enlivened with the added dormer windows and skylights. The renovation of the facades will consist in restoring the plinth wherever missing as well as adding cornices and door and window trims. In some of the buildings, it is planned to build roofs over the entrance doors. The walls are to be painted in light, pastel colours, but in some places applied in contrasting combinations.

Similar design-related solutions have been suggested for the east and south frontages of the square (Fig. 10). The idea is not to interfere with the existing state so as to be able to carry out the renewal plan at a relatively low cost.



Fig. 10. The north frontage of Castle Square – the current situation and the revalorization concept
Author: M. Adamczewski.

The most prominent building located at Castle Square is the one housing the Town Council. This is a three-storey building with a hipped roof, visually divided into two parts, which occupies the whole west frontage of the square (Fig. 11). In order to emphasize the stately function of the building, a historicizing, columned portico crowned by a tympanum with the town's coat of arms featuring in the middle has been designed. Several other architectural ornaments contribute to the whole design, such as cornices between the storeys and under the roof or door and window trims (Fig. 12).



Fig. 11. The Town Council in Jeziorany – the current state
Photo: M. Adamczewski.

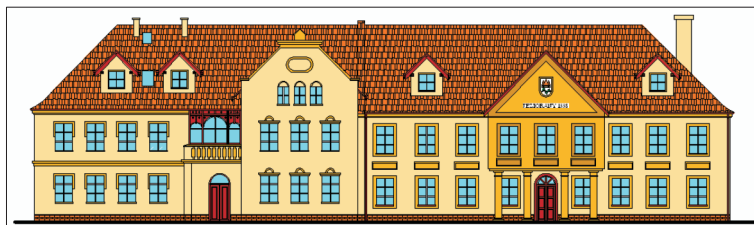


Fig. 12. The Town Council in Jeziorany – the revalorization concept
 Author: M. Adamczewski.

Among the greatest advantages of the planned revalorization of this building is the idea of assigning a new function to the medieval vaulted cellars underneath the building, the only surviving fragment of the former castle of the Bishops of Warmia. The project assumes that the cellars could be renovated and converted to house either a stylish restaurant or a registrar hall for wedding ceremonies.

Conclusions

Jeziorany is a good example of a town which – due to a number of various factors – has somehow lost its character of a town with centuries-long history and building tradition. The remaining fragments of the architecture in its centre document the latter. The renewal of the Old Town Market Square and Castle Square could give the town a chance to improve the way its centre looks like and functions today. The changes, once carried out, will affect the processes contributing to creating a true town centre by shaping a friendly space with new opportunities for development. The suggested solutions, which aim at correcting the urban structure and enhancing the architecture in the town centre, once supported by the local council, could serve as a foundation for developing a more detailed plan for the renewal of the town centre in Jeziorany. Based on the assumptions expressed in the present design, the following conclusions can be drawn, which could also be taken as guidelines for improving the town's image:

- improvement of the spatial structure of the town squares (urbanistic and architectural changes) positively affects the town's image and the public functions the town performs,
- the functions of the town centre (shops, services, housing) proposed to be located in the buildings flanking the two squares help to create a true town centre, in a way that is adequate for the discussed space,

– the small-town character of the discussed area is emphasized by small houses, fine divisions and subtle ornaments. The proposed contemporary architecture goes well with the historic buildings.

The street furniture is an element contributing to the attractiveness of urban spaces (the market place and Castle Square). The suggested materials and colours correspond to the atmosphere of a centre of a historic town.

Translated by JOLANTA IDŹKOWSKA

Accepted for print 29.09.2011

References

- CZUBIEL L., DOMAGAŁA T. 1969. *Zabytkowe ośrodki miejskie Warmii i Mazur*. Pojezierze Olsztyn, p. 154.
- Komunikaty Mazursko-Warmińskie*. 1987. Stacja Naukowa Polskiego Towarzystwa Historycznego, Olsztyn, p. 6–7.
- PAWŁOWICZ J. 2006. *Zieleń osiedlowa w rewitalizacji środowiska mieszkaniowego*. In: *Problemy rewitalizacji w gospodarce przestrzennej XXI wieku*. Ed. W. Czarnecki. Wyd. Wyższej Szkoły Finansów i Zarządzania w Białymstoku. Białystok, p. 183–188.
- Skalski K. 1999. *Rewitalizacja dawnych dzielnic, prezentacja doświadczeń polskich*. Świat nieruchomości, 26.
- SZAFRANKO E. 2000. *Ekonomiczne aspekty remontów w budownictwie mieszkaniowym*. IX konferencja naukowo-techniczna: „Problemy remontowe w budownictwie ogólnym i obiektach zabytkowych”, Wrocław, p. 459–465.

**ANALYSIS OF THE POSSIBILITIES FOR APPLYING
THE ASG-EUPOS SYSTEM SERVICES
FOR ESTABLISHING THE DETAILED CONTROL
NETWORKS**

Mieczysław Bakuła, Rafał Kaźmierczak, Grzegorz Grunwald

Chair of Satellite Geodesy and Navigation
University of Warmia and Mazury in Olsztyn

Key words: ASG-EUPOS, NAWGEO, POZGEO, POZGEO_D, RTK, GPS, GLONASS.

Abstract

The paper presents analyses and comparisons of coordinates' determination accuracy using ASG-EUPOS system real time (NAWGEO) and post-processing (POZGEO and POZGEO_D) services in the context of establishing detailed control networks. The survey of the detailed land survey network was conducted during construction of the national road S22 in its section Elbląg-Chruściel. At the first stage of the research static GNSS surveys were conducted using four Topcon HiPer Pro receivers. Almost all the points of the land survey network were stabilized in location with good availability to satellites. Only in the vicinity of some points, at the distance of around 10 meters, trees were situated. Processing of the observations was conducted by post-processing using the Topcon Tools software for 30–40 minute sessions using the observations from the network of fixed reference stations of POZGEO_D service. Additional static sessions were also processed using the POZGEO service. At the second stage of the study, RTK surveys using the ASG-EUPOS system NAWGEO service by applying two Topcon HiPer Pro receivers where one of them determined the position on the base of the single physical reference station while the other used the VRS network observations were conducted on the same points of the detailed network. The paper contains comparative analyses of the coordinates obtained and of their accuracy.

**ANALIZA MOŻLIWOŚCI WYKORZYSTANIA SERWISÓW SYSTEMU ASG-EUPOS
DO ZAKŁADANIA SZCZEGÓŁOWYCH OSNÓW GEODEZYJNYCH**

Mieczysław Bakuła, Rafał Kaźmierczak, Grzegorz Grunwald

Katedra Geodezji Satelitarnej i Nawigacji
Uniwersytet Warmińsko-Mazurski w Olsztynie

Słowa kluczowe: NAWGEO, POZGEO, POZGEO_D, ASG-EUPOS, RTK, GPS, GLONASS.

Abstrakt

W pracy przedstawiono analizy i porównania dokładności wyznaczeń współrzędnych z wykorzystaniem serwisów czasu rzeczywistego (NAWGEO) i postprocessingu (POZGEO i POZGEO_D) systemu ASG-EUPOS w kontekście zakładania szczegółowych osnów geodezyjnych. Pomiar szczegółowej osnowy geodezyjnej wykonano podczas budowy drogi krajowej S22, na odcinku Elbląg – Chruściel. W pierwszym etapie badań wykonano pomiary statyczne GNSS z wykorzystaniem 4 odbiorników Topcon HiperPro. Prawie wszystkie punkty osnowy geodezyjnej były stabilizowane w miejscach o dobrym dostępie do satelitów. Tylko w pobliżu niektórych punktów w odległościach około 10 metrów znajdowały się drzewa. Obserwacje opracowano w procesie postprocessingu z wykorzystaniem oprogramowania firmowego Topcon Tools, dla sesji 30–40-minutowych, z wykorzystaniem obserwacji sieci stacji referencyjnych serwisu POZGEO_D. Dodatkowo sesje statyczne opracowano także z wykorzystaniem serwisu POZGEO. W drugim etapie badań, na tych samych punktach osnowy szczegółowej, przeprowadzono pomiary RTK z wykorzystaniem serwisu NAWGEO systemu ASG-EUPOS dwoma odbiornikami Topcon HiperPro – jeden z nich wyznaczał pozycję na podstawie pojedynczej fizycznej stacji referencyjnej, natomiast drugi z wykorzystaniem sieciowych obserwacji VRS. Praca zawiera analizy porównawcze otrzymanych współrzędnych i ich dokładności.

Introduction

Appropriate determination of the ambiguity of phase surveys is necessary for precise determination of the GPS baseline coordinates from satellite observations (MISRA, ENGE 2006). This is the necessary condition, but in case of the limited access of the GPS receiver antenna to the satellites the determinations of ambiguities may be incorrect for a given pair of satellites, which results in appearance of gross errors (BAKUŁA et al. 2009). Erroneous determination of the baseline coordinates can be detected in the process of GPS baselines adjustment in case of the appropriate number of redundant observations and appropriate tying to the network of reference points (BAKUŁA et al. 2007, 2008). The possibility of obtaining high accuracy of the satellite survey results is influenced by numerous factors related not only to the type of equipment used but, first of all, the methodology of planning and performance of satellite observations. The GPS observations processing method, i.e. the choice of the appropriate methodology for processing the GPS baselines and next conducting the detailed analysis of their correct determination has also a significant influence on the obtained accuracies and reliability of the coordinates determined. Only in case of the appropriately planned network of GNSS baselines and redundant observations, we can obtain reliable analysis of accuracies in the process of GPS baselines adjustment (HOFMANN-WELLENHOF et al. 1997) and that is why, at actually every stage of survey and processing of satellite observations independent control should be applied and redundant observations should be used. The paper presents the accuracy analysis of coordinates obtained from processing the GPS/GLONASS network using the

POZGEO_D service as well as using GPS observations and the POZGEO service only. Additionally, at each point two independent RTK/GPS sessions were conducted using the ASG-EUPOS system NAWGEO service (BOSY et al. 2008). The detailed land survey network developed fulfilled the additional function of the implementation network with the required internal accuracy of horizontal coordinates at the level of 10 mm. Achievement of such accuracy is difficult, particularly when the survey is conducted where the access to satellites is limited.

Description of field survey

The land survey network along the road S22 in the section Elbląg – Chruściel was the test object during the experimental survey works. Within the frameworks of the experiment survey was conducted on 35 points (Fig. 1) where on the majority of points good survey conditions for satellite observations were available. The field experiments were divided into two stages. Stage one involving survey on the determined points by static method was conducted on October 5, 2010. Four land survey Topcon HiPer Pro GNSS receivers were used for static survey.

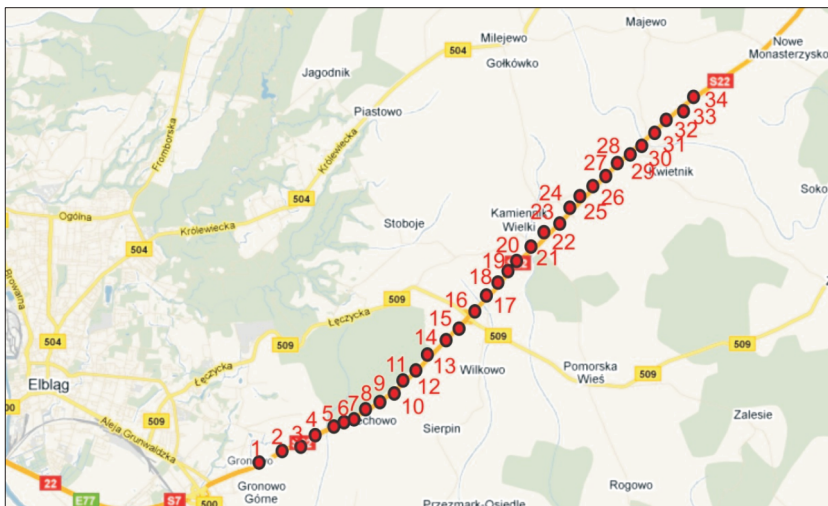


Fig. 1. Location of the control points on the object surveyed

The survey sessions duration depended on observation conditions on the point and ranged from 30 to 45 minutes. Table 1 presents the distribution of points for measurement into individual survey sessions.

Table 1

Distribution of the surveyed detailed network points according to the survey session

Session	Point No.	Point No.	Point No.	Point No.
1	1	2	4	–
2	3	5	6	7
3	8	9	10	11
4	12	13	14	15
5	16	17	18	19
6	20	21	22	23
7	24	25	26	27
8	28	29	30	Kon_168
9	31	32	33	34

Raw observations recorded by Topcon receivers were converted to the standard RINEX (*Receiver Independent Exchange*) data exchange format using the JPS2RIN.EXE software. The observations obtained from the static survey were processed in two ways. The first one involved post-processing and network adjustment using the commercial Topcon Tools software. For the purpose of tying the network the observation data from the station in Elbląg (ELBL), and two virtual stations (Vir5, Vir6) was downloaded from the POZGEO-D service (Fig. 2).

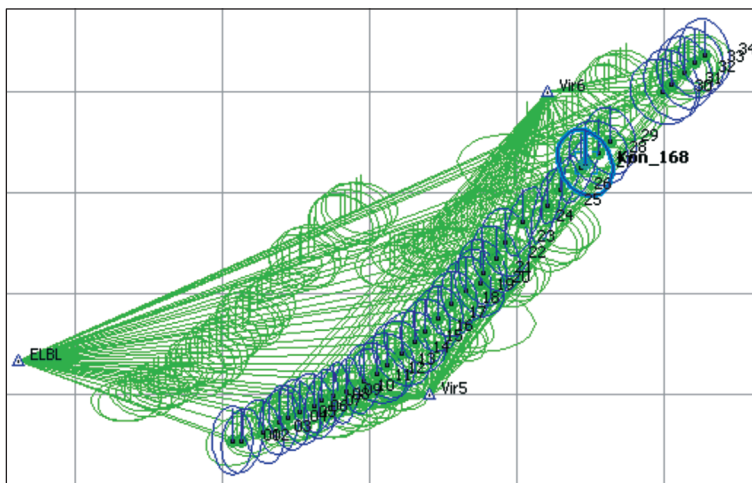


Fig. 2. Network of the adjusted baselines from post-processed static GNSS sessions

The adjustment process was conducted using the least squares method in relation to all three reference stations. The mean errors of coordinates of the points after adjustment did not exceed 5 mm while the values of the residues for the GPS/GLONASS baselines did not exceed 29 mm.

Determination of the coordination of points by POZGEO service was the second method for processing the static survey results. In this case, at the first stage of the analysis the observations from complete survey sessions (further referred to as the long sessions) were sent to the ASG-EUPOS system while in the second stage the observation files shortened to 15 minutes (with one second survey interval) were sent. The TEQC (The Toolkit for GPS/GLONASS/Galileo/SBAS Data) software was used for dividing the files.

Stage two of the survey was conducted on November 24, 2010. It involved measurement of all the determined points by means of the RTK method using two Topcon HiPer Pro receivers and the ASG-EUPOS system NAWGEO service. One of the receivers determined the position on the base of a single reference station situated in Elbląg (ELBL station) while the other receiver used observations from the virtual reference stations (VRS) selected automatically by the mobile receiver software.



Fig. 3. Survey of points by means of the RTK method

Analysis of processing of the points using the ASG-EUPOS system post-processing services: POZGEO_D and POZGEO

Stage one of the analysis involved comparison of the coordinates of points obtained from the POZGEO service for two different durations of sessions: 15 minutes (i.e. 900 survey epochs) and 30–40 minutes (full lengths of sessions carried out on individual points). The largest differences of coordinates occurred on point number 1 amounting to 2,891 m for the x coordinate, 1,192 for the y coordinate and 3,728 for the h coordinate. Presence of such gross errors was probably caused by obstructions at that point (Fig. 4a); the analyses of accuracies for the computed coordinates obtained from the POZGEO service for the above points did not indicate any problems with their determination

(Tab. 2), i.e. estimated accuracies were very small at the level of 1–3 cm. Point 25 situated in the vicinity of the middle voltage power line (Fig. 4b) was the second point in which large differences of coordinates, exceeding significantly the service accuracy characteristics, occurred. The differences of coordinates obtained for the remaining points oscillated within the 10 cm range (Fig. 5).

Table 2
Point determination accuracy analysis performed in the ASG-EUPOS system obtained from the system report

Point number	Long session					15-minute session				
	System 1992 X	System 1992 Y	mx	my	mp	System 1992 X	System 1992 Y	mx	my	mp
1	697662.165	530108.769	0.012	0.000	0.012	697659.274	530107.577	0.029	0.001	0.029
25	702021.596	535882.734	0.006	0.009	0.011	702021.865	535882.010	0.010	0.020	0.022



Fig. 4. Obstructions from the northern side on point 1 (Fig. 4a) and medium voltage transmission line near the point 25 (Fig. 4b)

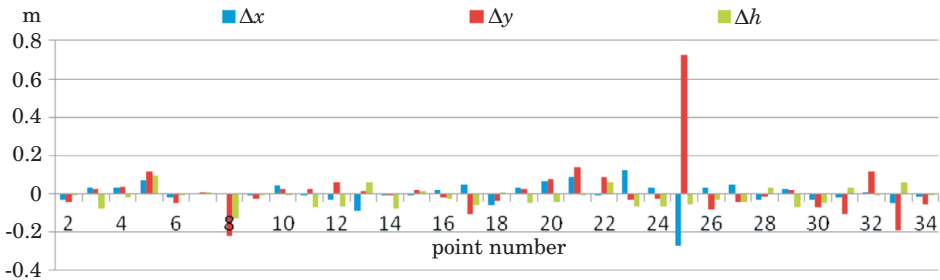


Fig. 5. Differences of coordinates obtained from processing the long and the 15 minute sessions in the POZGEO service

For transparency of the above figure, point one for which the analysis of the results obtained showed major differences in the coordinates was omitted. Analysis of the minimum and maximum values of the coordinates' differences (obtained from the POZGEO service for long and for 15-minute sessions) for the remaining points determined are presented in Table 3, except for points 1 and 25 in case of which gross errors in computations using the POZGEO service were observed in case of short static sessions.

Table 3
Minimum and maximum values from comparison between two computations

Specification	Δx [m]	Δy [m]	Δh [m]
Min.	-0,086	-0,220	-0,128
Max	0,124	0,137	0,092

Comparison of the coordinates originating from the POZGEO service with the coordinates obtained from the post-processing using the POZGEO_D service showed again the largest differences in coordinates for points 1 and 25. The differences of coordinates for point 1 are presented in Table 4.

Analyses of the comparison of points' coordinates obtained from the POZGEO service (long and 15-minute session) with own computations made using the Topcon Tools software are presented in Figure 6. Point 1 was not included in Figure 6 for which the differences were expressed in meters (Table 4).

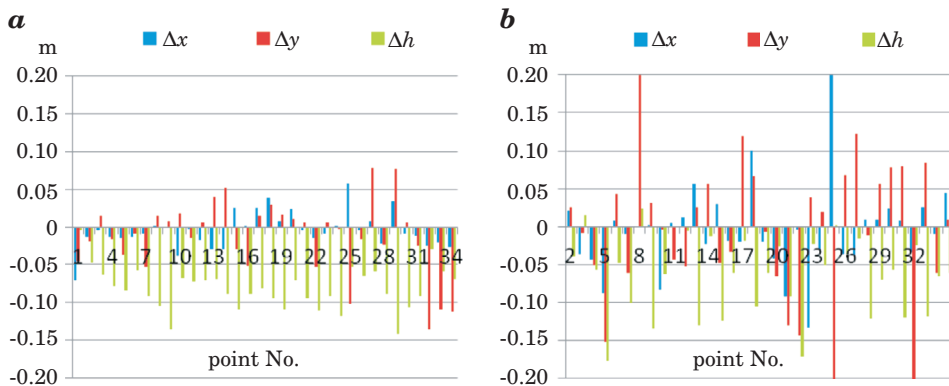


Fig. 6. Differences of coordinates obtained from the POZGEO service from a long session (a) and 15-minute session (b) and the coordinates obtained from the post-processing (Topcon Tools software)

Table 4
Differences in the coordinates for the first point in case of different computation variants

Specification	Own computations – POZGEO computations for long session [m]			Own computations – POZGEO computations for 15-minute session [m]			15-minute session from POZGEO – own computations [m]			15-minute session from POZGEO – RTK (344-0419 receiver) [m]			15-minute session from POZGEO – RTK (344-0391 receiver) [m]			15-minute session from POZGEO – RTK from 2 receivers [m]		
	Δx	Δy	Δh	Δx	Δy	Δh	Δx	Δy	Δh	Δx	Δy	Δh	Δx	Δy	Δh	Δx	Δy	Δh
Point	-0,071	-0,046	-0,004	2,891	1,192	-3,728	-2,962	-1,238	3,724	-2,956	-1,232	3,747	-2,966	-1,229	3,776	-2,961	-1,230	3,745

Comparative analyses of network points processing using the POZGEO_D and NAWGEO services

For the purpose of verification of the results obtained, on the determined points the additional survey using two GNSS Topcon HiPer Pro receivers by means of the RTK method and applying the ASG-EUPOS system NAWGEO service was conducted. In the first receiver the network solution of VRS (RTCM 3.1) service was applied while in the second receiver the data from a single reference station (ELBL station in Elblag) was used. The mobile telephone set Motorola V547 and IGTS-R (mobile GSM/GPRS/EDGE module) were used as modems assuring the GPRS connection. For each point 120 survey epochs with the 1-second interval were recorded. On the base of the data obtained the mean coordinates for each point were determined. The comparison of the coordinates obtained from two GNSS receivers showed similar results to the real time NAVGEO service that oscillated within the range of 2–3 centimeters in case of both using the observations from one reference station and from the virtual reference station (Table 5, Fig. 7).

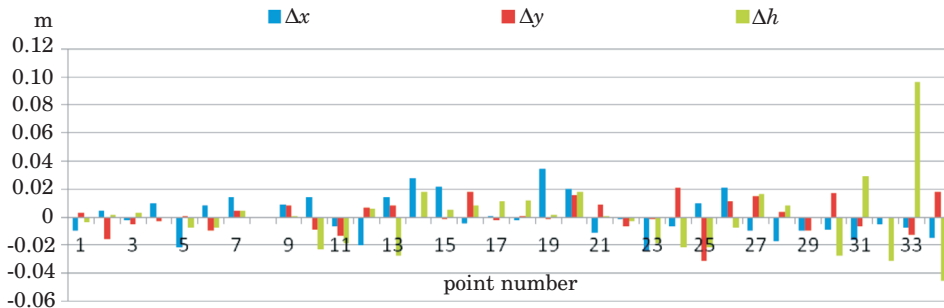


Fig. 7. Differences of the averaged coordinates from surveys conducted using two RTK receivers

Table 5
Minimum and maximum values of the results obtained

Specification	Δx [m]	Δy [m]	Δh [m]
Min.	-0,024	-0,031	-0,046
Max	0,034	0,021	0,096

Point 8 was not included in the comparisons because of the construction works that were in progress during the RTK survey. The differences of horizontal coordinates from RTK survey between two receivers oscillated within the range of 2–3 centimeters, which is within the accuracy ranges of the ASG-EUPOS system RTK services.

The mean coordinates from survey (by means of two receivers) using the RTK method were compared with the results obtained from static sessions post-processed using the POZGEO_D service (Fig. 8) and POZGEO service (Fig. 9), using all the GNSS observations, i.e. the long sessions. The coordinates of baselines between points determined were determined using the GPS and GLONASS observations.

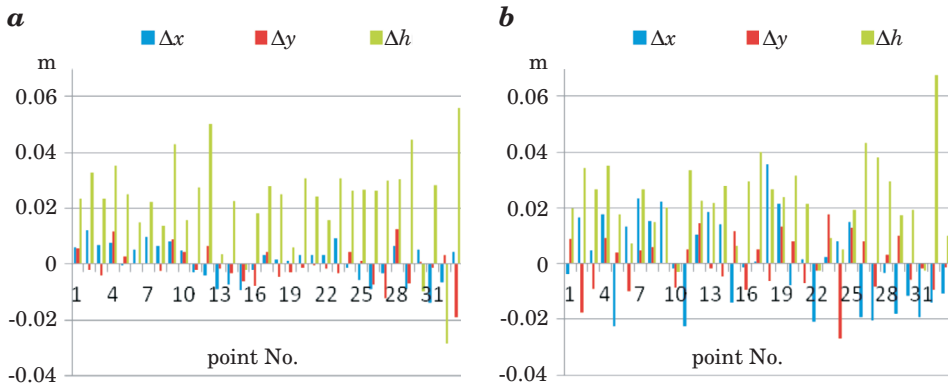


Fig. 8. Differences in coordinates obtained from the post-processing and from RTK survey

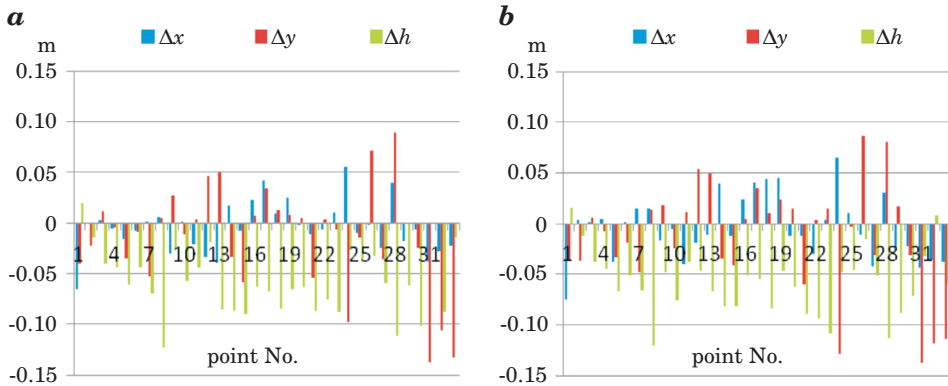


Fig. 9. Differences in coordinates obtained from the POZGEO service (long session) and from RTK survey

Analyzing all the comparisons of the surveys made using the RTK method with the results obtained from static observations it may be concluded that the RTK surveys obtained centimeter agreement with the coordinates obtained from static results for long sessions. This means that RTK surveys may represent excellent control for the results originating from rapid static surveys

where any obstructions exist. This allows identification of possible gross errors. In such cases, however, application of synchronic static sessions and adjustment of satellite observations as networks and not as an individual point would be recommended. In case of the results processed using the POZGEO service (for 15-minute sessions with one second survey interval) the coordinates obtained by means of the RTK method are more reliable and are characterized by significantly higher accuracy.

Summary and conclusions

The comparative analyses conducted for the different survey methods and data processing methods indicated that the highest accuracy of coordinates; determination for the position can be assured by conducting the computations in post-processing. The possibility of generating observations for any virtual (VRS) stations from the POZGEO_D service is highly useful as a tool in post-processing. It offers the possibility of optimal network configuration. In case of computations that are conducted for the user by the POZGEO service the results obtained are satisfactory in case of long survey sessions only. Using the POZGEO service, each time we determine the coordinates for one point only. Each of the consecutive determined points is not tied to any network points and as a consequence the differences and jumps in the values of coordinates are difficult to control. The results of determination of coordinates using the POZGEO_D and POZGEO services are similar for points with the unobstructed horizon. Problems appear in case of short sessions and points with obstructions. In the above analyses such problem appeared in case of points 1 and 25 where obstructions in the form of trees and medium voltage power line existed. Determination of the coordinates of points by means of the RTK method was a very good method for verification and elimination of gross errors. The differences of coordinates between the computations in post-processing and the RTK surveys were within the accuracy limits assumed for the RTK services of the ASG-EUPOS system. They oscillated within 2 cm horizontally and 4 cm vertically. In case of 15-minute sessions (with one second survey interval) processed in the POZGEO service the differences oscillated within the limits of 20 centimeters horizontally and vertically. The RTK technique can guarantee accuracies of 1–3 cm horizontally in open area, but for control points independent RTK surveys are required to provide reliability.

References

- BAKUŁA M., OSZCZAK S., BARYŁA R., POPIELARCZYK D., JARMOŁOWKI W., TYSZKO A., OSZCZAK B., SITNIK E., GREGORCZYK R., WIELGOSZ P., RAPIŃSKI J., JESIOTR G. 2007. *Determination of Coordinates of Control Points in the Wieruszów District Area*, Geomatics and Environmental Engineering, AGH University of Science and Technology, 1(1/1): 43–52.
- BAKUŁA M., OSZCZAK S., BORNUS R., JARMOŁOWSKI W., PELC-MIECZKOWSKA R., GREGORCZYK R. 2008. *Zastosowanie technologii GPS do wyznaczenia współrzędnych osnowy realizacyjnej obwodnicy miasta Wyszkowa*. Acta Sci. Pol. Geod. Descr. Terr., 7(4): 27–36.
- BAKUŁA M., OSZCZAK S., PELC-MIECZKOWSKA R. 2009. *Performance of RTK Positioning in Forest Conditions: Case Study*. Journal of Surveying Engineering, American Society of Civil Engineers, 135(3): 125–130.
- BOSY J., GRASZKA W., LEONCZYK M. 2007. *ASG-EUPOS. A Multifunctional Precise Satellite Positioning System in Poland*. European Journal of Navigation, 5(4): 2–6.
- HOFMANN-WELLENHOF B., LICHTENEGGER H., COLLINS J. 1997. *Global Positioning System: Theory and Practice*. 4th ed. Springer, Berlin Heidelberg New York.
- MISRA P., ENGE P. 2006. *Global Positioning System: Signals Measurement and Performance*. Ganga-Jamuna Press, Massachusetts.

THE USE OF RTCM 2.X DEKODER SOFTWARE FOR ANALYSES OF KODGIS AND NAWGIS SERVICES OF THE ASG-EUPOS SYSTEM

Rafał Kaźmierczak, Grzegorz Grunwald, Mieczysław Bakuła

Chair of Satellite Geodesy and Navigation
University of Warmia and Mazury in Olsztyn

Key words: Geodesy and Cartography, GNSS, RTCM, KODGIS, NAWGIS.

Abstract

The paper presents preliminary results of KODGIS and NAWGIS analyses with the use of RTCM 2.x Dekoder software. The software was created in the Chair of Satellite Geodesy and Navigation in Olsztyn. It allows analyzing values of pseudo-range corrections (PRC) being transmitted in the RTCM format by the ASG-EUPOS system. The analyses of PRC values over time for each satellite can allow to research the accuracy of differential positioning in KODGIS and NAWGIS services with the use of different GNSS receivers. The paper presents initial tests of the RTCM 2.x Dekoder software as well as some general information on the RTCM structure.

WYKORZYSTANIE AUTORSKIEGO PROGRAMU RTCM 2.X DEKODER DO BADAŃ SERWISÓW KODGIS I NAWGIS SYSTEMU ASG-EUPOS

Rafał Kaźmierczak, Grzegorz Grunwald, Mieczysław Bakuła

Katedra Geodezji Satelitarnej i Nawigacji
Uniwersytet Warmińsko-Mazurski w Olsztynie

Słowa kluczowe: geodezja i kartografia, GNSS, RTCM, KODGIS, NAWGIS.

Abstrakt

W pracy przedstawiono wstępne wyniki badań serwisów KODGIS i NAWGIS z wykorzystaniem autorskiego oprogramowania RTSM 2.x Dekoder. Program RTCM 2.x Dekoder opracowano w Katedrze Geodezji Satelitarnej i Nawigacji, UWM Olsztyn. Umożliwia on analizę wartości poprawek kodowych (PRC), transmitowanych w czasie rzeczywistym przez system ASG-EUPOS, w formacie RTCM. Analiza wartości przebiegu PRC dla poszczególnych satelitów umożliwia badanie wpływu dokładności wyznaczonych pozycji z wykorzystaniem różnych odbiorników GNSS oraz serwisów KODGIS i NAWGIS. W pracy przedstawiono wstępne testy wykorzystania programu RTCM 2.x Dekoder, jak również informacje dotyczące formatu RTCM.

Introduction

The data transmission protocols defines the terms of transmission of data from one place to another. The wrong choice of them can cause incorrect transmission or lack of it. The most of GNSS equipment producers develop their own data transmission protocols (usually in binary mode). Producers develop a couple of protocols for different hardware or applications. For instance, Trimble company's hardware is based on RT17, TSIP, CMR/CMR+ or combination of them. Another producers also have their own protocols: Leica (LB2), Ashtech (MBEN/PBEN, DBEN), AOA (ConanBinary, TurboBinary), Javad (JPS), Topcon (TPS), u-blox (MBX) and JPL(SOC). The structure of most of this protocols is binary but some of them, for example MBEN/PBEN (Ashtech) or LB2 (Leica) are formatted in ASCII standard (YAN 2006).

NTRIP (*Network Transport of RTCM via Internet Protocol*) is the standard built on client-server model, which transmits GNSS data from reference station to receiver. It is based on HTTP (*Hypertext Transfer Protocol*) and uses TCP protocol to transmission, in spite of that its architecture was originally built on internet radio system Icecast (its works with the aid of a couple of data sources connected to single server, from which information are transmit to many users) (WEBER 2004). NTRIP is capable of transmission data stream, which contains body of RTCM messages and data of every type (MCKESSOCK 2007). The protocols version 1.0 was accepted and was published as the RTCM standard in 2004. Work on its modernization is continued, which effect is version 2.0 of the protocol (WEBER 2004).

The full NTRIP system consists of: NTRIP caster, NTRIP server and sources and clients of NTRIP. Figure 1 shows the scheme of NTRIP protocol (MCKESSOCK 2007).

The NTRIP sources generates streams of binary data and transmit it to a client. This sources can be based on every type data, but originally the DGNSS corrections was transmitted in RTCM format.

RTCM is the most popular standard that transmit corrections. The standard was developed by Radio Technical Commission For Marine Services. It is used in most of GNSS applications that work in real time (<http://www.rtcn.org> 10.01.2009). The program RTCM Dekoder, which can be used to analyze RTCM data, is based on the RTCM standard.

RTCM Standard

In 1983 the Radio Technical Commission for Maritime Services (RTCM) appointed the Special Committee 104 (SC-104), which established the

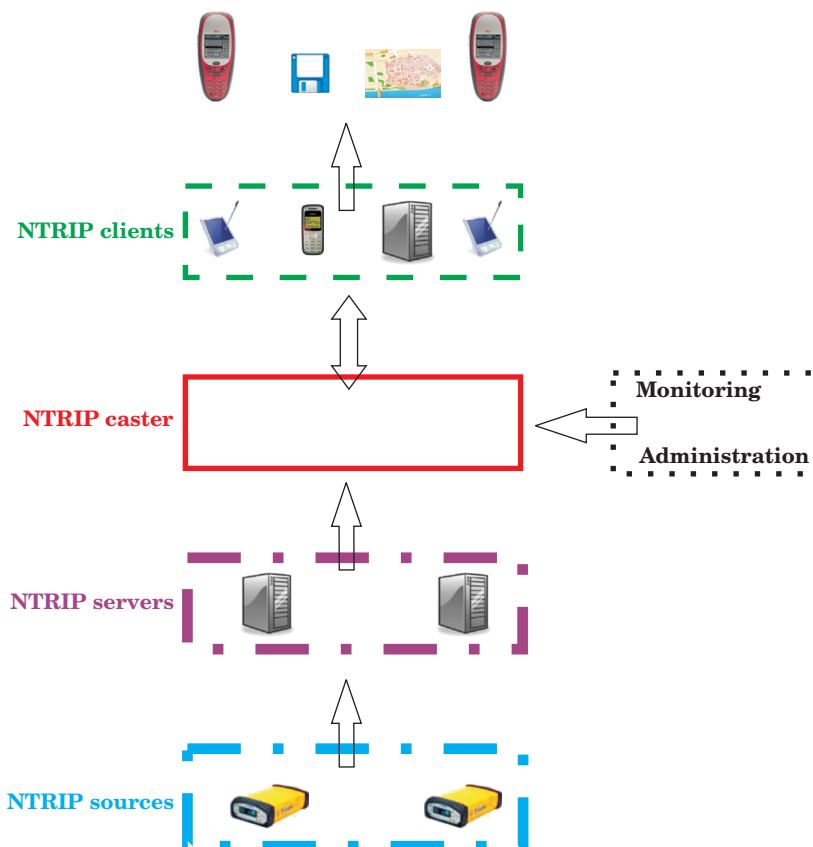


Fig. 1. The components of NTRIP protocol

Table 1

Development of RTCM

RTCM version	The year of application	Changes applied
RTCM 1.0	1985	Temporary recommendation for DGPS (PRC and RRC)
RTCM 2.0	1990	DGPS corrections and additional information Messages 1-17, 59
RTCM 2.1	1994	Extension for RTK Messages 18/19 and 20/21
RTCM 2.2	1998	Extension for DGLONASS Messages 31-37
RTCM 2.3	2001	Additional information for RTK Messages 23,24
RTCM 3.0	2004	New solution for RTK
RTCM 3.1	2008	Solution for transformation

Table 2

Types of RTCM messages

Number of message	Status	Message type	
1	specified	GPS differential corrections	
2	specified	GPS delta-differential corrections	
3	specified	Position of reference station	
4	proposed	Reference station datum	
5	specified	GPS constellation health	
6	specified	GPS null frame	
7	specified	DGPS radiobeacon almanac	
8	proposed	Pseudolite almanac	
9	specified	GPS partial correction set	
10	warranted	P-code differential corrections	
11	warranted	C/A-code L1, L2 delta corrections	
12	warranted	Pseudolite (pseudo-satellite) station parameters	
13	proposed	Ground transmitter parameters	
14	specified	GPS time of week	
15	specified	Ionospheric delay message	
16	specified	GPS special message	
17	proposed	GPS ephemerides	
18	specified	RTK uncorrected carrier phases	Messages 18-21 added in RTCM 2.1
19	specified	RTK uncorrected pseudoranges	
20	specified	RTK carrier phase corrections	
21	specified	RTK/high-accuracy pseudorange corrections	
22	proposed	Extended reference station parameters	
23	proposed	Type of antenna	Messages 23-24 added in RTCM 2.3
24	proposed	Reference station: (ARP - Antenna Reference Point)	
25-26	not defined		
27	proposed	Extended almanac of DGPS	
28-30	not defined		
31	proposed	GLONASS differential corrections	Messages 31-36 added in RTCM 2.3
32	proposed	Differential GLONASS reference station parameters	
33	proposed	GLONASS constellation health	
34	proposed	DGLONASS corrections	
35	proposed	GLONASS radiobeacon almanac	
36	proposed	GLONASS special message	
37	proposed	GNSS system time offset	
38-58	not defined		
59	specified	Proprietary message used in VRS 2.3 and FKP2.3	
60-63	reserved	Multipurpose usage	

structure and the format of transmitting the data within the DGPS system (SPECHT 2007). It established definitions of the elements and data units, the minimum time interval between transmissions, data segment size, their protocols and range. RTCM Standard is the most widely used model for the transmission differential GPS.

RTCM message consists of two main parts: a header and the rest remaining words of the message. The header consists of two words. The second part contains up to 31 words (usually it does not extend the length of 12 words) (WILLGALIS 2005). The scheme of the structure of RTCM message is presented in the Figure 2.

HEADER		THE REST OF WORDS			
WORD 1	WORD 2	WORD 3	WORD 4	...	WORD 33

Fig. 2. The structure of RTCM message

The header

The header is constructed by the two first words in each message. They are identical for every type of message. The main function of the header is to maintain the timing of receipt the corrections by means of a *modified counter Z*.

1	2	3	4	5	6	7	8	9	10	11	12	13	14	15	16	17	18	19	20	21	22	23	24	25	26	27	28	29	30	WORD 1
PREAMBLE								IDENTIFIER OF NAVIGATION MESSAGE				IDENTIFICATION NUMBER OF THE BASE STATION								PARITY CONTROL										
1	2	3	4	5	6	7	8	9	10	11	12	13	14	15	16	17	18	19	20	21	22	23	24	25	26	27	28	29	30	WORD 2
MODIFIED Z COUNTER													LENTH OF MESSAGE		NUMBER OF SEQUENCES				STATE OF WORKING		PARITY CONTROL									

Fig. 3. The header of RTCM 2.x message

Message 1

The first message is the main type of a message. It concerns the measurements based on C/A code. It contains the corrections to pseudorange and the rate of their changes. There is an Issue of Data (IOD – the age of data) parameter connected with every correction. Mobile receiver uses the same parameters, which are used by the reference station. In this method the need to apply the same ionospheric and tropospheric model for the reference station and the mobile receiver is eliminated.

Table 3

The elements of RTCM 2.x message header

COLOUR	NAME	NUMBER OF BITS	MEANING
	PREAMBLE	8	Identical for all types of messages (01100110)
	IDENTIFIER OF NAVIGATION MESSAGE TYPES	6	Identifies the message type 0-63
	IDENTIFICATION NUMBER OF THE BASE STATION	10	Identification number of the DGPS base station; band 0-1023
	MODIFIED Z COUNTER	13	Represents reference time for differential data transmission
	NUMBER OF SEQUENCES	3	Number of sequences
	THE LENGTH OF THE MESSAGE	5	The number of words in messages; 0-31
	STATE OF WORKING	3	State of reference station; 8 states: 0 = scale factor UDRE = 1 1 = scale factor UDRE = 0.75 2 = scale factor UDRE = 0.5 3 = scale factor UDRE = 0.3 4 = scale factor UDRE = 0.2 5 = scale factor UDRE = 0.1 6 = transmission is not monitoring 7 = incorrect working of reference station
	PARITY CONTROL	N*6	N – number of words in the message
	NONSIGNIFICAT BITS	N*10	N – number of words in the message

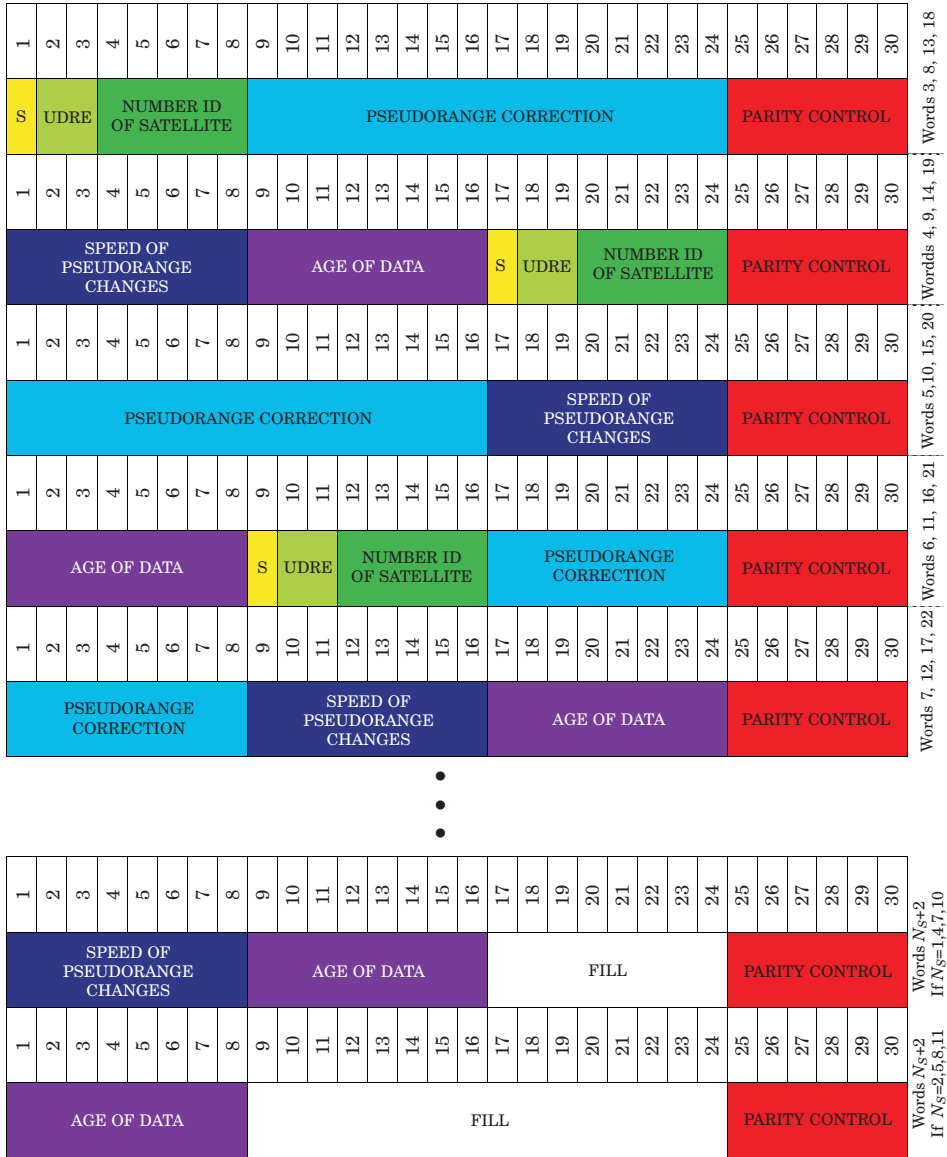


Fig. 4. Structure of RTCM 2.x. Message 1

Table 4

Content of 1 message

COLOUR	NAME	NUMBER OF BITS	MEANING		
Yellow	S	1	Scale factor – precision of measurement	Scale factor for PRC	Scale factor for RRC
			Value - 0 – for corrections of low precision pseudorange corrections	0.02 m	0.002 m/s
			Value - 1 – for corrections of higher precision pseudorange corrections	0.32 m	0.032 m/s
Light Green	UDRE	2	User Differential Range Error – estimated root-mean-square of pseudorange measurement; 4 states; $UDRE = \sqrt{\delta_r^2 + \delta_g^2}$ δ_r^2 – root-mean-square of base station pseudorange measurement δ_g^2 – root-mean-square of base station antenna position calculation 0 => UDRE ≤ 1 meter 1 => 1 meter < UDRE ≤ 4 meters 2 => 4 meters < UDRE ≤ 8 meters 3 => UDRE > 8 meters		
Green	Id NUMBER OF SATELLITE	5	Number of satellite; 1-32 (Value 0 means satellite number 32)		
Light Blue	PSEUDORANGE CORRECTION	16	Value of pseudorange (with „+” or „-”); when value 100 000 comes the satellite shouldn't be used; range +/- 655,34 m (for 0,02 m scale factor) or +/- 10485,44 m (for 0,32 m scale factor)		
Dark Blue	RANGE RATE CORRECTION	8	Value of range rate correction (with „+” or „-”); range +/- 0,254 m/s (for 0,002 m/s scale factor) or +/- 4,064 m/s (for 0,032 m/s scale factor)		
Purple	AGE OF DATA	8	When reference station data are older than data that are used, then the data shouldn't be used		
White	FILLING	$8 \times [Ns \text{ mod } 3]$	N_s – number of satellites		
Red	PARITY CONTROL	$N*6$	N – number of words in the message		
Light Grey	NONSIGNIFICANT BITS	$N*10$	N – number of words in the message		

Message 2

The second message contains the delta differential corrections. It was mentioned in the first message that when the method, which involves sending the corrections to pseudorange, is used, the mobile receiver and the reference station must be based on the same IOD parameters. If the receiver does not decode new ephemerides of the satellites as soon as they are received, it means that the time data and ephemerides of satellites which are used, are older than the data used by the reference station. The delta differential corrections enable the pseudorange correction (PRC) and range-rate correction (RRC). There are PRC and RRC determined at the reference station on the basis of old and new IOD. That's why:

$$\text{DELTA PRC} = \text{PRC (OLD)} - \text{PRC (NEW)} \quad (1)$$

$$\text{DELTA RRC} = \text{RRC (OLD)} - \text{RRC (NEW)} \quad (2)$$

The second message is transmitted together with the first message. Finally, the pseudorange correction is calculated from the formula:

$$\begin{aligned} \text{PRC}(t) = & \text{PRC}(N_{d1}) + \text{DELTA PRC}(S_{d2}) + \text{RRC}(N_{d1}) \cdot (t-t_1) + \\ & + \text{DELTA RRC}(S_{d2}) \cdot (t-t_2) \end{aligned} \quad (3)$$

- S_{d2} – parameter regarding old data – RTCM message 2,
- N_{d1} – parameter regarding old data – RTCM message 1,
- t – time of PRC calculation,
- t_1 – „modified Z counter” from message 1,
- t_2 – „modified Z counter” from message 2 (SPECHT 2007).

Message 3

The third message contains the information about ECEF (Earth-Centred Earth-Fixed) geocentric coordinates of the antennas of the reference receiver of DGPS station. Coordinates are given in the system WGS-84 (BETKE 2001).

Message 9

There are two methods of formatting pseudorange corrections. The first one uses the first message, whereas the second one uses the ninth message. In contrast to the first message, which includes PRC and RRC for all the satellites

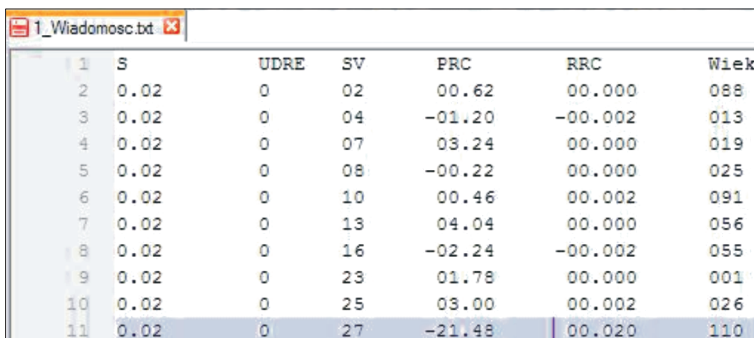
available for each reference station, the ninth message includes the corrections only to a few satellites (three satellites or one satellite). In the event of a damage to a single bit in the first message, the mobile receiver loses the corrections to all satellites. Compressing information for three each, results in decreasing the age of corrections. It also enables to use the remaining PRC corrections by the receiver (SPECHT 2007). The diagram of binary numeral system of the ninth message and the interpretation of its content are presented in the 4th illustration. The meaning and the range of data are identical as in the case of the first message (Tab. 5).

The RTCM 2.x Dekoder Program

To execute the program mentioned above, the Microsoft Visual Studio 2008 environment was used. Software source code was written in C#. It is an object-oriented language and it is based on the safe data types. The advantage of the selected language is the fact that there is no need to define the interface component by means of *Interface Definition Language* (IDL). There is also no point in creating the types of library to use them (WRIGHT 2002).

RTCM 2.x *Decoder* decodes and analyses initially the data included in the main messages RTCM 2.x. There are following basic tasks, which can be achieved by using the created application (RTCM 2.x *Decoder*):

- Decoding the RTCM data from a binary file (1st, 2nd, 3rd, 9th, 18th, 19th, 20th, 21th messages).
- Decoded data recording (in TXT format) divided by message types (e.g. '1_Message.txt' – 5th illustration).
- Visualization of the contents on the screen sent by the provider of message system,



	S	UDRE	SV	PRC	RRC	Wiek
1	0.02	0	02	00.62	00.000	088
2	0.02	0	04	-01.20	-00.002	013
3	0.02	0	07	03.24	00.000	019
4	0.02	0	08	-00.22	00.000	025
5	0.02	0	10	00.46	00.002	091
6	0.02	0	13	04.04	00.000	056
7	0.02	0	16	-02.24	-00.002	055
8	0.02	0	23	01.78	00.000	001
9	0.02	0	25	03.00	00.002	026
10	0.02	0	27	-21.48	00.020	110
11	0.02	0				

Fig. 5. The effect of decoding 1 message from file

S	UDRE	SV	PRC	RRC	Wiek danych
0.02	0	2	0.62	0	88
0.02	0	4	-1.2	-0.002	13
0.02	0	7	3.24	0	19
0.02	0	8	-0.22	0	25
0.02	0	10	0.48	0.002	91
0.02	0	13	4.04	0	58
0.02	0	16	-2.24	-0.002	55
0.02	0	23	1.78	0	1
0.02	0	25	3	0.002	26
0.02	0	27	-21.46	0.02	110
0.02	0	2	0.62	0	88
0.02	0	4	-1.2	0	13
0.02	0	7	3.24	0	19
0.02	0	8	-0.22	0	25
0.02	0	10	0.48	0.002	91
0.02	0	13	4.04	0	58
0.02	0	16	-2.24	-0.002	55

1 Message

S	UDRE	SV	PRC	RRC	Wiek danych
0.02	0	2	-4.86	0	86
0.02	0	4	-4.74	0	6
0.02	0	7	-4.62	0	18
0.02	0	13	-4.76	0	30
0.02	0	16	-4.9	0	54
0.02	0	23	-4.78	0	104
0.02	0	25	-4.9	0	25
0.02	0	2	-4.88	0	86
0.02	0	4	-4.78	0	6
0.02	0	7	-4.66	0	16
0.02	0	13	-4.8	0	30
0.02	0	16	-4.82	0	54
0.02	0	23	-4.78	0	104
0.02	0	25	-4.94	0	25

2 Message

ECFEX	ECFXY	ECFZ	D stacji	Z	Stan pracy stacji
3840289.01	1381860.63	4885326.36	890	2700.6	0
3840289.01	1381860.63	4885326.36	890	2700.6	0
3840289.01	1381860.63	4885326.36	890	2712.6	0
3840289.01	1381860.63	4885326.36	890	2718.6	0
3840289.01	1381860.63	4885326.36	890	2724.6	0
3840289.01	1381860.63	4885326.36	890	2730.6	0
3840289.01	1381860.63	4885326.36	890	2736.6	0
3840289.01	1381860.63	4885326.36	890	2742.6	0
3840289.01	1381860.63	4885326.36	890	2748.6	0
3840289.01	1381860.63	4885326.36	890	2754.6	0
3840289.01	1381860.63	4885326.36	890	2760.6	0
3840289.01	1381860.63	4885326.36	890	2766.6	0
3840289.01	1381860.63	4885326.36	890	2772.6	0
3840289.01	1381860.63	4885326.36	890	2778.6	0
3840289.01	1381860.63	4885326.36	890	2784.6	0
3840289.01	1381860.63	4885326.36	890	2790.6	0
3840289.01	1381860.63	4885326.36	890	2796.6	0

3 Message

S	UDRE	SV	PRC	RRC	Wiek danych
0.02	0	14	-0.28	0.002	52
0.02	0	12	2.22	0.002	59
0.02	0	4	-0.92	0	49
0.02	0	2	-3.26	0	33
0.02	0	0	-18.04	0.002	35
0.02	0	30	1.88	0	118
0.02	0	17	-0.38	0	72
0.02	0	9	1.74	0.002	16
0.02	0	27	4	-0.002	6
0.02	0	0	-18.06	0	35
0.02	0	17	-5.4	0	72
0.02	0	9	1.72	0	16
0.02	0	17	-6.42	-0.008	72
0.02	0	9	1.74	0.004	16
0.02	0	30	1.88	0	118
0.02	0	2	-3.24	0.002	33
0.02	0	0	-18.06	0.006	35

4 Message

Fig. 6. Examples of decoded in RTCM 2.x Dekoder messages

There are following additional functions of RTCM 2.x:

- Displaying the message types transmitted in ASG-EUPOS system,

9. Wiadomość	18. Wiadomość	19. Wiadomość	20. Wiadomość	21. Wiadomość	Typy transmitowanych wiadomości
3,	59(SubID: 2),	59(SubID: 2),	2,	9, 16, 9, 9, 9, 9, 9, 9, 9, 9, 59(SubID: 2),	59(SubID: 2), 3, 9, 9, 9, 9, 9, 9, 3, 9, 9, 9, 9, 59(SubID: 2), 59(SubID: 2), 3, 9, 9, 9, 9, 9, 9, 9, 9, 9, 59(SubID: 2), 59(SubID: 2), 3, 9, 9, 9, 9, 9, 9, 9, 9, 9, 59(SubID: 2), 59(SubID: 2), 3, 9, 9, 9, 9, 9, 16, 2, 9, 3, 9, 9, 9, 9, 59(SubID: 2), 59(SubID: 2), 9, 9,

Fig. 7. The KODGIS RTCM message types

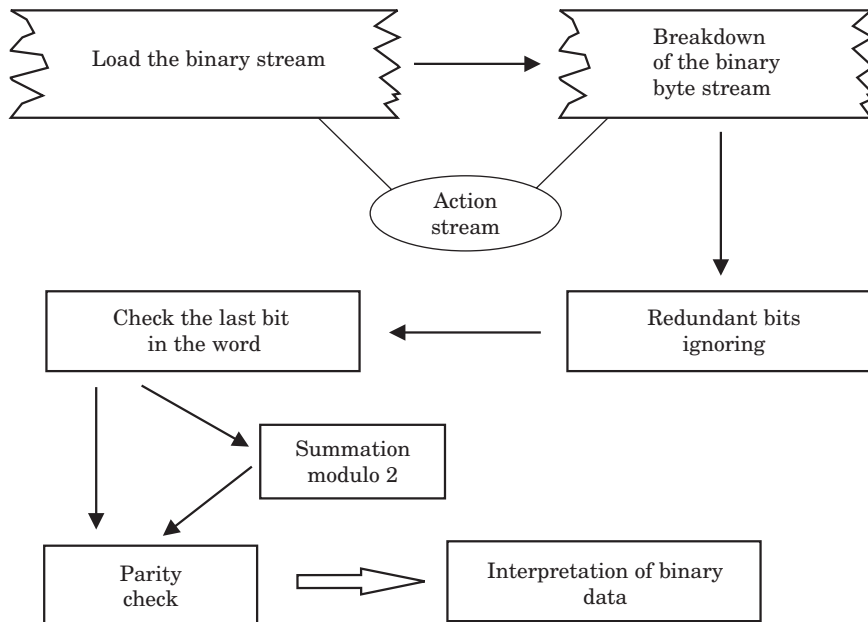


Fig. 8. Decoding process

– Presentation in the charts the dependence between the change of the value of the correction to pseudorange and the time for particular satellites (zooming in and zooming out the displayed data in the chart, highlighting the value, the possibility to save the charts as: Jpeg, GIF, PNG, Emf, Tiff, Bmp, direct print).

– Comparison the values of corrections to pseudorange from 1st message (NAWGIS) and 9th message (KODGIS) in the chart for any satellites,

Optional addition to particular data, for each satellites, information from the header (ID of the station, a counter Z, the status of work of the station).

The process of decoding the binary stream transmitted in KODGIS and NAWGIS is presented in the 8th illustration.

The comparative analysis of KODGIS and NAWGIS services were performed in two stages:

1. General summary of the types of transmitted messages in services.
2. Comparison of the transmitted PRC corrections for the north part of Poland in the charts.

Table 5

Message types KODGIS and NAWGIS

Service	Pseudorange corrections	Coordinates of base station	Text message	Private message	Additional information about reference station
KODGIS	2, 9	3	16	59	–
NAWGIS	1, 2	3	16	59	22, 23, 24

As a result of decoding RTCM messages, transmitted in NAWGIS PÓŁNOC and POŁUDNIE, the coordinates of referential station for the service were set. An example of comparison the PRC corrections for NAWGIS PÓŁNOC and POŁUDNIE are presented in the following illustration.

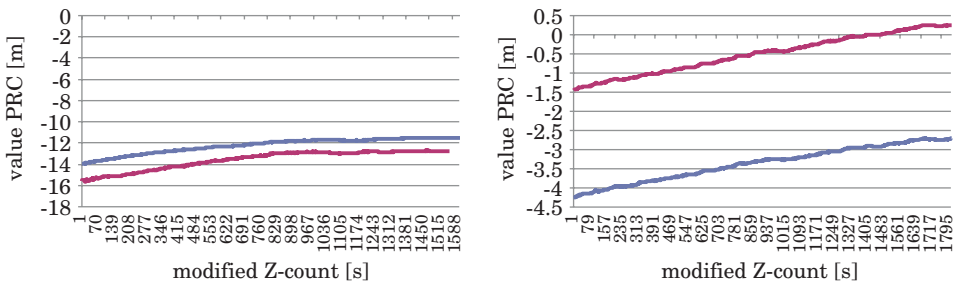


Fig. 9. Comparison of PRC values for NAWGIS PÓŁNOC (blue) and POŁUDNIE (red) for 9 and 11 satellites

The following illustrations present the summary of corrections for NAWGIS PÓŁNOC and KODGIS. The PRC values are generated by ASG-EUPOS system for Olsztyn. The chart of the corrections in RTCM Decoder 2.x transmitted in the services: KODGIS and NAWGIS PÓŁNOC.

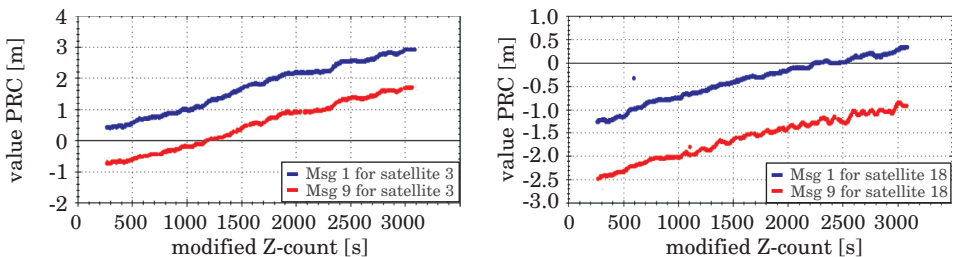


Fig. 10. PRC values for NAWGIS (blue) and KODGIS (red) for 3 and 18 satellites

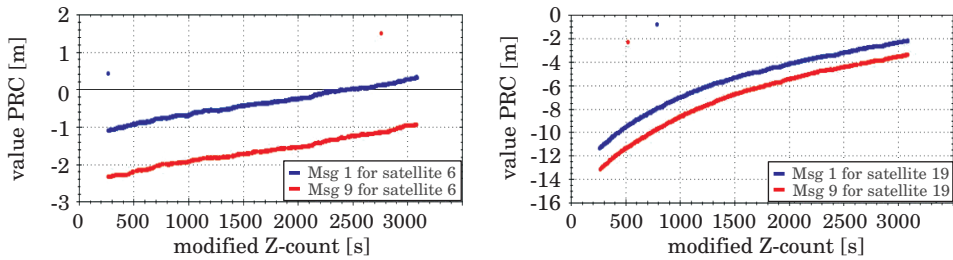


Fig. 11. PRC values for NAWGIS (blue) and KODGIS (red) for 6 and 7 satellites

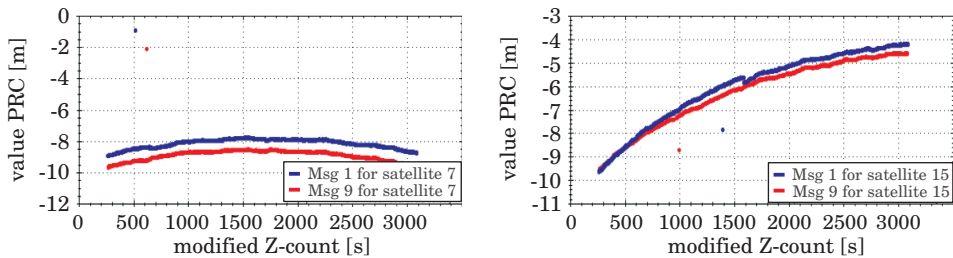


Fig. 12. PRC values for NAWGIS (blue) and KODGIS (red) for 15 and 19 satellites

Conclusion

The developed RTCM 2.x Decoder programme enables to visualize and to record the corrections to pseudorange with differential DGPS positioning. It is possible due to decoding the RTCM 2.x format. There are three main stages which can be distinguished during the process of decoding the data. The first of them is to load the binary stream and to omit the redundant bits. The second stage is to check the last bit in a byte and the parity checking. The last element of decoding the RTCM data is the interpretation of binary values. Using the programme enables to observe the changes of corrections to pseudorange. Differences in the pseudorange corrections, which are presented in the charts in this article, mean that in order to achieve for both DGPS services ASG-EUPOS accuracy, it is necessary to use GNSS receivers, which are respectively dedicated with DGPS ASG-EUPOS services. Differences in pseudorange corrections to NAWGIS PÓŁNOC and PÓŁUDNIE are between 2 and 4 meters during the test period. These values depend on the position of the particular satellite. The summary of NAWGIS PÓŁNOC and KODGIS values (for Olsztyn) presents also the differences in corrections to particular satellites. If

the types of the messages in KODGIS and NAWGIS are taken into account, it can be noticed that the differences in pseudorange corrections are one of the main reasons of achieving accuracy in tested services.

Translated by AUTORS

Accepted for print 13.05.2011

References

- BETKE K. 2001. *Transmission characteristics of marine Differential GPS (DGPS) stations*, 9.
- MCKESSOCK G. 2007. *A comparison of local and wide area GNSS differential corrections disseminated using the Network Transport of RTCM via Internet Protocol (NTRIP)*. Department of Geodesy and Geomatics Engineering Technical report No. 249, University of New Brunswick, Canada, pp. 23–27.
- RTCM Recommended Standards for Differential GNSS (Global Navigation Satellite Systems) Service, version 2.3* RTCM Special Committee NO.104, Radio Technical Commission for Maritime Services (RTCM Paper 88-96/SC104).
- RTCM, <http://www.rtcn.org> (January 2009).
- SPECHT C. 2007. *System GPS*. Bernardinum, Pelplin, pp. 256–257, 261–262, 266–267.
- WEBER 2004. *Streaming Real-Time IGS Data and Products Using NTRIP*. Federal Agency for Cartography and Geodesy (BKG). Frankfurt, Germany, pp. 1–2.
- WILLGALIS S. 2005. *Beiträge zur präzisen Echtzeitpositionierung in GPS-Referenzstationsnetzen*. Wissenschaftliche arbeiten der Fachrichtung Geodäsie und Geoinformatik der Unniversität Hannover, Germany, 255: 44–46
- WRIGHT CH. 2002. *C# Porady i metody*. Nakom, Poznań.
- YAN T.S. 2006. *GNSS Data Protocols: Choice and Implementation*. International Global Navigation Satellite Systems Society IGNS Symposium. Holiday Inn Surfers Paradise, 26: 3.

**NEW ELABORATION OF GRADIENT MAP
OF VERTICAL CRUSTAL MOVEMENTS
IN THE TERRITORY OF POLAND**

Kamil Kowalczyk¹, Jacek Rapiński²

¹ Chair of Land Surveying and Geomatics

² Institute of Geodesy

University Warmia and Mazury in Olsztyn

Key words: vertical crustal movements, gradient map, precise leveling.

A b s t r a c t

The goal of this elaboration was to elaborate the map of vertical crustal movements gradients in the territory of Poland. This paper describes general characteristic of leveling data from last two leveling campaigns as well as the method of evaluation. Earlier gradient map from 1990 is also discussed. The map of gradients with an accuracy estimate is a result of this work.

**NOWE OPRACOWANIA MAPY GRADIENTÓW PRĘDKOŚCI PIONOWYCH RUCHÓW
POWIERZCHNI SKORUPY ZIEMSKIEJ NA OBSZARZE POLSKI**

Kamil Kowalczyk¹, Jacek Rapiński²

¹ Katedra Geodezji Szczegółowej

² Instytut Geodezji

Uniwersytet Warmińsko-Mazurski w Olsztynie

Słowa kluczowe: ruchy pionowe skorupy ziemskiej, mapy gradientów, niwelacja precyzyjna.

A b s t r a k t

Celem pracy było opracowanie map gradientów prędkości pionowych ruchów powierzchni skorupy ziemskiej na obszarze Polski. W artykule przedstawiono ogólną charakterystykę materiału niwelacyjnego z ostatnich dwóch kampanii niwelacji precyzyjnej oraz sposób opracowania map gradientów. Odniesiono się także do wcześniej opracowanej mapy gradientów z roku 1990. Efektem jest mapa gradientów wraz z oceną błędów średnich ich wyznaczenia.

Introduction

First attempts to determine the vertical crustal movements in Poland were taken in the late fifties. This works resulted in three maps of vertical crustal movements (WYRZYKOWSKI 1971, 1985a, KOWALCZYK 2006a). The first vertical crustal movements elaboration in Poland was made in 1960 on the basis of common leveling lines from 1952–1958 (I i II order) and 1926–1937 (I order) campaigns. These lines did not create leveling loops (NIEWIAROWSKI, WYRZYKOWSKI 1961). The method used to obtain the vertical crust movement was based on the comparison of two adjusted networks fixed at the same point for which the height was assumed to be zero (NIEWIAROWSKI, WYRZYKOWSKI 1961).

Second and third attempt to derive vertical crustal movements in Poland was based on much larger data set, with different methods for movement speed computation. The comparison of this methods can be found in (KOWALCZYK 2006b).

The above works was published as an analog maps and model (KOWALCZYK 2006b). Vertical crustal movements were depicted using isolines. The other possibility to depict the movements is a map of gradients calculated for each leveling line with respect to it's direction. Until now in Poland only one map of gradients was published (Fig. 1) (WYRZYKOWSKI 1990). In this paper as well as in (WYRZYKOWSKI 1990) the all of the gradients are positive since their direction is depicted by arrows on the maps.

Gradients of vertical crustal movements speed distinctly depicts those lines for which the value of movement is equal. These values are expressed as a slope of the straight line in the unit of time. In this work unadjusted data was used for the computations, so called "observed" data (KAKKURI 1987). The distances were calculated on the basis of coordinates in 1992 coordinate system.

The information about gradients of vertical crustal movements can be used in scientific and practical tasks such as (WYRZYKOWSKI 1990):

- seismic regional assignment,
- micro seismic regional assignment of cities and large industrial facilities,
- research on earth crust,
- prospecting of natural resources,
- localization of large buildings and structures,
- evaluation of correlates between modern earth crust movements and geophysical fields,
- evaluation of the state of the art of leveling networks.

In particular the gradients can be used in the research on the correlation between vertical crustal movements and geophysical fields. The main reason for this is because on the large areas the errors are deforming the movements speed more then gradients (WYRZYKOWSKI 1990).

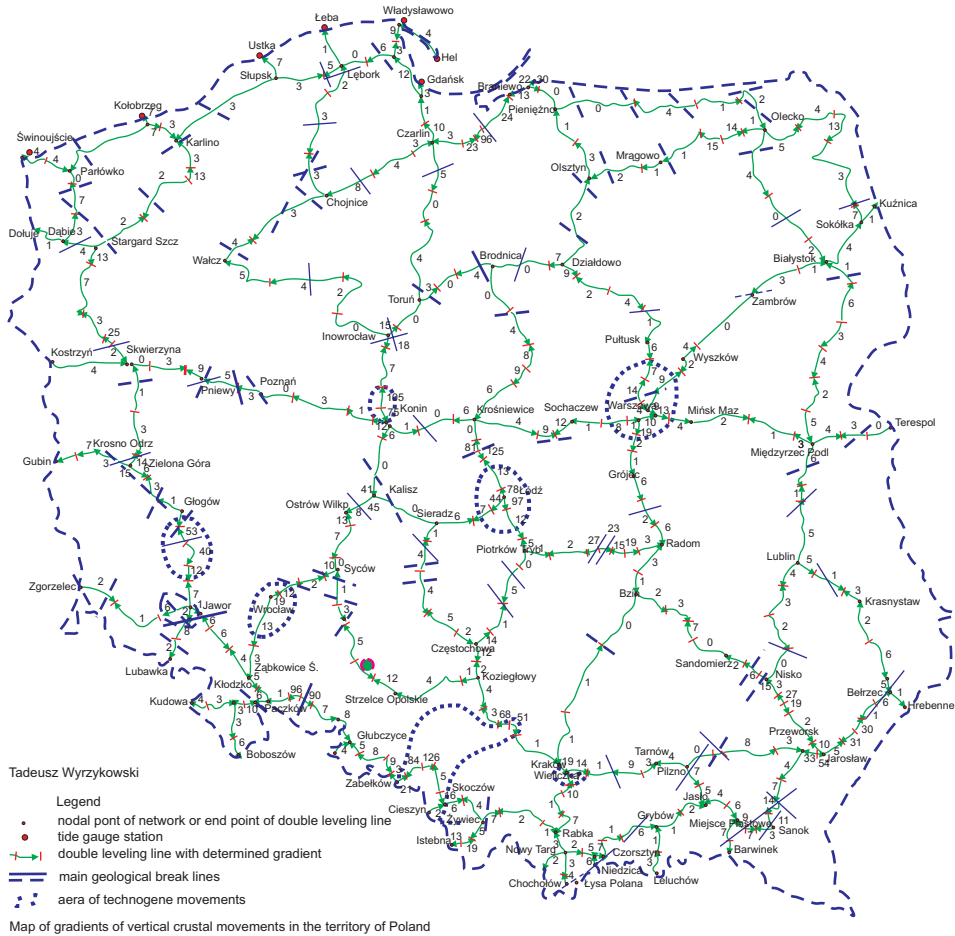


Fig. 1. Map of gradients of vertical crustal movements in the territory of Poland 1990

Leveling data used in elaboration

The first study of map of gradients of vertical crustal movements in Poland was performed on the basis of the double leveling of I order (1974–1979), which completely overlays with earlier I order leveling lines (1952–1955) and partially with 2 order 1 class lines (1955–1958). Total number of 141, 8411 km long lines, forming 23 closed polygons of double leveling were used. In these lines there were 5300 common benchmarks (WYRZYKOWSKI 1990). Average time between two consecutive epochs was 21 years. For the current study the unadjusted vertical crustal movements network was used as a source material (KOWALCZYK 2006a). This network was created on the basis of I order leveling

data from 1974–1982 and 1997–2003. In general more than 360 lines of double leveling were used. In this lines almost 11 thousand common benchmarks were identified. Mean time difference between epochs was 22.5 year. Detailed description of materials used can be found in (KOWALCZYK 2006b, 2009).

Gradient determination

In (WYRZYKOWSKI 1990) gradients were calculated using two formulas:
– first, as a angular value of slope in time unit (”/year – seconds per year)

$$\text{grad}V_1 = \frac{(V_2 - V_1) \cdot \rho''}{L} \text{ ”/year} \quad (1)$$

where:

V_1, V_2 – speed of vertical crustal movement in first and last point of leveling line, for which the gradient is calculated in mm/year,

L – distance between points in mm,

ρ'' – ro sec. 206 265

– second, as a difference of vertical crust movement speed, calculated for 1 km long line (mm/rok/km).

$$\text{grad}V_1 = \frac{(V_2 - V_1)}{L} \quad (2)$$

The dependency between these two equations can be denoted as (WYRZYKOWSKI 1990):

$$\text{grad}V_1 \approx 5\text{grad}V_1 \quad (3)$$

In this paper both equations (1 and 2) were used. The difference is that instead of speed differences in end points ΔV we have used unadjusted speed Δv on these lines.

Elaboration of new map of gradients of vertical crustal movements in the territory of Poland

The map of gradients of vertical crustal movements speed was prepared as a digital model and its cartographic representation. Both model and map was prepared in 1992 coordinate system (Fig. 2).

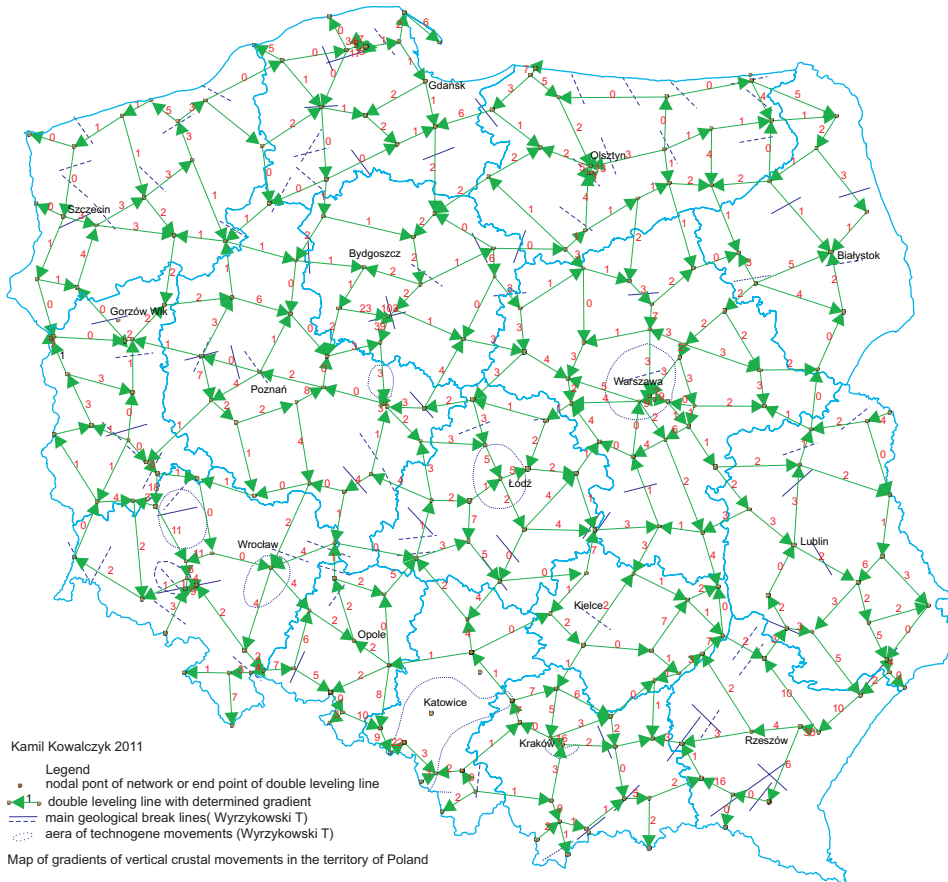


Fig. 2. Map of gradients of vertical crustal movements in the territory of Poland, year 2011

Additionally the map contains:

- the value of gradients in $0.001''/\text{year}$ (the choice of units was the same as in (WYRZYKOWSKI 1990), to allow comparison of both maps,
- the direction of unadjusted value of vertical crustal movement on the network lines,
- main lines of geological breaks from WYRZYKOWSKI 1990,
- major cities.

Analysis of gradient of vertical crustal movements distribution in the territory of Poland

To keep the ability to compare gradient map from 1990 and present map, the results were appraised statistically. Figure 3 presents the amount of determined gradients of vertical movements with resolution of 0.01"/year.

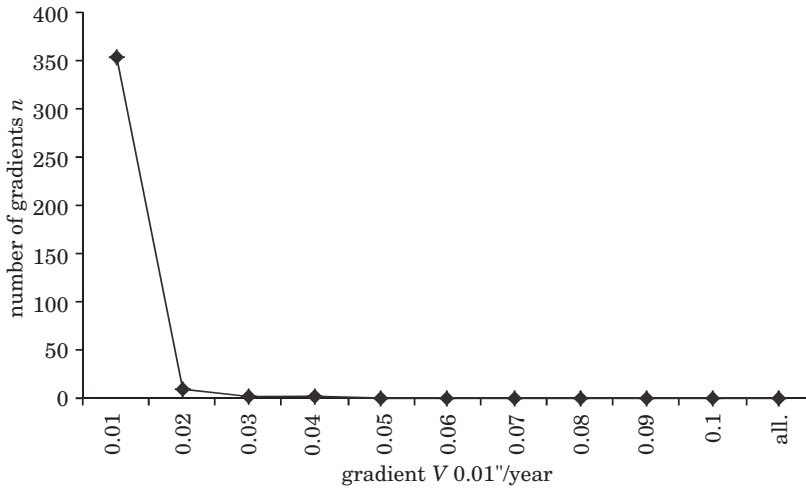


Fig. 3. The amount of determined gradients of vertical movements with resolution of 0.01"/year

From Figure 3 it is clear that 354, which is 96%, of overall vertical movement gradients are about 0.01"/year, in the range of 0.02"/year there is 98,5% of gradients.

For the further examination of the gradients distribution the more detailed figure within the range of 0.01"/year and resolution 0.001"/year is presented (Fig. 4).

In this case the distribution shows decreases of amount of gradients along with it's size.

The assessment of mean error of modern vertical crustal movements gradient in the territory of Poland was made with reference to mean length of leveling line, which is 37 km.

The formula for the mean error can be denoted as:

$$m_{\text{grad}v_{\text{sr}}} = \frac{\rho''}{L_{\text{sr}}} \sqrt{m_{\Delta v_{\text{sr}}}^2 + \frac{\Delta v_{\text{sr}}^2}{L_{\text{sr}}} m_L^2} \quad (4)$$

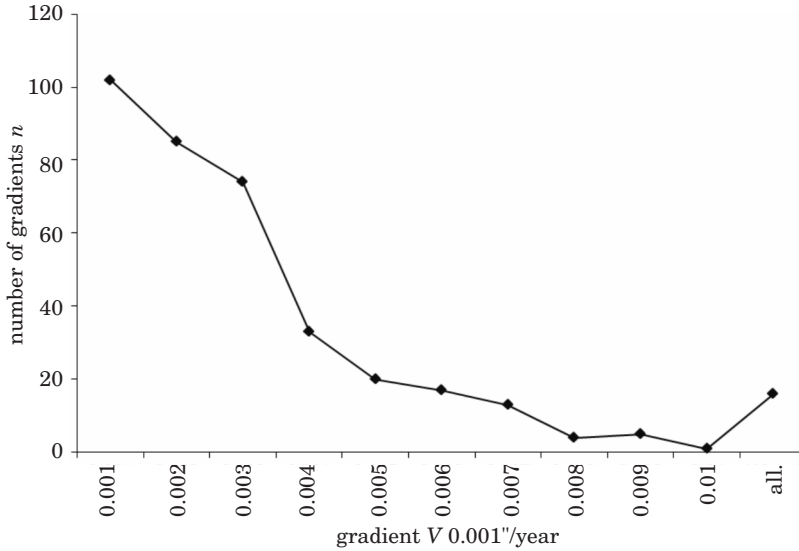


Fig. 4. The amount of determined gradients of vertical movements with resolution 0.001"/year

where:

$m_{\Delta v_{\dot{s}r}}$ – mean error of vertical crustal movements on network line

$\Delta v_{\dot{s}r} = 0.44$ mm/year

$m_L = 1\ 000\ 000$ mm

In equation (4) the mean error of vertical crustal movements on network line remains unknown. To calculate this error one must start with the formula:

$$\Delta v = \frac{\Delta h}{\Delta t} \tag{5}$$

where:

Δh – the difference of height differences on the line of double leveling ($h_2 - h_1$) in mm,

Δt – distance between epochs in years

The equation for the mean error of vertical crustal movement on network line can be written as:

$$m_{\Delta v_{\dot{s}r}} = \frac{1}{\Delta t_{\dot{s}r}} \sqrt{(m_{\Delta h_{\dot{s}r}}^2 + \Delta v_{\dot{s}r}^2 + m_{\Delta t_{\dot{s}r}}^2)} \tag{6}$$

where:

$m_{\Delta t}$ = 0.12 – mean error of epoch distance determination

$\Delta t_{\dot{s}r}$ – mean distance between epochs (22.5 year)

Mean $\Delta h_{\dot{s}r}$ error calculated using formula:

$$m_{\Delta h_{\dot{s}r}} = \sqrt{(m_{h_1}^2 + m_{h_2}^2) \cdot L_{\dot{s}r}} \quad (7)$$

The value of mean errors of the double line leveling $m_{h_1}^2$ i $m_{h_2}^2$ were obtained from WYRZYKOWSKIEGO (1985b) and GAJDEROWICZA (2005), and are equal to

$$m_{h_1}^2 = 0.55 \text{ mm/km}$$

and

$$m_{h_2}^2 = 0.52 \text{ mm/km}$$

Substituting the above values to equation (7) the value of mean error is $m_{\Delta h_{\dot{s}r}} = 4.60 \text{ mm}$.

Substitution to equation (6) will result in the final value of mean error $m_{\Delta v_{\dot{s}r}}$ of vertical crustal movement speed on the leveling line. In our case it was 0.21 mm/year. Substituting the above values to equation (4), the mean error of gradient of vertical crustal movement speed in the territory of Poland for the mean line length is $m_{\text{grad}v_{\dot{s}r}} = 0,0012''/\text{year}$.

To analyze the mean gradient, the ratio between each gradient and the entire network mean error is necessary. Simplified formula presented by (WYRZYKOWSKI 1990) was used to calculate mean error of each gradient:

$$m_{\text{grad}v} = \frac{\rho'' \cdot m_{\Delta h}}{\Delta T \cdot L} \quad (8)$$

The results were divided into 4 ranges (Tab. 1).

Table 1
Ratio between each gradients and the entire network mean error in percents

Ranges	Amount of occurrence	Value %
0-1	123	33.2
1-2	106	28.7
2-3	60	16.2
More	81	21.9

Looking at Table 1 it is clear that in 62% of cases the calculated ratio between each gradient and the entire network mean error is smaller then twic the value of the mean error. It means that the gradient is correct. The ratio is more then triple mean error happened in 22% of cases, which is a half of the

number obtained in (WYRZYKOWSKI 1990). Fifty percent of this cases happened on the technogene areas, remaining values only slightly exceeds the triple mean error.

Conclusions

In most cases the same methods that were used for the evaluation of vertical crustal movements map in the territorz of Poland (KOWALCZYK 2006a) were used to determine the gradients. However the change of the Baltic sea level is not taken into consideration in gradients determination. Therefor the gradients are free from the sea level errors. Each of the gradients of vertical movement speed is determined independently.

The largest gradient is observed on the Inowrocław – Szadłowice line – 0,103"/year with mean error 0,005"/year. Other large values of gradient were observed in the vicinity of Inowrocław, Jarosław and Łęczyce.

In the remaining area the value of gradients is smaller than 0,010"/year. The largest errors of gradients were on the short lines Kostrzyń 1 – Kostrzyń 2 (0,019"/year), Jaroty – Bartąg (0,016"/year), Godętowo – Łęczyce (0,016"/year), Konin 2 – Konin 1 (0,013"/year). Other large errors are also on the short lines.

The mean error of gradient of vertical crustal movement speed for the mean line length is $m_{grad_{sr}} = 0,0012"/year$. 78% of calculated gradients to mean error ratio is smaller than triple mean error. The results were 20% better than in previous elaboration. It can be caused by the use of more precise leveling equipment as well as the choice of data used for the calculations – only data from first class network was used. It is also confirmed by the mean errors of height determination mh for campaign #2 – 0,7 mm/km, # 3 – 0,55 mm/km, # 4 – 0,52 mm/km respectively. The mean value of gradient is $grad_v = 0.003"/year$.

With reach and systematic leveling data available (KOWALCZYK, BEDNARCZYK 2009) the elaboration of gradients for each line of double leveling can be performed. This kind of research would show for which of leveling network nodes the change in its heigt is significantly different from the avarege.

Translated by JACEK RAPIŃSKI

Accepted for print 10.10.2011

References

- GAJDEROWICZ I. 2005. *Ocena dokładności sieci niwelacji precyzyjnej I klasy pomierzonej w latach 1997–2003*. Technical Science, Supl. 2: 123–134.

- NIEWIAROWSKI J., WYRZYKOWSKI T. 1961. Wyznaczenie współczesnych ruchów pionowych skorupy ziemskiej na obszarze Polski przez porównanie wyników powtarzanych niwelacji precyzyjnych. Pr. Inst. Geod. i Kart., VII, 1(17).
- KAKKURI J. 1987. *Character of the Fennoscandian land uplift in the 20th century*. Geological Survey of Finland, Special Paper 2: 15–20, Helsinki.
- KOWALCZYK K. 2006a. Wyznaczenie modelu ruchów pionowych skorupy ziemskiej na obszarze Polski. Rozprawa doktorska UWM Olsztyn.
- KOWALCZYK K. 2006b. Porównanie współcześnie wyznaczonych ruchów pionowych powierzchni skorupy ziemskiej na obszarze Polski z wyznaczeniami wcześniejszymi. Przegląd Geodezyjny, 12: 4–7.
- KOWALCZYK K. 2009. Dane niwelacyjne w badaniu pionowych ruchów skorupy ziemskiej na obszarze Polski. Acta Sci. Pol. Geodesia et Descriptio Terrarum, 8(1): 31–44.
- KOWALCZYK K., BEDNARCZYK M. 2009. *Relational database of three precise leveling campaigns in Poland*. Techn. Sc., 12: 145–164.
- WYRZYKOWSKI T. 1971. *Mapa współczesnych bezwzględnych prędkości pionowych ruchów powierzchni skorupy ziemskiej na obszarze Polski*. Państw. Przeds. Wyd. Kartogr., Warszawa.
- WYRZYKOWSKI T. 1985a. *Mapa współczesnych prędkości pionowych ruchów powierzchni skorupy ziemskiej na obszarze Polski*. Inst. Geod. i Kart., Warszawa.
- WYRZYKOWSKI T. 1985b. *Analiza dokładnościowa materiału sieci I klasy (pomiar z lat 1974–1979)*. Pr. Inst. Geod. i Kart. t. XXXII, 1–2 (74–75).
- WYRZYKOWSKI T. 1990. *Opracowanie map gradientów prędkości współczesnych pionowych ruchów powierzchni skorupy ziemskiej na obszarze Polski*. Pr. Inst. Geod. i Kart., t. XXXVII, 1–2 (84–85).

VERIFICATION OF THEORETICAL PHONG MODEL IN REFLECTOR LESS SURVEYS

Kamil Kowalczyk¹, Jacek Rapiński²

¹ Chair of Land Surveying and Geomatics
² Institute of Geodesy
University Warmia and Mazury in Olsztyn

Key words: range finder, intensity, laser scanning.

Abstract

This paper presents the verification of Phong model used for reflector-less surveys. The model presented in (RAPINSKI, KOWALCZYK 2011) is compared with survey data. In order to obtain survey data the experiment with authors own testing device and software was performed. Data from the experiment was used to show the model parameters for various materials. The coefficients describing the model are: the fraction of light that was scattered, the fraction of light that was reflected and the luminance coefficient.

WERYFIKACJA TEORETYCZNEGO MODELU PHONGA W POMIARACH BEZLUSTROWYCH

Kamil Kowalczyk¹, Jacek Rapiński²

¹ Chair of Land Surveying and Geomatics
² Institute of Geodesy
University Warmia and Mazury in Olsztyn

Słowa kluczowe: dalmierz, parametr intensywności, skanowanie laserowe.

Abstrakt

W artykule przedstawiono weryfikację teoretycznego modelu Phong'a w pomiarach bezlustrowych. Model opisany przez RAPIŃSKIEGO i KOWALCZYKA (2011) zweryfikowano z wykorzystaniem danych pomiarowych. W celu pozyskania tych danych przeprowadzono eksperyment zaprojektowany przez autorów urządzeniem pomiarowym oraz autorskim oprogramowaniem. Na podstawie danych pomiarowych określono parametry modelu dla różnego typu materiałów. Parametry (współczynniki) opisujące model to część wysłanego światła lasera, która uległa rozproszeniu, część wysłanego światła lasera, która uległa odbiciu, oraz współczynnik opisujący luminancję.

Introduction

In modern civil engineering reflector-less surveys and laser scanning are continuously gaining attention. These techniques use laser beam to measure distance. There is a lot of effects that impact the distance measurement accuracy, maximum range and value of the intensity parameter. The fraction of laser light that returns to the range finder is conditional upon material type and color, incidence angle, laser wavelength and atmospheric attenuation (KOWALCZYK, RAPINSKI 2011).

In (RAPINSKI, KOWALCZYK 2011) authors described the proposition of use of theoretical Phong model for reflector less range finders maximum range. Although in theory this model seems to be appropriate it needs verification. The Phong model, used in computer 3D graphics, was adapted to model the maximum range of the range finder. This model describes the dependency of the incidence angle on the fraction of the returned laser light.

Practical verification of this model in real survey environment would be difficult due to large number of required observation, influence of not modeled effects (like atmospheric attenuation). In addition it is difficult to find an object with enough free space available for surveys (maximum range of modern equipment is in the range of few hundred meters). The verification was conducted in the laboratory environment.

The main goal of this paper is to verify the use of Phong model for maximum range and intensity parameter modeling.

Intensity and maximum range

Both intensity and maximum range are dependent on the fraction of power of laser beam that will return from the target. The laser range equation describes the dependency between transmitted and received laser beam power (SABATINI, RICHARDSON 2010):

$$P_R = \frac{\sigma D^4 \tau_{\text{atm}} \tau_{\text{sys}} P_T}{16 R^4 \lambda^2 K_a^2} \quad (1)$$

where:

P_R – received signal power;

P_T – transmitter power;

σ – effective target cross section (m²);

K_a – aperture illumination constant;

R – system range to target (m);

λ – wavelength (m);
 D – aperture diameter (m)
 τ_{atm} – atmospheric transmission factor;
 τ_{sys} – system transmission factor.

Assuming that the entire beam will be reflected, equation (1) becomes (KRUAPECH, WIDJAJA 2010):

$$P_R = \frac{\rho D^2 \tau_{\text{atm}} \tau_{\text{sys}} P_T}{8R^2} \quad (2)$$

where ρ stands for the target reflectance.

Deriving R from the equation 2 gives:

$$R = \sqrt{\frac{P_T \rho D^2 \tau_{\text{atm}} \tau_{\text{sys}}}{8P_R}} \quad (3)$$

In the equation 3, D^2 , τ_{sys} and the ratio P_R/P_T are constant for a certain instrument. The term τ_{atm} depends on the atmospheric extinction coefficient, and is constant for the atmospheric parameters during the survey. This parameter was neglected in further considerations since it was constant in laboratory environment.

Phong model

In theory, the laser beam reflection can be either specular reflection, diffuse reflection or retro reflection. In practice most reflections are a combination of specular and diffuse. Phong model divide the amount of light reflected in these two ways in two coefficients: k_d – the amount of beam that is diffused and k_s – the amount of beam that is reflected. The influence of the laser beam geometry is presented by Θ – incidence angle and Φ – the angle between incidence angle and the viewer direction. Additionally the luminance of the material is described by the parameter n . Thus the Phong model can be described by the following equation (GREGORY, LANDER 2009):

$$I = I_i(k_d \cos^\Theta + s_s \cos^n\Phi) \quad (4)$$

where:

I – the intensity of the reflected beam,
 I_i – the intensity of the incidence beam,
 k_d – the amount of beam that is diffused,

k_s – the amount of beam that is reflected,
 Θ – incidence angle,
 Φ – the angle between incidence angle and the viewer direction,
 n – parameter describing the luminance of the material.

It is important to notice that at the current stage, this model do not include the effects of atmospheric attenuation and material extinction. Figure 1 depicts the example shape of reflection modeled by Phong in polar coordinates. The angular coordinate depicts the incidence angle while the distance from the 0 point depicts the intensity value.

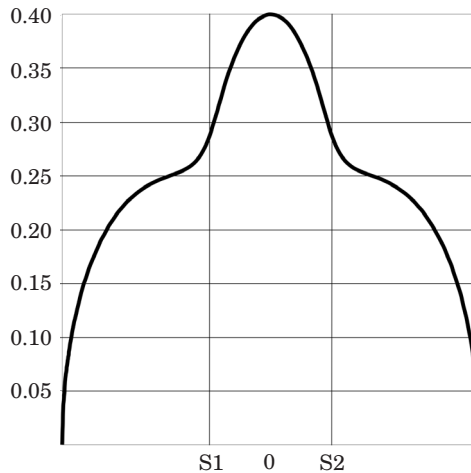


Fig. 1. Intensity plot

Experimental verification of phong model

As mentioned in the introduction, practical verification of this model in real survey environment would be difficult. Therefore verification of the Phong model was performed in the laboratory environment. The tasks connected with laboratory tests were focused in three main problems:

- testing device design,
- materials used for model verification,
- data recording.

Testing devices design was composed of:

- Atmega328 micro controller,
- laser light source,
- photo detector,

- servomotor with target holder,
- PC computer for data storage and visualization.

The main idea was to detect the change of voltage on the photo detector, which resistance changed according to the intensity of the laser light reflected from the test material. To change the incidence angle, the target holder had ability to rotate. The movement of servomotor, output voltage registration and data transfer to PC was made with Atmega328 micro controller. The appropriate micro controller software was coded by authors (application patent). The outline of the device is depicted in Figure 2.

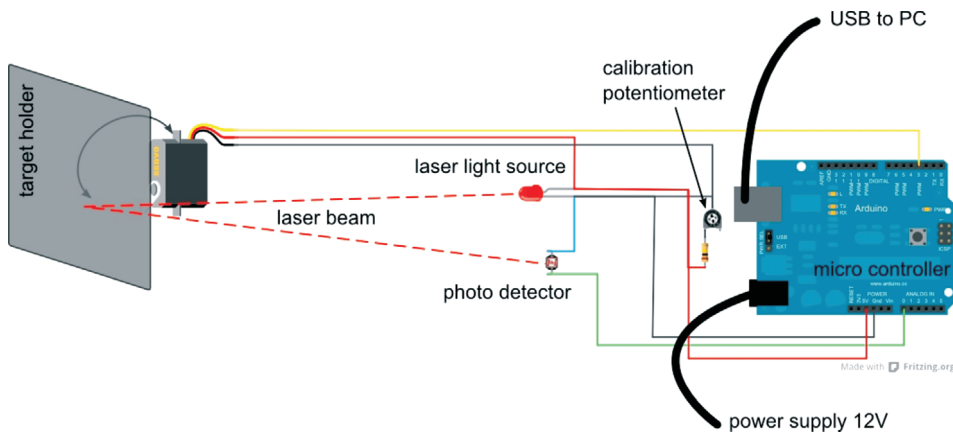


Fig. 2. Design of the testing device (the idea of authors)

The following materials were used for tests: white paper (matte and glossy), gray paper, red paper, blue foil, aluminum, tin foil, sand paper, shiny side of CD.

Results

To fit the parameters of each material to obtained data, a dedicated software in Processing language was developed. The software allowed to fit the data from the model to survey data by modifying three parameters: k_d – the amount of beam that is diffused and k_s – the amount of beam that is reflected and n – luminance. The example of fitting is presented in Figure 3.

In Figures 3a, b, c, d purple lines depicts the surveyed data and black outline is modeled data. The above figures confirms the possibility to use a Phong model for reflector less surveys. Figure 3a presents white, shiny paper. The “spike” at the incidence angle of about 0 degrees is visible. In Figure 3b white matte paper is shown. It confirms that matte materials

diffuses the light with no specular reflection. In the case of aluminum (Fig. 3c) there is a lot of specular reflection while almost none diffuse reflection. In Figure 3d, sand paper with gradation of 150 was used. The “outliers” are caused by single sand gains that reflected the laser beam.

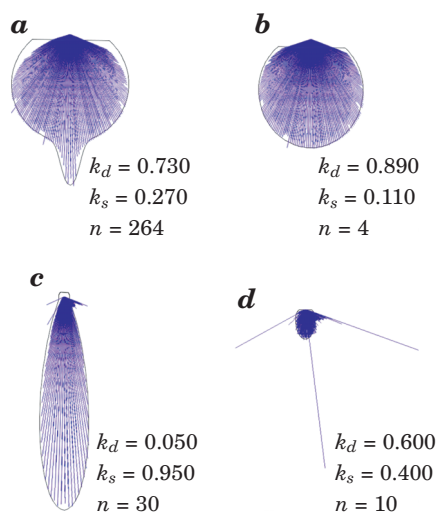


Fig. 3. Purple lines depicts the surveyed data and black outline is modeled data: *a* – white, shiny paper, *b* – white matte paper, *c* – case of aluminum, *d* – sand paper with gradation of 150

Table 1 presents the values of k_d , k_s and n for various materials.

Value of coefficients k_d , k_s and n

Table 1

Material	Value of coefficients		
	k_d	k_s	n
Tin foil	0	1	34
CD	0.02	0.98	130
Aluminum	0.05	0.95	30
Blue duct tape	0.1	0.9	40
Red slightly shiny paper	0.49	0.51	50
Gray paper slightly matte	0.5	0.5	10
White shiny paper	0.73	0.27	264
Blue sand paper	0.87	0.13	6
Red sand paper	0.88	0.12	82
White matte paper	0.89	0.11	4

The values presented in Table 1 varies according to the type of material. Coefficient k_d varies from 0 for tin foil (glossy reflection) to 0.89 for white matte paper (almost diffuse reflection). The coefficient n is smallest for matte white paper (the reflection is blur Fig. 3c) while for white shiny paper it is 264 which means that the reflection is very sharp (it is confirmed in Fig. 3a).

Conclusions

The approach presented above confirms that Phong model can be used to model the intensity and maximum range. In addition the model parameters for some materials were experimentally measured. Obtained results confirms the theoretical basis described in (RAPINSKI, KOWALCZYK 2011). Designed test device works well and can be used to determine Phong model parameters for various materials. The Phong model with obtained parameters can be used for example to unify the intensity parameter while scanning the cylindrical objects (make the intensity independent from the incidence angle).

Translated by JACEK RAPINSKI

Accepted for print 17.06.2011

Reference

- GREGORY J., LANDER J. 2009. *Game Engine Architecture*. A K Peters, Ltd.
- KOWALCZYK K., RAPINSKI J. 2011. *Investigating the error sources in reflector less EDM*. Journal of Surveying Engineering (in print).
- KRUAPECH S., WIDJAJA J. 2010. *Laser range finder using Gaussian beam range equation*. Optics Laser Technology, 42(5): 749.
- RAPINSKI J., KOWALCZYK K. 2011. *The modelling of a reflectorless range finder maximum range with Phong model*. Reports on Geodesy. Warszawa (in print).
- SABATINI R., RICHARDSON A. 2010. *RTO-AG-300-V26 Airborne Laser Systems Testing and Analysis*. NATO Research and Technology Organization.

STATISTICAL ANALYSIS OF THE FOURTH PRECISE LEVELLING CAMPAIGN IN POLAND

Adam Łyszkowicz¹, Anna Bernatowicz²

¹ Chair of Land Surveying and Geomatics
University of Warmia and Mazury in Olsztyn

² Chair of Land Surveying
Koszalin University of Technology

Key words: levelling networks, random errors, systematic errors.

Abstract

Paper presents statistical evaluation of accuracy of levelling network measured in Poland in years 1999–2001. The analysis was done using 16 150 misclosures from the double levelling of the sections, 382 misclosures from the double levelling of the lines and 133 loops misclosures. The statistical analysis was conducted by the regression method, correlation method and the analysis of variance. It results that the measured height differences have various accuracy (analysis of variance), and that systematic errors are changing according to the value and sign. The existence of systematic errors causes that the successive neighboring sections of some levelling lines are correlated. The correlation in the majority of the lines is not statistically essential.

STATYSTYCZNA OCENA DOKŁADNOŚCI CZWARTEJ KAMPANII NIWELACJI PRECYZYJNEJ W POLSCE

Adam Łyszkowicz¹, Anna Bernatowicz²

¹ Katedra Geodezji Szczegółowej
Uniwersytet Warmińsko-Mazurski w Olsztynie

² Katedra Geodezji
Politechnika Koszalińska

Key words: wyrównanie sieci, błędy przypadkowe, błędy systematyczne.

Abstrakt

W pracy przedstawiono statystyczną ocenę dokładności sieci niwelacji precyzyjnej pomierzonej w Polsce w latach 1999–2001. Do analizy wykorzystano 16 150 odchylek z podwójnej niwelacji odcinków, 382 odchyłki z podwójnej niwelacji linii oraz 133 odchyłki zamknięć poligonów. Analizę

przeprowadzono metodą regresji, korelacji i metodą analizy wariancji. Z przeprowadzonych analiz wynika, że pomierzone różnice wysokości mają zróżnicowaną dokładność (analiza wariancji) oraz że błędy systematyczne są różne co do wartości i znaku. Istnienie błędów systematycznych powoduje, że kolejne sąsiednie odcinki niektórych linii niwelacyjnych są skorelowane. Korelacja w większości linii nie jest statystycznie istotna.

Introduction

A priori accuracy of a levelling network traditionally is estimated by the Lallemand's and Vignal's formulas. Such estimation of all four levelling campaigns in Poland was conducted in the work (ŁYSZKOWICZ, BERNATOWICZ 2010). Since 1950s to analyze levelling data the statistical methods were employed, mainly analysis of variance. The main goal of this work is applying the statistical analysis to better understanding the behavior of the structure of the errors in the Polish precise levelling network measured in 1999–2002.

Analyzing systematic and random errors in the levelling networks one suppose that the misclosures ρ_i from forward and backward levelling can be express as a sum

$$\rho_i = \Delta_i + \varepsilon_i \quad (1)$$

where Δ_i is a systematic error and ε_i is a random error.

Random errors vary from setup to setup of a instrument and their stochastic character can be express by

$$E(\varepsilon_i) = 0, \quad E(\varepsilon_i^2) = \sigma_\varepsilon^2, \quad E(\varepsilon_i \varepsilon_j) = 0 \quad (2)$$

The systematic errors are equally or similarly contained in some or all heights differences. If these errors are also considered as a stochastic values, their characteristics can be described as

$$E(\Delta_i) = \mu_\Delta, \quad E(\Delta_i^2) = \sigma_\Delta^2, \quad E(\Delta_i \Delta_j) = \text{cov}(\Delta_i \Delta_j) \neq 0 \quad (3)$$

According to equations (2), (3) the main difference between systematic and random errors is in the covariance does not equal zero. Systematic errors lead to correlations between height differences.

This paper presents a comprehensive discussion of regression analysis, analysis of variance and analysis of correlation applied to the fourth precise levelling campaign in Poland. The regression analysis was used to show how systematic errors affecting levelling lines. Analysis of variance shows that the

systematic effects are different for each line and analysis of correlation was used to show the degree of correlations between the neighboring sections.

First time the analysis of variance was applied to examination of the levelling network in the Nile Delta (WASSEF 1955) and concerned rather small network consisting of 2450 km. In Poland analysis of variance first time was applied to analysis of levelling network by (TYRA 1983). He conducted analysis of levelling network measured in 1953–1955 which was composed of 10 303 sections. The basic defect of this work is that the author analyzed misclosures $\frac{\rho}{l}$, which have different accuracy and do not fulfill the assumption of analysis of variance.

In the paper (LEWANDOWICZ 1994) the estimation of the sources of errors and their influence on the results of levelling measurements was done. The evaluation of the observation was done with the use of statistical methods such as: the method of empirical moments, statistical tests and the method of the estimation of empirical distribution function. In practical calculations the results of the levelling measurements from years 1974–1979 were used.

Similarly as in the previous work in this study the misclosures $\frac{\rho}{l}$ were used, which have no the same accuracy. Similar defect is in the paper (ŁYSZKOWICZ, LEOŃCZYK 2005), where to the levelling network measured in 1999–2001, in the analysis of variance, the misclosures $\frac{\rho}{l}$ were used incorrectly.

Below is described such a method of normalization of the misclosures ρ , λ and φ which removes the dependence from the length, and thus gives the misclosures with the same accuracy.

If we assume that the result of forward δH^g and backward δH^p measurement of the levelling section is a stochastic variables with the normal distribution $N(\mu, \sigma)$ then the expected value of measured heights differences is equal:

$$E(\delta H^g) = E(\delta H^p) = \mu \quad (4)$$

and the variance of height difference is:

$$\text{var}(\delta H^g) = \text{var}(\delta H^p) = \sigma_0^2 l \quad (5)$$

where l is a length of levelling line and σ_0^2 is a variance of height differences of the section 1 km long from the survey in one direction.

If we consider the misclosures ρ which is the difference from forward and backward measurement, then its expected value is equal:

$$E(\rho) = 0 \quad (6)$$

and variance of such stochastic variable ρ is:

$$\text{var}(\rho) = \text{var}(\delta H^g) - 2 \text{cov}(\delta H^g, \delta H^p) + \text{var}(\delta H^p) \quad (7)$$

where $\text{cov}(\delta H^g, \delta H^p)$ denoted covariance of the variables δH^g and δH^p .

If we assume that the random variables are independent then the covariance will be equal zero and all variances will be identical and the equation (7) will be reduce to the form:

$$\text{var}(\rho) = 2 \text{var}(\delta H) = 2\sigma_o^2 l \quad (8)$$

To compare misclosures ρ counted from sections measurements with various lengths, one should standardize them in the following way:

$$\rho_u = \frac{\rho}{\sqrt{2l}} \quad (9)$$

since the expected value of such standardized misclosures ρ_u is equal zero:

$$E(\rho_u) = 0 \quad (10)$$

while the variance is:

$$\text{var}(\rho_u) = \frac{1}{2l} \text{var}(\rho) = \frac{1}{2l} 2\sigma_o^2 l = \sigma_o^2 \quad (11)$$

for all the lengths l of the sections of the levelling network.

In a case of the line misclosures λ , which is a sum of section misclosures ρ consisting of given line, the variance of λ is the sum of all variances ρ :

$$\text{var}(\lambda) = 2\sigma_o^2 l_1 + 2\sigma_o^2 l_2 + \dots + 2\sigma_o^2 l_n = 2\sigma_o^2 L \quad (12)$$

where L is a line length.

Standardized discrepancy λ_u is defined in the following way:

$$\lambda_u = \frac{\lambda}{\sqrt{2L}} \quad (13)$$

because only variance of such random variable is equal σ_o^2 .

If a few lines create the loop then the sum of mean height differences, corrected due to gravity and other systematic factors should be equal zero. However in practice, one receives the certain loop misclosures which can be expressed by the formula:

$$\varphi = \sum_{i=1}^n \Delta H_i^{sr} \quad (14)$$

where n is a number of levelling traverses. Variance of a random variable φ be:

$$\text{var}(\varphi) = \frac{1}{2} \sigma_o^2 l_1 + \frac{1}{2} \sigma_o^2 l_2 + \dots = \frac{1}{2} \sigma_o^2 \sum l_i = \frac{1}{2} \sigma_o^2 F \quad (15)$$

where F is the length of levelling traverse and σ_o^2 is variance of height differences 1 km length measured in one direction. Standardized misclosures φ_u is defined in the following way:

$$\varphi_u = \varphi \sqrt{\frac{2}{F}} \quad (16)$$

since the variance of such variable is equal σ_o^2 for all length F of levelling traverses.

The fourth precise levelling campaign in Poland

The fourth precise levelling campaign in Poland started in 1999 and was finished in 2003 (Fig. 1). The network consists of 16 150 sections with average length 1.1 km, 382 lines with average length about 46 km, 135 loops, and 245 nodal points. Total length of levelling lines is 17 516 km. The levelling lines were measured with Zeiss Ni002 (66% measurements), Zeiss DiNi 11 (31% measurements), Topcon NJ (3% measurements) e.g. (PAZUS 2001). Rod scale corrections, rod temperature corrections, tidal corrections and normal Molodensky corrections were introduced to the raw measured of height differences.

From the field measurements we have 16 150 section discrepancies ρ , 382 line discrepancies λ and 133 loop misclosures φ . In table 1 is given statistical character of these misclosures.

On the basis of the misclosures ρ , λ and φ the accuracy of the fourth levelling campaign was evaluated using so called "old" formulas and the



Fig. 1. The levelling network of the fourth campaign

following results were obtained. The root mean square error m_1 of height differences counted from misclosures ρ is ± 0.278 mm, the root mean square error m_2 of height differences counted from misclosures λ is ± 0.519 mm and the root mean square error m_3 of height differences counted from misclosures φ is ± 0.826 mm (BERNATOWICZ 2010).

Table 1

Statistical character of misclosures ρ , λ , φ

Specification	ρ	λ	φ
Number of discrepancies	16 150	382	133
Mean [mm]	+0.07	2.74	0.27
Std dev. [mm]	± 0.58	6.89	12.54
Min [mm]	-1.83	-20.41	-31.49
Max [mm]	1.82	20.83	28.83
Skewness	0.08	-0.40	0.21
Kurtosis	-0.01	0.30	-0.10

The first, the simplest assessment of a successful network adjustment of the fourth campaign is described in (ŁYSZKOWICZ, JACKIEWICZ 2005). The adjustment of the network was done as the minimally constrained adjustment and the standard deviation of height differences equal ± 0.88 mm was obtained. Identical evaluation of the accuracy of the campaign IV was obtained in the network adjustment carried out in the study (GAJDEROWICZ 2005).

Statistical analysis of standardized discrepancies

ρ_u , λ_u and φ_u

In order to perform the statistical analyses, the discrepancies ρ , λ and φ were normalized according to formulas (9), (13) i (16). The results of calculations are given in table 2.

Table 2
Statistical characteristic of normalized discrepancies ρ_u , λ_u i φ_u (BERNATOWICZ 2010)

Specification	ρ_u	λ_u	φ_u
Number of discrepancies	16 150	382	133
Mean [mm]	0.05	0,28	0.02
Std dev. [mm]	± 0.39	± 0.68	± 1.17
Min [mm]	-1.06	-1.86	-2.62
Max [mm]	1.13	1.55	2.64
Skewness	-0.10	-0.58	0.18
Kurtosis	-0.66	-0.06	-0.16

Statistical hypothesis test was conducted to verify if the mean of discrepancies is not significantly different from zero. To see whether the mean of the discrepancies is significantly different from zero, the student t test was applied to each mean at the 0.05 level of significance to test the null hypothesis $H_0: \mu = \mu_0$ against alternative hypothesis $H_1: \mu \neq \mu_0$. The variable t_0 may be computed from (MIKHAIL 1976):

$$t_0 = \frac{\bar{x} - \mu_0}{\frac{s}{\sqrt{n}}} \quad (17)$$

Rejection of the hypothesis H_0 on the level of significance α on the advantage of the alternative hypothesis $H_1: \mu \neq \mu_0$, follows when $|t_0| \geq t_{\alpha/2}$.

In the case of testing the significance of the mean value of the discrepancies ρ_u we have: $\bar{x} = 0.05$ mm, $s = \pm 0.39$ mm, $n = 16\ 150$, $\mu = 0$. Computed value of

t_0 is 16.29 and critical value of t at $\alpha = 0.05$ and 16 149 degree of freedom is 1.96, therefore the hypothesis that the mean value is equal 0.05 mm should be accepted. In the case of mean value of discrepancies λ_u we have $t_0 = 8.04$ and critical value of t is 1.97 what indicate that the hypothesis that mean value is equal 0.28 mm should be accepted. In the last case, if we consider the mean value of discrepancies φ_u we have $t_0 = 0.20$ and because the critical value of t is 1.98 the hypothesis that the mean value is zero should be accepted.

Table 3
The results of goodness fit of the empirical expansion of discrepancies ρ_u with normal expansion

Line	Test χ^2			Line	Test χ^2		
	χ^2 practical	degree of freedom	χ^2 theoretical		χ^2 practical	degree of freedom	χ^2 theoretical
29	9.41	3	7.81	141	4.05	4	9.49
32	7.44	4	9.49	147	2.22	4	9.49
36	0.42	3	7.81	154	7.66	5	11.07
41	2.10	2	5.99	170	5.17	6	12.59
44	3.79	6	12.59	192	2.35	4	9.49
54	2.42	5	11.07	196	3.67	5	11.07
92	7.49	3	7.81	198	3.45	5	11.07
97	5.10	5	11.07	206	3.10	4	9.49
118	7.88	6	12.59	217	4.65	5	11.07
119	3.82	7	14.07	225	1.35	2	5.99
121	2.37	7	14.07	236	2.67	6	12.59
131	2.73	4	9.49	284	2.70	4	9.49
133	7.07	7	14.07	319	1.19	3	7.81
135	3.61	7	14.07	335	4.13	5	11.07
137	2.93	6	12.59	337	7.42	6	12.59

Analysis of variance assumed that discrepancies ρ_u of a levelling line should have normal distribution. The investigation of the goodness of fit of the empirical expansion of discrepancies ρ_u with the normal expansion was conducted using the χ^2 test. The results of computation are given in table 3. From table 3 is seen that practical statistics χ^2 are always smaller than the theoretical (with except of the line 29). This means that discrepancies ρ_u of examine levelling lines have the normal expansion and that main assumption of the analysis of variance is fulfilled.

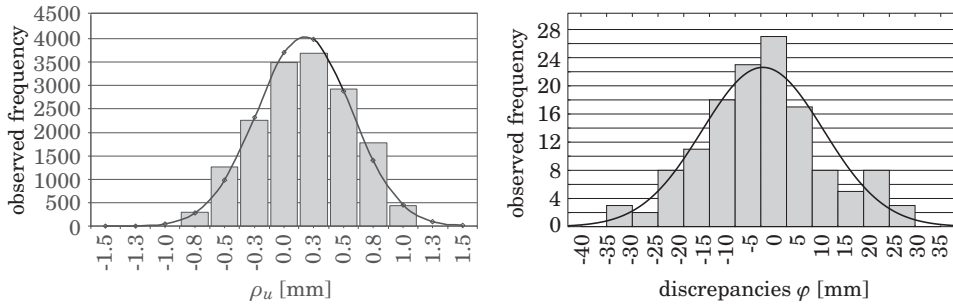


Fig. 2. Histogram of 16 150 standardized discrepancies ρ_u ($\chi^2_{pr} = 263.0, \chi^2_{teor} 12.6$), histogram of 133 standardized discrepancies φ_u ($\chi^2_{pr} 8.52, \chi^2_{teor} 12.6$)

The computed values of skewness and excess (table 2) show that the data sets of discrepancies ρ_u and λ_u created for the whole levelling network do not have the normal expansion, while the set of discrepancies φ_u should rather have the normal expansion. Investigations conducted with the use of the χ^2 test confirm these presumptions. The lack of the fit of the sets of empirical distributions of ρ_u and λ_u with the normal expansion means that discrepancies ρ_u and λ_u are apparently affected by systematic errors. Only empirical distribution of discrepancies φ_u fits to the normal distribution (Fig. 2).

Linear regression

Linear regression can be used to find the function relating two or more variables. In our case the values of d (distance) are regarded as fixed (error free) and the values of successive $\Sigma\rho$ are the measured values (see Fig. 3).

From this drawing results, that the empirical graph of successive sums can be approximated by the straight the line. It inclination gives evaluation of the systematic error on 1 km of the levelling line. In the considered case this systematic error is 0.09 mm/1 km.

In the way described above the systematic errors were computed for 30 lines (Tab. 4). The lines chosen to the analysis have the length more than 75 km. The average length of the lines is 82 km, and the average number of sections in a line is 70. Average systematic error computed for this set of lines is 0.09 mm/1 km and accuracy estimation of this error is very credible because its value is 10 times smaller than the value of the error itself.

From (Tab. 4) results, that the systematic errors of the measured height differences consisting of the levelling line are not typical systematic errors and

they are changing in a size as in sign. One can conduct the similar analysis for discrepancies λ , but the investigation of the sum of discrepancies λ have no sense and therefore the direct dependence of discrepancies λ are studied in the respect to a length L of a line.

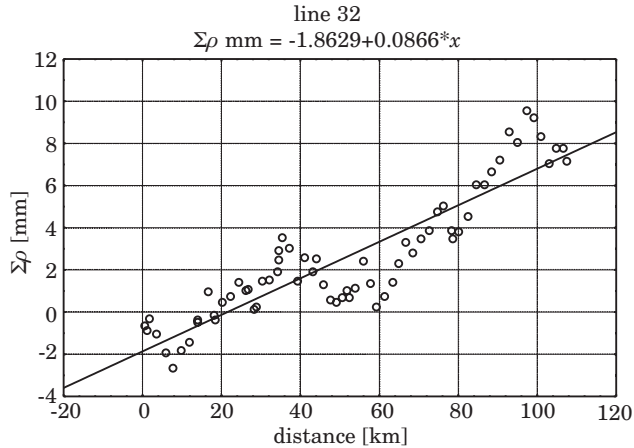


Fig. 3. Increasing, along the line 32, sum of the discrepancies ρ

Table 4

Computed systematic errors for the selected 30 lines of the levelling network (see Fig. 1)

Line	Number of section	Length of line in km	Systematic error and its accuracy in mm		Line	Number of section	Length of line in km	Systematic error and its accuracy in mm	
			δ	m_δ				δ	m_δ
29	68	82.03	0.17	0.01	141	79	95.29	0.07	0.02
32	67	107.41	0.09	0.01	147	100	83.13	0.09	0.01
36	59	76.57	0.04	0.005	154	69	76.07	0.06	0.00
41	60	82.53	0.10	0.004	170	102	92.32	0.11	0.00
44	75	91.93	0.18	0.01	192	76	79.57	0.15	0.00
54	56	77.51	-0.08	0.01	196	65	81.82	0.14	0.00
92	58	80.84	0.05	0.01	198	61	98.99	0.11	0.01
97	67	71.59	0.10	0.01	206	66	88.49	-0.29	0.01
118	67	83.73	0.15	0.004	217	59	83.85	0.11	0.01
119	82	96.31	0.21	0.01	225	76	79.01	0.03	0.01
121	83	83.53	0.10	0.01	236	66	82.18	0.24	0.01
131	52	63.81	0.11	0.01	284	76	87.55	0.13	0.01
133	87	88.56	-0.15	0.003	319	60	76.79	0.23	0.01
135	76	85.07	0.14	0.01	335	78	87.60	-0.13	0.00
137	77	90.48	0.17	0.01	337	78	79.26	0.21	0.01

On the figure 4 is shown the graph of the 383 discrepancies λ in respect to the length of the levelling lines. From figure results that the longer is line the larger value of discrepancies it has, which can be interpreted as accumulation of the successive systematic errors. In our case the estimated systematic error from discrepancies λ , evaluated by the regression line, is (0.07 ± 0.02) mm/km.

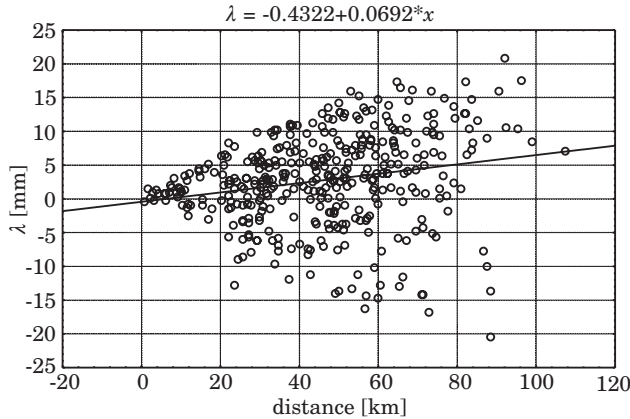


Fig. 4. Graph of the 383 discrepancies λ in respect to the length of the levelling line

The systematic error of the levelling network also can be estimated the by the method of linear regression from the discrepancies φ of the loop misclosures (Fig. 5).

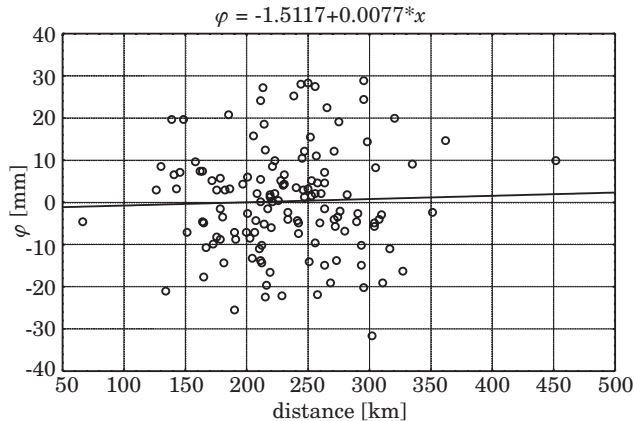


Fig. 5. The graph of 133 discrepancies φ in respect to the length of the loop

From figure 5 results that there is no practically dependence between the length of the loop and the discrepancies φ .

From conducted in the present chapter investigations results, that observations of height differences of a sections (average length of a section 1.1 km) are affected by the systematic errors considerably. Observations of height differences of a line (average length of the line 46 km) are affected less by systematic errors and the levelling loops where the average length is 232 km, do not practically are affected by the systematic errors. This means that systematic errors behave initially as traditional systematic errors and than they increase and after crossing of certain length of the levelling line they behave as accidental errors and in adding up give zero.

Correlation

It was showed in the previous chapters that the measured height differences of a sections were affected by the systematic errors. These errors can cause correlations between the successive sections of a line what results from the formula (3). Determination of these correlations will be conducted below.

In the work (LUCHT 1983) and (BERNATOWICZ 2010) the correlation of neighboring sections is defined in the following way:

$$r_t = \frac{\sigma_{D_t}^2}{2\sigma_\rho^2} - 1 \quad (18)$$

where variances $\sigma_{D_t}^2$ i σ_ρ^2 were estimated as:

$$s_{D_t}^2 = \frac{\Sigma D_t^2}{n_{D_t}} \quad s_\rho^2 = \frac{\Sigma \rho^2}{n} \quad (19)$$

and D_t is define as

$$D_t = \rho_i + \rho_j \quad \text{dla} \quad t = j - i = 1, 2, \dots, n - 1 \quad (20)$$

In the present work the coefficient of the correlation r_1 was computed for 30 test lines given in table 4. The analysis was conducted for the normalized discrepancies ρ_u according to the formula (9). On the basis of so normalized discrepancies the sums describe by the formula (20) were created and empirical standard deviations $s_{D_t}^2$ and s_ρ^2 were computed and then the empirical coefficients of the correlation r_1 .

Table 5

Computed coefficients of correlation r_1 for the individual levelling lines

Line	r_1	z	Line	r_1	z	Line	r_1	z
29	0.24	1.97	121	0.13	1.17	196	-0.14	-1.11
32	-0.01	-0.08	131	0.31	2.24	198	-0.13	-1.00
36	0.19	1.44	133	0.31	2.94	206	0.44	3.75
41	-0.18	-1.37	135	0.25	2.18	217	0.004	0.03
44	0.14	1.20	137	0.24	2.11	225	0.09	0.77
54	-0.13	-0.95	141	0.33	2.99	236	0.33	2.72
92	0.10	0.74	147	0.13	1.29	284	0.27	2.37
97	-0.17	-1.37	154	-0.28	-2.34	319	0.16	1.22
118	0.19	1.54	170	0.18	1.81	335	-0.15	-1.31
119	0.10	0.89	192	-1.79	-0.21	337	0.01	0.09

The question comes into being or the counted correlation coefficients r_1 are essential from the statistics point of view. To check this condition the test described in (MIKHAIL 1976) was applied and the hypothesis $H_0: r_1 = 0$ in respect to the hypothesis $H_1: r_1 \neq 0$ was applied. For large n variable

$$z = \frac{\sqrt{n-3}}{2} \ln \left(\frac{1+r}{1-r} \right) \quad (21)$$

has the normal distribution and the hypothesis H_0 is accepted when

$$-z_{\alpha/2} < z < z_{\alpha/2} \quad (22)$$

When H_0 is rejected the two random variables in question are said to be significantly correlated at the level α . In our case variable z should be inside the interval -1.93 and +1.93 if the level $\alpha = 0.05$ is assumed. From the table 5 it is seen that in the case of the ten lines (bold letters) the correlation coefficients are between 0.25 and 0.44 and are statistically significant. The remaining twenty lines has correlation coefficients less than 0.25 and they are no significant.

Analysis of variance

Various systematic factors act on the measurements of the height differences of the different lines and one can conclude about it from the analysis variance of discrepancies ρ_u . The analysis of variance serves to the verification of the hypothesis about the equality of a mean value of a tested samples by

comparison their variances. In this method the tested sample of the size n is divided into m groups. In our case tested sample contains all discrepancies ρ_u of the forward and backward levelling of a sections in the network and the levelling lines form a groups.

One verifies the hypothesis about the equality of a mean values compute for each group (levelling line). If this hypothesis is true, then all tested samples come from the same expansion (BRANDT 2002) what in the case of levelling means that the same systematic error are present in all measurements.

Computational diagram given in (BRANDT 2002, p. 456) for 382 levelling line was applied to verify the hypothesis about equality of mean value of forward and backward levelling of a levelling sections. Discrepancies were normalized according to the formula (9). The whole calculations was executed in Excel. Suitable numerical values are written down in table 6.

Table 6
Comparison of the results obtained from the analysis of variance for discrepancies ρ_u

Variance [mm ² /km]		Sum of squares	Degree of freedom	$F > F_{1-\alpha}$
Between lines	0,434	165,47	381	3,02 > 1,12
Within lines	0,144	2268,85	15 768	
Total	0,151	2434,32	16 149	

From table 6 results, that for the studied sample of discrepancies ρ_u on the level of significance $\alpha = 0.05$, statistic F is 3,018 while its theoretical value $F_{1-\alpha}$ for $k_1 = 380$ and $k_2 = 15\ 767$ is 1,124. This means, that the variances are not equal, because of different systematic errors presented in the analyzed observations. The results of analyses, show on inhomogeneity of the accuracy of the analyzed network. Such heterogeneity of the network also shows that studied sample of all 16 150 discrepancies does not possess normal expansion (see chapter 3).

Summary

Discrepancies ρ , λ and φ from the double levelling of a sections, lines and the loop closures have no the same accuracy because they are dependent on the length. Therefore one should apply formulas (9), (13) and (16) to normalized them. The empirical expansion of discrepancies ρ_u consisting of individual levelling lines is characterized by normal expansion (chapter 3) which make

possible applying the analysis of variance to study the levelling network. However the empirical expansion of the discrepancies ρ_u of the whole levelling network does not show the normal expansion. Similarly the empirical expansion of all discrepancies λ_u have no the normal expansion, while the empirical expansion of all deviations φ_u has the normal expansion.

From the conducted linear regression results, that lines clearly are affected by systematic errors, but these errors are not typical systematic errors and they are changing to size and sign.

The occurrence of systematic errors causes that the successive measurements of the height differences of the sections are correlated (chapter 5). It results that the degree of the correlation is different to the value (from 0.01 to 0.44) and the sign and, that the majority of the correlations are not essential from the statistical point of the view.

The analysis of variance confirms that the accuracy of the measurements of the height differences in the whole network are not homogeneous what means various systematic factors in the individual lines.

From the carried out analysis results that in a *a priori* estimation of accuracy of levelling network the largest difficulty is proper definition of the systematic errors and their influence on the accuracy of a levelling networks.

Translated by AUTORS

Accepted for print 27.10.2011

References

- BERNATOWICZ A. 2010. *Analiza korelacji w krajowej sieci niwelacji precyzyjnej*. Praca doktorska, UWM Olsztyn.
- BRANDT S. 2002. *Analiza danych*. Wydawnictwo Naukowe PWN.
- GAJDEROWICZ I. 2005. *Ocena dokładności krajowej sieci niwelacji precyzyjnej I klasy pomierzonej w latach 1997–2003*. Technical Sciences, Supplement 2, UWM Olsztyn.
- LEWANDOWICZ E. 1994. *Analiza kompozycji błędów w niwelacji precyzyjnej*. Rozprawa doktorska, Akademia Rolniczo-Techniczna w Olsztynie.
- LUCHT H. 1983. *Neighbourhood correlations among observations in levelling networks*. H. Pelzer, W. Niemeier (eds.) *Precise levelling*, 38 Contribution to the Workshop on Precise Levelling held in Hannover, Fed. Rep. of Germany, 16–18 March 1983, pp. 315–326.
- ŁYSZKOWICZ A., BERNATOWICZ A. 2010. *Accuracy evaluation of the successive campaigns of the precise levelling in Poland*, Technical Sciences, 13.
- ŁYSZKOWICZ A., JACKIEWICZ A. 2005. *Adjustment of Polish precise levelling network using Geolab package*. Proceedings of the 6th International Conference “Environmental Engineering”, Vilnius, Lithuania.
- ŁYSZKOWICZ A., LEOŃCZYK M. 2005. *Accuracy of the last precise levelling campaign in Poland*. EUREF symposium, Vienna.
- MIKHAIL E.M. 1976. *Observations and least squares*. Dun-Donnelley, New York.
- PAŹUS R. 2001. *National Report of Poland to EUREF2001*. International Association of Geodesy / Section I – Positioning; Subcommission for Europe (EUREF) Report on the Symposium of the IAG Subcommission for Europe (EUREF) in Dubrovnik, Croatia, 16–18 May 2001.

- REMMER O. 1975. *Levelling errors, In Statu Nascendi*. Geodatiski Institut, Meddelelse 51, Kobenhavn.
- TYRA J. 1983. *Zastosowanie analizy wariancyjnej i kowariancyjnej do badania dokładności państwowej niwelacji precyzyjnej I klasy*. Geodezja i Kartografia, 32(4).
- WARCHAŁOWSKI E. 1954. *Niwelacja geometryczna*. PPWK, Warszawa.
- WASSEF A.M. 1955. *Statistical analysis of discrepancies in levelling with applications to the first-order levelling of the Nile Delta*. Bulletin Géodésique, 36.

**DETERMINATION OF RESIDUAL
PSEUDO-CHEMICAL ENERGY AND ENERGY
DISSIPATIVE DURING REVERSIBLE MARTENSITIC
TRANSFORMATION IN $\text{Ni}_{52,2}\text{Mn}_{21,3}\text{Ga}_{26,5}$ ALLOY**

Miroslaw Bramowicz

Chair of Materials and Machinery Technology
University of Warmia and Mazury in Olsztyn

K e y w o r d s: shape memory alloys, reversible martensitic transformation, Heusler alloys, Ni-Mn-Ga.

A b s t r a c t

In this paper we present results of an analysis of the influence of annealing time on the residual pseudo-chemical energy and dissipative energy $F_{\text{dis}}(z)$ during reversible martensitic transformation. Analysis was performed without equilibrium temperature and basis on the model proposed in the study: (LIKHACHEV 1998).

From designated courses of residual non-chemical and pseudo-chemical dissipative energies come, that carried thermal treatment causes significant changes of them.

Immediately after casting the studied alloy shows continuous increase of the dissipative energy with increasing of martensite fraction. After annealing at the time from 1+0 h, curves $F_{\text{dis}}(z)$ have a curve close to constant function whereas beyond this range show dynamic increasing or decreasing of dissipation energy.

**WYZNACZENIE RESZTKOWEJ ENERGII SPRĘŻYSTEJ ORAZ ENERGII
ROZPRASZANEJ PODCZAS ODWRACALNEJ PRZEMIANY MARTENZYTYCZNEJ
W STOPIE $\text{Ni}_{52,2}\text{Mn}_{21,3}\text{Ga}_{26,5}$**

Miroslaw Bramowicz

Katedra Technologii Materiałów i Maszyn
Uniwersytet Warmińsko-Mazurski w Olsztynie

Słowa kluczowe: stopy z pamięcią kształtu, odwracalna przemiana martenzytyczna, stopy Heuslera, Ni-Mn-Ga.

A b s t r a c t

W pracy przedstawiono wyniki przeprowadzonej analizy wpływu czasu wygrzewania próbek stopu $\text{Ni}_{52,2}\text{Mn}_{21,3}\text{Ga}_{26,5}$ na resztkową energię sprężystą oraz energię dyssypowaną $F_{\text{dis}}(z)$ podczas odwracalnej przemiany martenzytycznej. Analizę przeprowadzono z pominięciem temperatury równowagi fazowej na podstawie modelu zaproponowanego w pracy LIKHACHEVA (1998).

Z wyznaczonych przebiegów zmian resztkowej energii sprężystej oraz energii rozpraszanej wynika, że przeprowadzona obróbka termiczna powoduje znaczne ich zmiany. W stanie bezpośrednio po wytopie badany stop wykazuje ciągle wzrost energii rozpraszanej wraz ze wzrostem zawartości frakcji martenzytu. Po zastosowaniu wygrzewania w czasach 1+20 h, krzywe $F_{\text{dis}}(z)$ mają przebieg zbliżony do funkcji stałej, natomiast poza nim wykazują dynamiczny wzrost bądź spadek energii dyssypowanej.

Introduction

Ni-Mn-Ga alloys compose intermetallic compound described by general formula X_2YZ . They are among to the so-called Heusler's alloys group. They are characterized by a lot of unique properties such as: structural (e.g. the ability to form modulated super-structures), functional (the ability to reversible martensitic transformation) and magnetic.

Stoichiometric, intermetallic compound with density $\rho = 8.148 \text{ g/cm}^3$ crystallizes at $\approx 1380\text{K}$ temperature, creating at room temperature super-structure, face-centred cubic structure *fcc* (L2₁ No 225) and high order degree of atomic packing in crystallographic lattice up to 98% (AYUELA 1999, BISWAS 2006). Unit cell of high temperature (austenite) phase consists of 16 atoms, however, according to literature sources the lattice parameter (a_0) contains in the range of 5,822+5,825 Å (MARTYNOV 1992, STUHR 1995, VASIL'EV 2003, ZHELUDEV 1995).

Putting the austenitic phase (A) into cooling below characteristic temperature M_s (martensite start) crystal lattice undergoes homogenous deformation to the system of lower symmetry, form low-temperature phase (martensite – *M*). This transformation is reversible by thermal impact. Fundamentals parameters, which characterize each reversible martensitic transformation, are characteristic temperatures: the beginning and end of phase transition (M_s – martensite start, M_f – martensite finish, A_s – austenite start, A_f – austenite finish) and temperature determined thermodynamic equilibrium state (T_0) between occurred phases. Characteristic temperatures can be determined by scanning differential calorimetry (BRECZKO 2005). While, the temperature T_0 describes the experimentally determined by Cornelis and Wayman (CORNELIS 1976) equation (1), which was used among others in the work (KHOVALIO 2004, ROMERO 2003, AHLERS 2003, HUO 1998).

$$T_0 = \frac{M_s + A_f}{2} \quad (1)$$

But as comes from the papers (LIKHACHEV 1997, 1998) their define and value determination is debatable.

The aim of the work

The aim of this study is carrying out the thermodynamic analysis of reversible martensitic transformation occurred in the $\text{Ni}_{52,2}\text{Mn}_{21,3}\text{Ga}_{26,5}$ alloy. The analysis was performed according to the algorithm proposed in study: (LIKHACHEV 1998) which omits temperature of thermodynamic equilibrium (T_0).

The object and methodology of the study

The object of this study were samples of $\text{Ni}_{52,2}\text{Mn}_{21,3}\text{Ga}_{26,5}$ alloy which were undergone homogenizing treatment.

Homogenization process was performed in a tube furnace R09 type in argon atmosphere. The temperature of homogenization was determined by literature study, generally basing on papers: (BESSEGHINI 2001, KHOVAILO 2004). Studies published in the cited papers shows that the thermal treatment of Heusler's alloys affects on the structure, phases volume and lattice parameters.

In order to study the effect of homogenization time on the structure of the $\text{Ni}_{52,2}\text{Mn}_{21,3}\text{Ga}_{26,5}$ alloy were carried out homogenization treatment at 1173K in different annealing time.

During the homogenizing treatment samples were heated and cooled to room temperature in the furnace. In all cases, the heating time (t_1) was 45min, and the annealing time ($t_w = t_2 - t_1$) for individual samples is summarized in Table 1. The whole process ended with slow cooling (in furnace) to room temperature (T_p).

Table 1
Statement of annealing time of individual samples

Sample designation	P0	P1	P2	P3	P4	P5
t_w [h]	after casting	1	5	10	20	60

In order to perform thermodynamic analysis according to described below algorithm, were carried out calorimetric measurements (DSC). Measurement was performed with NETZSCH DSC204 instrument at constant heating/cooling rate of 10 K/min in the range 173÷473 K. As protective gas was used argon (Ar). In the limit temperatures of analyzed range i.e. 173 K and 473 K was used 5 min holding in order to stabilize thermodynamic processes that may occur.

Before measurement, calorimeter was calibrated by finding the melting point of pure indium (*In*).

Kinetics of reversible martensitic transformation proceeded in this alloy, based on the analysis of thermal hysteresis loop trajectory and so called elastic coefficients was reported earlier in paper (BRECZKO 2007).

Thermodynamic parameters describing reversible martensitic transformation

To analyze the kinetics of reversible martensitic transformation was used the algorithm and thermodynamic parameters proposed and widely described in papers (LIKHACHEV 1998). Likhachev, based on the first and second law of thermodynamics, introduces parameters that describe:

- pseudo-chemical (Δu_p) transformation energy,
- residual non-chemical energy (φ) – depended on volume martensite fraction during transformation: $M \rightarrow A$ and $A \rightarrow M$,
- pseudo-chemical equilibrium temperature (T_{0p}).

Parameters mentioned above and dissipative energy (F_{dis}) which is a result of internal friction are described by equations (2)-(5) (LIKHACHEV 1998):

$$\Delta u_p = \Delta s \int_0^1 dz T_{eq}(z) = \Delta s T_{0p} \quad (2)$$

$$\varphi(z) = \Delta s \int_0^z dz (T_{eq}(z) - T_{0p}) \quad (3)$$

$$T_{0p} = \int_0^1 dz T_{eq}(z) \quad (4)$$

$$F_{\text{dis}}(z) = -\frac{1}{2} \Delta s [T_+(z) - T_-(z)] \quad (5)$$

where:

z – martensite volume fraction,

$T_{eq}(z)$ – represents the dissipative thermoelastic equilibrium line described by equation (6) (LIKHACHEV 1998):

$$T_{eq}(z) = \frac{1}{2} [T_+(z) - T_-(z)] \quad (6)$$

where: (+) – means temperature achieved during heating (transformation $M \rightarrow A$), while (–) – means temperature achieved during cooling cycle ($A \rightarrow M$).

According to the mentioned model, the energy balance in each point of reversible martensitic transformation, in heating and cooling cycle is described by the following equation (7) (LIKHACHEV 1998):

$$\Delta s T_{eq}(z) = \Delta u_p + \frac{d\varphi(z)}{dz} \pm F_{dis}(z) \quad (7)$$

Results and discussion

The performed thermodynamic analysis, based on the methodology proposed in paper (LIKHACHEV 1998), allows to better understanding of the impact of heat treatment on the kinetics of reversible martensitic transformation which occurs in $\text{Ni}_{52,2}\text{Mn}_{21,3}\text{Ga}_{26,5}$ alloy.

From plotted courses of residual non-chemical energy and dissipative forces showed in Fig. 1a and Fig. 1b, follow that the thermal treatment causes significant thermal changes in both residual non-chemical potential $\varphi(z)$ and forces F_{dis} dissipative during internal friction. Transformation $A \rightarrow M$ occurred in $\text{Ni}_{52,2}\text{Mn}_{21,3}\text{Ga}_{26,5}$ alloy after the melt has continuous increase of the dissipative energy with increasing fraction of martensite (Fig. 1b), while after annealing at a time $t=0$ h, curves $F_{dis}(z)$ take the characteristic shape. In the range $z \approx 0,1 \div 0,9$, function $F_{dis}(z)$ becomes similar to a constant, and beyond this range shows dynamic increase or decrease of dissipative energy.

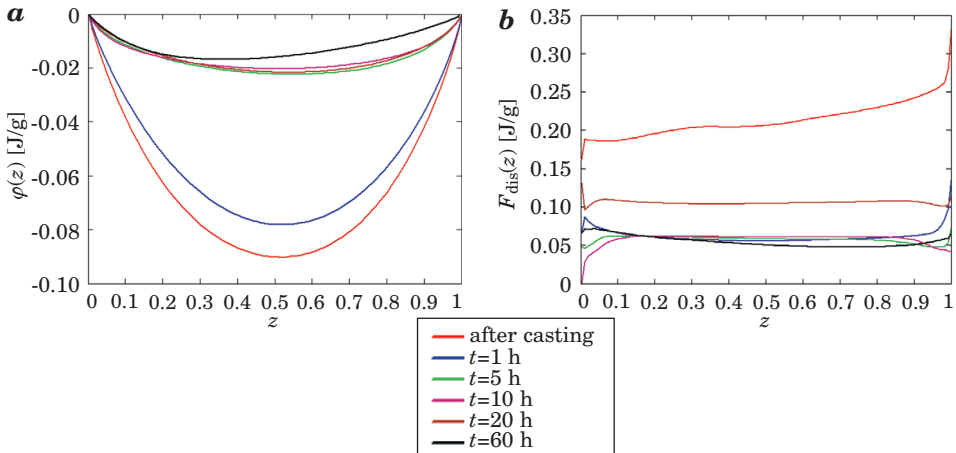


Fig. 1. Changes of: a) residual non-chemical energy, b) dissipative energy

Follows from the residual potential, that it achieves a minimum for the $z(T_{eq} = T_{0p})$, above the minimum its function $\varphi(z)$ is increasing. As it comes clear from Fig. 1a minima $\varphi(z)$ for samples P0-P4 coincide (with some

approximation), while in the plotted curve of function $\varphi(z)$ for P5 sample its minimum has significant shift in the direction of prevailing fraction of austenite. This situation may suggest a formation of different crystallographically martensite, or most likely the increase of the quantity of variants self-accommodation groups of martensite crystallites. In this case the growth of martensite plates is inhibited by a previously established crystallite of low-temperature phase. Detailed results of these calculations are presented in Table 2.

Table 2
Values of pseudo-chemical equilibrium temperature, pseudo-chemical transformation energy and energy dissipative during transformations: $A \rightarrow M$ and $M \rightarrow A$

Marking the sample	The time of warming up [h]	T_{op} [K]	Δu_p [J/g]	$\int_0^1 F_{dis}(z)$ [J/g]
P0	0	278.0	4.985	0.214
P1	1	282.5	5.365	0.062
P2	5	284.0	3.975	0.058
P3	10	284.5	3.983	0.058
P4	20	284.0	4.687	0.105
P5	60	289.0	1.734	0.055

Conclusions

Based on carried out experiment it was found, that applied heat treatment caused changes of residual non-chemical energy and dissipative energy. After applying the 60-hour soaking, the value of dissipative energy in the consequence of internal friction, decreased quadruple. It is probably a result of less extend of defected structure compared to the state after casting. However, function courses $\varphi(z)$ and $F_{dis}(z)$ plotted basing on the quoted model, as well as the distribution of their peaks, represent in the vivid way the kinetics of martensitic transformation.

Translated by AUTORS

Accepted for print 20.06.2011

References

- AHLERS M. 2003. *Stability of martensite in noble metal alloys*. Materials Science and Engineering, A349: 120–131.
- BESSEGHINI S., PASQUALE M., PASSARETTI F., SCIACCA A., VILLA E. 2001. *NiMnGa polycrystalline magnetically activated shape memory alloy: a calorimetric investigation*. Scripta Mater. 44: 2681–2687.

- BISWAS C., BANIK S., SHUKLA A.K., DHAKA R.S., GANESAN V., BARMAN S.R. 2006. *Surface composition and electronic structure of $Ni_{2+x}Mn_{1-x}Ga$ studied by X-ray photoelectron spectroscopy*. Surface Science 600: 3749–3752.
- BRECZKO T., BRAMOWICZ M. 2005. *Calorimetric and microscopic study of Ni-Mn-Ga polycrystalline alloy*. Proceedings of SPAS, 9: 57–60.
- BRECZKO T., BRAMOWICZ M. 2007. *Changes of thermal hysteresis during homogenisation process of Ni-Mn-Ga polycrystalline alloy*. Proceedings of SPIE, 6597.
- HUO Y., ZU X. 1998. *On the Three Phase Mixtures in Martensitic Transformations of Shape Memory Alloys: Thermodynamical Modeling and Characteristic Temperature*, Continuum Mech. Thermodyn. 10: 179–188.
- KHOVAILO V.V., KAINUMA R., ABE T., OIKAWA K., TAKAGI T. 2004. *Aging-induced complex transformation behavior of martensite in $Ni_{57.5}Mn_{17.5}Ga_{25}$ shape memory alloy*. Scripta Materialia, 51: 13–17.
- KHOVALIO V.V., OKAWA K., ABE T. 2003. *Entropy change at martensitic transformation in ferromagnetic shape memory alloys $Ni_{2+x}Mn_{1-x}Ga$* , Journal of Applied Physics, 93 (10).
- LIKHACHEV A.A., SEGUI C., CESARI E. 1998. *Non-chemical potentials and dissipative forces in thermoelastic martensitic transformation*. Scripta Materialia, 38(11): 1635–1641.
- MARTYNOV V.V., KOKORIN V.V. 1992. *The crystal structure of thermally- and stress-induced martensites in Ni_2MnGa single crystals*. Journal de Physique III, 2: 739–749.
- ROMERO R., PELEGRINA J.L. 2003. *Change of entropy in the martensitic transformation and its dependence in Cu-based shape memory alloys*. Materials Science and Engineering, A354: 243–250.
- STUHR U., VORDERWISCH P., KOKORIN V.V. 1997. *Spin waves and phonon anomaly in the Heusler alloy Ni_2MnGa* . Physica, B: 135–136, 234–236.
- VASIL'EV A.N., BUCHEL'NIKOV V.D., TAKAGI T., KHOVAILO V.V., ESTRIN E.I. 2003. *Shape memory ferromagnets*. Physics-Uspexhi, 46(6): 559–588.
- ZHELUDEV A., SHAPIRO S.M., WOCHNER P., SCHWARTZ A., WALL M., TANNER L.E. 1995. *Phonon anomaly, central peak, and microstructures in Ni_2MnGa* . Physical Review B, 51: 17.

ANALYSIS AND COMPARISON OF A JOINT CONNECTING MEMBERS IN A ROOF TRUSS

Stefan Dominikowski, Piotr Bogacz

Chair of Civil Engineering and Building Constructions
University of Warmia and Mazury in Olsztyn

Key words: truss, membrane forces, node, gusset plate.

A b s t r a c t

A truss as a planar structure consisting of joined members is dimensioned on certain assumptions which simplify the computational procedure. This paper presents an analysis of a randomly chosen node in a truss. Two cases have been considered. The first one concerned a node in a double-trapeze truss, where gusset plate was used. In the second case, the analyzed truss node consisted of a vertical member and a cross brace connected directly to the bottom chord. Our analysis has demonstrated that, as the references and the design experiments suggest, joining truss members directly does not cause any increase in the membrane forces or stresses.

ANALIZA I PORÓWNANIE POŁĄCZENIA PRĘTÓW W WĘZŁE WIĄZARA KRATOWEGO DACHOWEGO

Stefan Dominikowski, Piotr Bogacz

Katedra Budownictwa i Konstrukcji Budowlanych
Uniwersytet Warmińsko-Mazurski w Olsztynie

Słowa kluczowe: kratownica, siły membranowe, węzeł, blacha węzłowa.

A b s t r a k t

Kratownicę jako ustrój prętowy płaski wymiaruje się z pewnymi założeniami upraszczającymi procedurę obliczeniową. W pracy przedstawiono analizę losowo wybranego węzła kratownicy. Rozpatrzono dwa przypadki. W pierwszym przeanalizowano węzeł kratownicy dwutrapezowej, w którym zastosowano blachę węzłową. W drugim przeanalizowano węzeł kratownicy, w którym słupki i krzyżulec był połączony bezpośrednio do pasa dolnego. Analiza dowiodła, że zgodnie z zaleceniami w literaturze oraz doświadczeniami projektowymi bezpośrednie łączenie prętów nie powoduje wzrostu sił membranowych oraz naprężeń.

Introduction

A truss is a structure consisting of members connected at joints called nodes, which has a geometrically constant shape. It is among the most often designed and made constructions to support steel roofs of industrial buildings. A truss owes its popularity to a relatively light weight of the construction of truss supports, which means highly competitive costs of such roofs. Engineers are keen on designing trusses because of the ease of calculating the internal forces. A wide variety of trusses has found many uses in civil engineering.

Calculating dimensions of trusses

Calculating dimensions of trusses, according to BOGUCKI (1976) and ŻÓŁTOWSKI et al. (2000), is done based on the following assumptions:

1. Members are connected in nodes as hinged joints although in reality these joints are rigid or nearly rigid. For the sake of making the calculations simpler, the effect of stiffness is usually omitted – bending moments in nodes are absent and only axial forces appear in the members.

2. All members are rigid.

3. Axes of the members, passing through the members' centre of gravity, coincide with the geometrical outline of the truss – the node's balance. However, when the axes of the joined members are shifted by no more than 3% of the member's height, the shift need not be included in the calculations (Fig. 1).

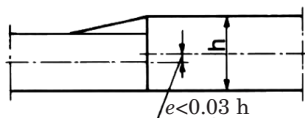


Fig. 1. Negligible shift of axes of truss members

Source: own work based on ŻÓŁTOWSKI et al. (2000).

4. There are no eccentricities or additional bending moments in a node – that is the members are joined concentrically in a node, i.e. axes of gravity intersect in one point.

When this condition is not met while designing a truss, an additional moment of the value $M = N \cdot e$ will appear in the node (Fig. 2). In accordance with the principles of statics, this moment divides itself between all the members meeting in a given node in proportion to their stiffness.

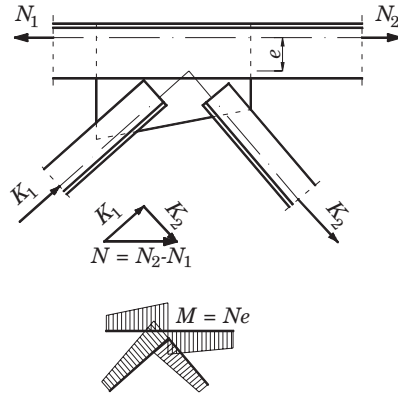


Fig. 2. Including additional moments in a truss node
 Source: own work based on ŻÓŁTOWSKI et al. (2000).

5. All members of a truss should lie in one plane and their cross-section is symmetrical relative to the truss's plane. When this condition is not fulfilled, an additional moment from the bending depending on:

$$\sigma = \frac{N}{A} + \frac{N \cdot e^2}{I},$$

- N – the force acting in the i^{th} member of the truss [N],
 - A – the i^{th} member's cross-section area [mm²],
 - e – eccentricity [mm],
 - I – moment of inertia [mm⁴],
- should be included in the calculations (Fig. 3a, b).

Additional stresses can be omitted when batten plates are placed between gusset plates (Fig. 3c, d).

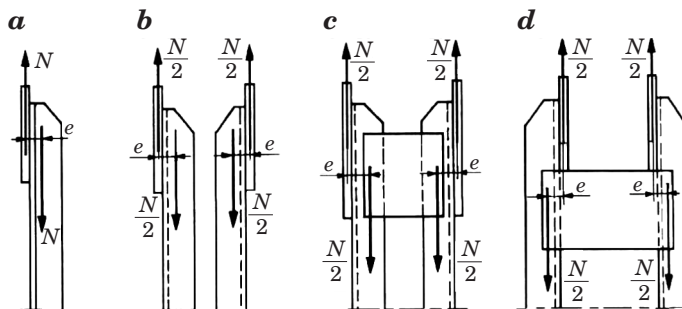


Fig. 3. Connection of members with gusset plates
 Source: own work based on ŻÓŁTOWSKI et al. (2000).

6. Members in joints should be placed symmetrically relative to each member's axis, as this will enable us to avoid additional bending moments in a node.

7. The most important assumption is that external load on a truss is applied to the nodes – this means that only axial forces will appear. If some external load is applied to a member (outside the nodes), bending moments (their approximations) should be included in the calculations and members should be dimensioned as compressed or tensed eccentrically.

When analyzing the above assumptions, and especially the ones concerning hinged joints of truss members, it can be concluded that this is a gross oversimplification, which seems all the more unjustified because construction engineers often use gusset plates in truss member joints. An essential condition for determination of exclusively axial forces in truss members is that all the members are rectilinear, which is not always the case (production flaws, deformation during transport). Additional reasons why node moments should not be omitted is the non-axial connections of members in nodes (Fig. 2). The fact that joints are non-axial causes the appearance of residual moments, which should also be included in the calculations. The non-axiality of truss members often originates from technological or design-related considerations, such as the intention of designing nodes that will be easiest to make. BIEGUS (2003) claims that joints without gusset plates are technologically the easiest type of connection (Fig. 4).

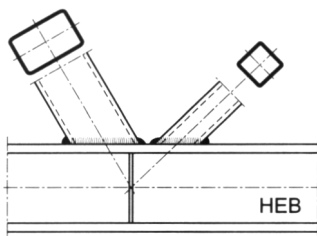


Fig. 4. A truss node without a gusset plate

Source: own work based on ŻÓŁTOWSKI et al. (2000).

The bending moment $M = N \cdot e$ (Fig. 1) which appears in a node with non-axially connected members divides itself among all the members proportionally to their stiffness (BOGUCKI 1976, ŻÓŁTOWSKI et al. 2000).

Planar trusses can be designed as:

- externally statically determinate -simple-supported trusses,
- statically indeterminate trusses – continuous trusses, frames.

The assumption that truss members are connected axially in a node is made because of the ease of calculating internal forces in the members. This ease is due to the assumed internal static determinacy of the truss's structure. It is then possible to apply well-known, classic methods for calculation of internal forces (Ritter method, nodes equilibrium method, Culmann method, and others) (JASTRZĘBSKI et al. 1974). In reality, the structure of a truss is a multiply statically indeterminate construction and assuming its internal static determinacy is far-reaching approximation, which disagrees with the actual work of a designed construction.

Truss members are connected in a node, which can be fitted with a gusset plate or not. Nodes are designed according to an analytical and geometrical method. Both members connected in a node and gusset plates should fulfill several conditions. Both ŻÓŁTOWSKI (2000) and BIEGUS (2003) suggest that vertical members as well as cross braces should be connected directly to the chords and using gusset plates should be avoided.

In the light of the above suggestions and considerations as well as the results of some experimental designs, the usability of gusset plates in trusses has been analyzed.

A computer model

This paper compares values of external forces in a double-trapeze truss in which all the nodes are rigid. It has been assumed that truss chords are stiff and rigidly connected with cross braces and vertical members. Our analysis involved one, randomly selected node, in which non-zero cross brace and vertical member are connected with the bottom chord.

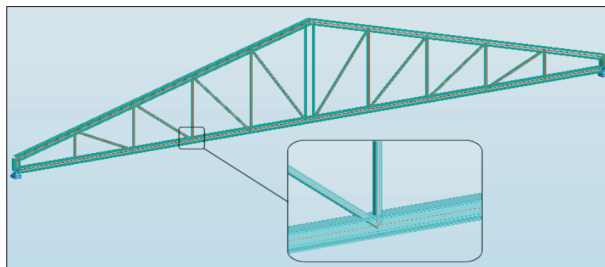


Fig. 5. The analyzed model of a truss with a selected node
Source: Autodesk Robot Structural Analysis Professional 2011, licence no 3251.

The cross brace and vertical member are connected directly to the chord by welding (case I) or via a gusset plate (case II). In order to determine the values

of membrane forces in the members connected in the analyzed node, the latter was isolated by the so-called “rigid connection”. At the same time, in the isolated node, walls of members were replaced by panels, treated as coating, of the thickness equal the thickness of the walls of members connected in the analyzed node. Creating the panels was possible by introducing additional nodes (slave nodes) connected to the main node (master node). Thus, it is possible to analyze maps of any internal forces in the node.

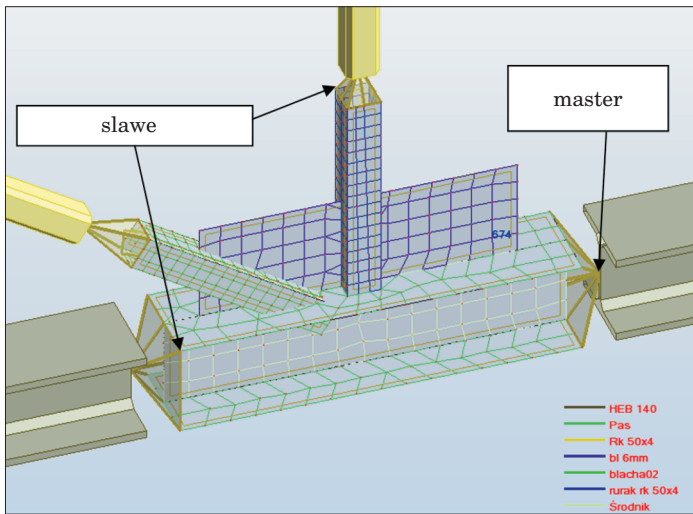


Fig. 6. A computer model of a node – the way of isolating nodes

Source: Autodesk Robot Structural Analysis Professional 2011, licence no 3251.

In one case, a panel simulating a gusset plate was introduced to the node (Fig. 7a); in the other case, the members reaching the node were connected to the chord directly (Fig. 7b).

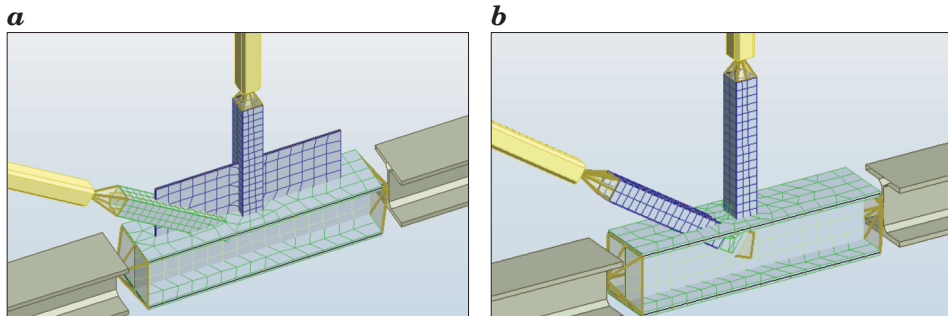


Fig. 7. A computer model of the analyzed node: *a* – with a gusset plate, *b* – without a gusset plate

Source: Autodesk Robot Structural Analysis Professional 2011, licence no 3251.

In both cases, the truss was subjected to a force applied uniformly to the top chord of the truss. This way of loading a truss can simulate loading a purlinless roofing construction. The value of the load was identical in both analyzed cases (with and without a gusset plate) and equalled $q=10\text{kN/}$ Both models were submitted to an analysis according to the Finite Elements Method. The gusset plate is marked as element 247 in our analysis.

Analysis of the results

Figure 8 shows maps of membrane forces x-x in the analyzed node with a gusset plate whereas Figure 9 illustrates maps of membrane forces x-x in the analyzed node without a gusset plate.

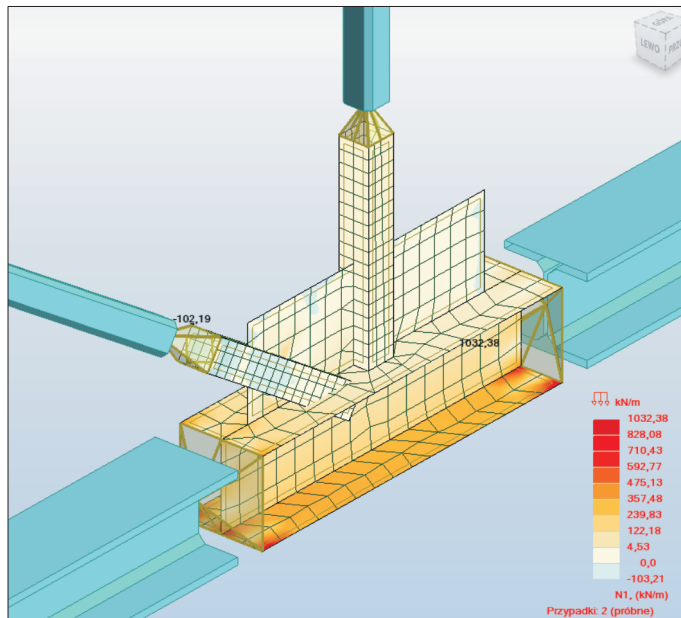


Fig. 8. A map of membrane forces x-x in the analyzed truss node with a gusset plate
Source: Autodesk Robot Structural Analysis Professional 2011, licence no 3251.

Maps of shear stresses in the analyzed node with a gusset plate are presented in Figure 10, while Figure 11 shows maps of shear stress in the node without a gusset plate.

In these figures, the blue colour indicates values of stresses in tangents in the planes of connections between the panels.

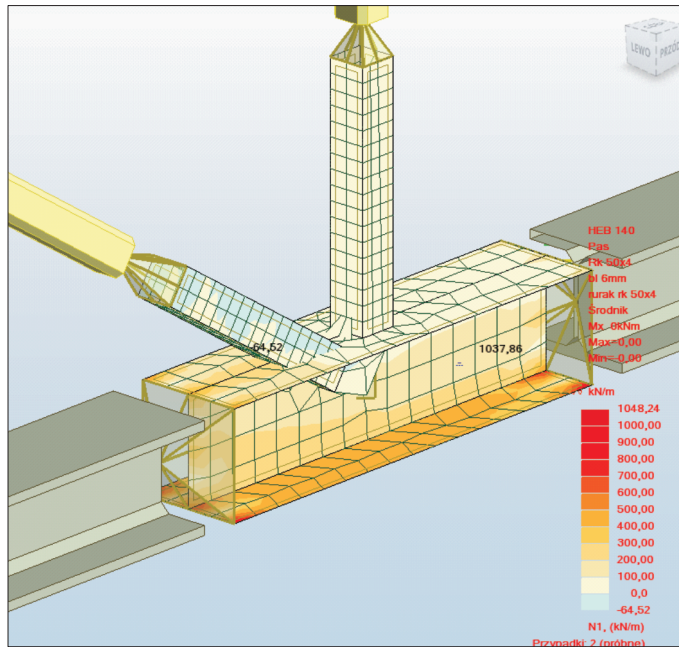


Fig. 9. A map of membrane forces x-x in the analyzed truss node without a gusset plate
 Source: Autodesk Robot Structural Analysis Professional 2011, licence no 3251.

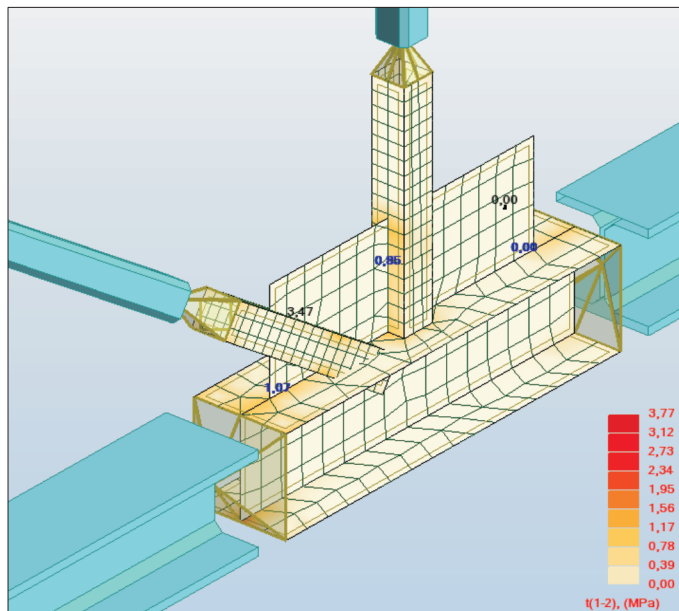


Fig. 10. A map of tangent stresses in the analyzed truss node with a gusset plate
 Source: Autodesk Robot Structural Analysis Professional 2011, licence no 3251.

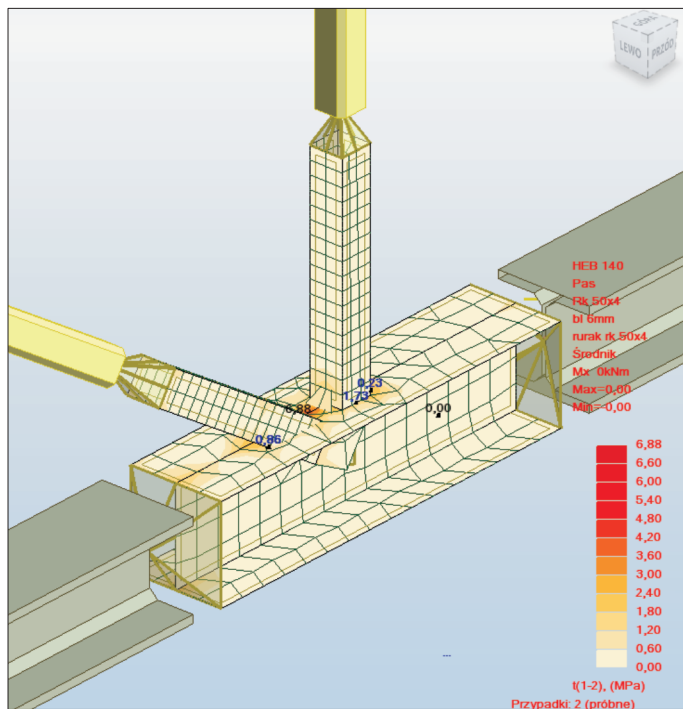


Fig. 11. A map of tangential stresses in the analyzed truss node without a gusset plate
 Source: Autodesk Robot Structural Analysis Professional 2011, licence no 3251.

Values of the extreme external forces alongside the number of the element in which they appear are given in Tables 1 and 2.

Table 1
 Values of the extreme stresses, membrane forces and shear forces in a node with a gusset plate

	σ_{xx} [MPa]	σ_{yy} [MPa]	σ_{xy} [MPa]	N_{xx} [kN/m]	N_{yy} [kN/m]	N_{xy} [kN/m]	τ_{xx} [MPa]	τ_{yy} [MPa]
Max	75.14	27.38	30.52	901.70	286.89	366.28	3.40	2.42
Panel	235	236	235	235	235	235	237	251
Node	421	309	408	421	421	408	661	146
Min.	-58.41	-21.53	-30.53	-233.65	-150.68	-366.34	-4.91	-2.26
Panel	248	236	235	248	236	235	237	251
Node	29	661	398	29	661	398	704	200

Source: the authors.

Table 3
Values of the extreme stresses, membrane forces and shear forces in a node without a gusset plate

	σ_{xx} [MPa]	σ_{yy} [MPa]	σ_{xy} [MPa]	N_{xx} [kN/m]	N_{yy} [kN/m]	N_{xy} [kN/m]	τ_{xx} [MPa]	τ_{yy} [MPa]
Max	74.73	119.95	103.21	896.77	286.68	365.14	1.41	1.07
Panel	235	251	250	235	235	235	249	238
Node	421	578	466	421	421	408	150	461
Min.	-262.12	-264.50	-109.59	-524.23	-529.00	-364.49	-3.46	-1.06
Panel	250	251	251	250	251	235	250	239
Node	463	463	463	463	463	398	76	316

Source: the authors.

Meanwhile, values of the efforts of truss members were compared for the following types of joints:

1. all the members connected in a joint are hinged.
2. the members of the inner truss structure are joined by hinges and connected with continuous truss chords (top and bottom chords)
3. all the members in nodes are connected rigidly.

The results for the both extreme conditions are contained in Table 3.

Table 3
Comparison of values of efforts of truss members

Comparison of bending moments and shifts between three types of joints in a truss		
all hinged joints	continuous chords. hinged vertical members and cross braces	all stiff joints
bending moments [kNm]		
0.3	51.4	79.3
excess of normal stresses [%]		
14.4	39.8	53.2
shift of nodes [m]		
0.04668	0.0433	0.04296

Source: the authors.

Summary

Based on the above analysis, it can be concluded that the recommendation found in many references, suggesting that gusset plates should be avoided in trusses, especially in truss roofs, is substantiated. This is demonstrated by the values of the membrane forces set in Table 1 and Table 2. When gusset plates are used, the value of membrane forces is $N_{xx,max} = 901.70$ kN/m, but when no

gusset plate is fitted, this value is $N_{xx,max} = 896.77$, which is comparable. In addition, the stresses, both tangent and normal ones, in the analyzed nodes yield comparable values.

An important conclusion to be drawn from the above tests is that the extreme values of the forces and stresses do not occur in panel number 247, which is a gusset plate used in the analyzed node.

Translated by JOLANTA IDŹKOWSKA

Accepted for print 22.08.2011

References

- BIEGUS A. 2003. *Stalowe budynki halowe*. Arkady, Warszawa.
- BOGUCKI W. 1976. *Budownictwo stalowe*. Arkady, Warszawa.
- JASTRZĘBSKI P., MUTERMILCH J., ORŁOWSKI W. 1974. *Wytrzymałość materiałów*. Arkady, Warszawa.
- PN-EN 1993-1-8:2006, *Eurokod 3: Projektowanie konstrukcji stalowych*. Część 1-8: *Projektowanie węzłów*.
- ŻÓŁTOWSKI W., FILIPOWICZ A., ŁUBIŃSKI M. 2000. *Konstrukcje Metalowe*. Część I. *Podstawy projektowania*. Arkady, Warszawa.
- ŻÓŁTOWSKI W., ŁUBIŃSKI M. 1992. *Konstrukcje Metalowe*. Część II. *Obiekty budowlane*. Arkady, Warszawa.

THE BASIC EQUATIONS OF FLUID MECHANICS IN FORM CHARACTERISTIC OF THE FINITE VOLUME METHOD

Wojciech Sobieski

Department of Mechanics and Machine Design
University of Warmia and Mazury in Olsztyn

Key words: CFD, Finite Volume Method, balance equations.

Abstract

The article presents the derivation of the basic balance equations in form characteristic of the Finite Volume Method. In the following sections the origin of the balance equation of momentum, mass and energy is presented. Next, the conservation equations in vector form are described. The Finite Volume Method is used in Computational Fluid Mechanics for numerical modeling of fluid flows in wide range. The motivation for writing the article was the difficulty in finding short and concise articles on this subject in the literature. The current article is a first part of a cycle dedicated to the mathematical basis of the Finite Volume Method.

PODSTAWOWE RÓWNANIA MECHANIKI PŁYNÓW W FORMIE CHARAKTERYSTYCZNEJ DLA METODY OBJĘTOŚCI SKOŃCZONYCH

Wojciech Sobieski

Katedra Mechaniki i Podstaw Konstrukcji Maszyn
Uniwersytet Warmińsko-Mazurski w Olsztynie

Słowa kluczowe: CFD, metoda objętości skończonych, równania bilansowe.

Abstrakt

W artykule przedstawiono wyprowadzenie podstawowych równań bilansowych w formie charakterystycznej dla metody objętości skończonych. Przedstawiono pochodzenie równania bilansu pędu, masy i energii, następnie równania zachowania w formie wektorowej. Metoda objętości skończonych jest stosowana w tzw. numerycznej mechanice płynów do numerycznego modelowania przepływów płynów w możliwie szerokim zakresie. Motywacją do napisania artykułu była trudność w znalezieniu podobnego rodzaju krótkich i zwięzłych opracowań na ten temat w literaturze. Artykuł jest pierwszą częścią cyklu poświęconego matematycznym podstawom metody objętości skończonych.

Introduction

The proliferation of computers at the end of the twentieth century allowed for the application of numerical methods, that is, methods of solving mathematical problems using operations on numbers rather than symbolic variables. Results obtained in this way are approximate but the accuracy of the calculations can be selected predetermined depending on the needs. The first consideration of numerical techniques was led by Carl Friedrich Gauss (1777–1855), who based on the works of Leonhard Euler (1707–1783), Joseph Louis Lagrange (1736–1813) and Isaac Newton (1643–1727). The work begun by Gauss resulted in the development of so-called Finite Difference Method (FDM), whose essence is replacing the derivatives occurring in differential equations by the corresponding differential quotients. FDM began to be used to solve various mathematical problems, including issues relating to the mechanics of solids and fluid mechanics. After some time it appeared that the FDM has some limitations that hinder its application to solve more complex physical problems. The search for new possibilities gave rise to the Finite Element Method (FEM), which is more favorable from the point of view of needs of solid mechanics and the Finite Volume Methods (FVM), much more appropriate to the specificity of fluid mechanics. It should be emphasized that in principle each of the methods listed here can be applied to solve the same differential equations; however, it is much more preferable to apply in various areas of physics methods specific to them.

The purpose of this article is to present the equations of fluid mechanics in form which is characteristic of the Finite Volume Methods. It should be stressed that the laws and principles of physics are the same as in the case of classical mechanics (non-numeric), but the way of their presentation is different, as is apparent from the method of reasoning specific to them. A general difference between FDM and the FVM is that the FVM does not apply to discretization of differential equations, but to the space in which they apply. Hence the basis for any action here is the so-called Finite Volume (or Control Volume). It is a virtual, closed by a surface, part of the space, in which then the mathematical considerations are carried out. It is important in that the Finite Volume must be large enough so that the matter inside the volume can be treated as a representative sample of the fluid and small enough so that it can also be regarded as a “discrete” point of the space. A consistent and very general system of balance equations, resulting from the analysis of the phenomena occurring in the Finite Volume, is the basis of computations in absolutely every case of the numerical flow analysis. This aspect distinguishes significantly the numerical fluid mechanics from the classical mechanics, in which, depending on the needs different “individual” laws or formulas are

used: the law of continuity, Bernoulli's law, Navier-Stokes equation, Fourier's law, Fick's law, Forchheimer's law or other, often independent of one another. In the Computational Fluid Mechanics (CFD), these laws also exist but are written in another form. Some of them are a simplified version of one of the general balance equations, while others are merely a supplement (a closure). These issues will be discussed later.

The rest of this article will describe the derivation of balance equations of mass, momentum and energy, in form characteristic of the FVM. It is worth noting that this form replaces gradually the classic derivations based on a virtual cube placed in a Cartesian coordinate system (see the description of the Navier-Stokes equations in ORZECOWSKI et al. (1997) and passes into the general literature related to the fluid mechanics (GRYBOŚ 1998, PUZYREWSKI, SAWICKI 2000). This follows from the fact that the balance equations specific for the FVM are characterized by extraordinary elegance and consistency, unachieved previously in the theory of fluid flows. The motivation to write this article was the observation that in the literature, the authors usually confine themselves to present the basic system of equations, with no explanation of its origin. In addition, comparing the various publications the lack of unified mathematic form can be noted. Sometimes, the basic equations look quite different and difficult to fit together (compare e.g. works (JAMESON, MAVRIPLIS 1985, MUZAFERJAJA, GOSMAN 1997) and CUHNA, FERREIRA 2002). On the other hand, the authors who describe the basic equations of fluid mechanics (e.g. in academic books), do it usually in the classical way, without focusing on the Finite Volume Method. The lack of appropriate derivation was the motivation to create this article. The purpose of the article was to explain to the readers the basic approach to the theory in FVM, and to propose a universal and general form of balance equations.

The idea of balances in a Finite Volume

The mathematical description of fluid flow in FVM approach is created for a volume $V \in \Omega$ closed by a surface S . This surface is oriented by a vector \vec{n} , directed outwards from the volume (Fig. 1). For the Finite Volume it can define two main types of balances: the surface and the volumetric balance. The surface balance describes the possibility to exchange the value of Φ with the surroundings through the fluxes flowing through the surface:

$$\int_S (\Phi \vec{v} \cdot \vec{n}) dS \quad (1)$$

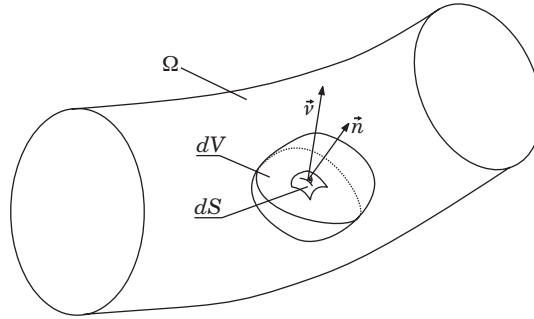


Fig. 1. The Finite Volume

Mathematically the flux is a vector defined as the product of any physical quantity Φ , e.g. mass, momentum or energy, and velocity \vec{v} of flow in the direction perpendicular to the surface (Fig. 2).

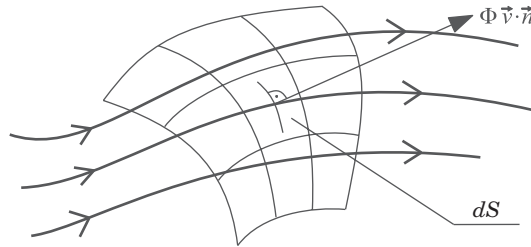


Fig. 2. Visualization of a flux

The volumetric balance describes the possibility to change of value Φ inside the volume V :

$$\int_V (\Phi) dV \quad (2)$$

To facilitate understanding of those balances we can use an example of heat balance in a room. The total heat inside the room can be changed by cooling or heating the walls (e.g. due to changes in outdoor temperature) or by heat sources like heater, various devices that produce heat and the heat generated by people in the room. The other parameters such as mass, momentum and energy can be treated analogically.

Mass balance equation

The total mass m [kg] contained in the volume V [m³] filled by fluid with density ρ [kg/m³] can be calculated as follows

$$m = \rho_{\text{average}} V = \int_V \rho dV \quad (3)$$

The change in mass in the time interval dt [s] is dependent on local fluctuations of density inside the fixed, rigid volume

$$\frac{d}{dt} m = \int_V \frac{\partial \rho}{\partial t} dV \quad (4)$$

In the general case of compressible fluid, the mass in volume V is subject to a compression. As a consequence inside the volume arise free space. To avoid a discontinuity in the flow, this free space must be supplemented by mass from the outside. This means that in time dt a resultant mass flux equal to the difference between mass fluxes flowing into and flowing out through the surface must get inside the volume V :

$$\int_V \frac{\partial \rho}{\partial t} dV = - \int_S (\rho \vec{v} \cdot \vec{n}) dS \quad (5)$$

where $(\rho \vec{v} \cdot \vec{n})$ is an elementary mass flux perpendicular to the surface of the Finite Volume. In the literature it is assumed that a positive sign applies to the effluent stream from the volume, hence the negative sign in the formula (since we consider the compression of mass in the volume). The surface integral on the right side can be converted to a volumetric integral using the Green-Gauss-Ostrogradzki Theorem (GGOT) (EVERSTINE 2010, SHARAFUTDINOV 1994, SAOUMA 2002) then:

$$\int_V \frac{\partial \rho}{\partial t} dV = - \int_V \text{div}(\rho \vec{v}) dV \quad (6)$$

or

$$\int_V \left(\frac{\partial \rho}{\partial t} + \text{div}(\rho \vec{v}) \right) dV = 0 \quad (7)$$

Above integral will be zero, only if the integrand expression to be zero

$$\frac{\partial \rho}{\partial t} + \text{div}(\rho \vec{v}) = 0 \quad (8)$$

Formula (8) represents the final form of mass balance equations. In fact it is a different form of well known and useful mass continuity equation.

Momentum balance equation

According to Newtonian mechanics, the momentum of the body \vec{p} [kg · m/s] is equal to mass m [kg] times velocity \vec{v} [m/s], which in the case of the Finite Volume must be expressed as a volumetric integral (see Eq. (3))

$$\vec{p} = m \vec{v} = \int_V (\rho \vec{v}) dV \quad (9)$$

The change of momentum in time is only possible due to the forces (the change of momentum is equal to the force)

$$\frac{d\vec{p}}{dt} = \frac{d}{dt} \int_V (\rho \vec{v}) dV = \vec{F}_T \quad (10)$$

where the total force \vec{F}_T is a sum of the mass forces \vec{F}_V [N] related to the mass contained in the volume V and the external forces \vec{F}_S [N] from the impact of neighboring material on the surface S

$$\vec{F}_T = \vec{F}_V + \vec{F}_S \quad (11)$$

Equation (11) can add to the formula (10)

$$\frac{d}{dt} \int_V (\rho \vec{v}) dV = \vec{F}_V + \vec{F}_S \quad (12)$$

The formula (12) shows that the momentum can be changed as a result of:
 – mass forces (source forces) \vec{F}_V operating inside the volume V . The mass forces are divided into external (e.g. gravity, electromagnetic force) and internal

forces (e.g. inertial forces). Mass forces act on each particle of fluid, therefore the resultant of forces acting on the Finite Volume V must be calculated as an integral of the volume (where \vec{f}_V it the unit mass force [N]):

$$\vec{F}_V = \int_V (\rho \vec{f}_V) dV \tag{13}$$

- external surface forces \vec{F}_S acting on the surface S of the volume V . Surface forces may be the hydrostatic and hydrodynamic pressure, internal friction or friction of fluid on the rigid walls (where \vec{f}_S is unit surface force [N] and \vec{T} is the total stress tensor acting on the surface S):

$$\vec{F}_S = \int_S \vec{f}_S dS = \int_S (\vec{T} \vec{n}) dS = \int_V \text{div}(\vec{T}) dV \tag{14}$$

Therefore, the change of momentum (12) is equal to the sum of the variations of forces acting on the volume V

$$\frac{d}{dt} \int_V (\rho \vec{v}) dV = \int_V (\rho \vec{f}_V) dV + \int_V \text{div}(\vec{T}) dV \tag{15}$$

The left-hand side of equation (15) may be transformed using the Reynolds Transport Theorem (RTT) (RTT allows one to determine how a given quantity defined within a control volume changes with time as the control volume deforms) (WHITAKER 1976) and next GGOT to the form

$$\frac{d}{dt} \int_V (\rho \vec{v}) dV = \int_V \frac{\partial(\rho \vec{v})}{\partial t} dV + \int_S (\rho \vec{v} \otimes \vec{v} \vec{n}) dS = \int_V \frac{\partial(\rho \vec{v})}{\partial t} dV + \int_V \text{div}(\rho \vec{v} \otimes \vec{v}) dV \tag{16}$$

then

$$\int_V \frac{\partial(\rho \vec{v})}{\partial t} dV + \int_V \text{div}(\rho \vec{v} \otimes \vec{v}) dV = \int_V \text{div}(\vec{T}) dV + \int_V (\rho \vec{f}_V) dV \tag{17}$$

Leaving signs of integrals we obtain

$$\frac{\partial(\rho\vec{v})}{\partial t} + \text{div}(\rho\vec{v} \otimes \vec{v}) = \text{div}(\vec{T}) + \rho\vec{s}_b \quad (18)$$

where $\rho\vec{s}_b = \rho\vec{f}_V$ is treated as the general record of the source forces.

The resultant of surface forces can be decomposed into two parts: normal and tangent.

$$\vec{T} = -p\vec{I} + \vec{\tau}^t \quad (19)$$

These forces are represented on the surface S , respectively, by the total shear stress tensor $\vec{\tau}^t$ and the spherical stress tensor (pressure) $-p\vec{I}$ (negative sign due to convention taken out by Cauchy). We then obtain:

$$\frac{\partial(\rho\vec{v})}{\partial t} + \text{div}(\rho\vec{v} \otimes \vec{v}) = \text{div}(-p\vec{I} + \vec{\tau}^t) + \rho\vec{s}_b \quad (20)$$

The total shear stress tensor $\vec{\tau}^t$ consists usually of the sum of viscous molecular stress tensor $\vec{\tau}^m$ and turbulent Reynolds stress tensor $\vec{\tau}^R$.

$$\frac{\partial(\rho\vec{v})}{\partial t} + \text{div}(\rho\vec{v} \otimes \vec{v}) = \text{div}(-p\vec{I} + \vec{\tau}^m + \vec{\tau}^R) + \rho\vec{s}_b \quad (21)$$

Sometimes it is needed to add other stress tensor, e.g. diffusion stress tensor $\vec{\tau}^{diff}$ or radiation stress tensor $\vec{\tau}^{rad}$. Equation (21) is the final form of momentum balance equation.

Energy balance equation

In the balancing of energy, one usually only takes into account the kinetic energy

$$E_k = \frac{m\vec{v}^2}{2} = \int_V \rho \frac{\vec{v}^2}{2} dV \quad (22)$$

and the internal energy

$$U = mu = \int_V (\rho u) dV \quad (23)$$

where u is the specific density of internal energy, which is the energy of all forms of molecular motion, especially the movement of heat. The sum of kinetic and internal energy gives the total energy E :

$$E = \int_V \rho \left(\frac{\vec{v}^2}{2} + u \right) dV = \int_V (\rho e) dV \quad (24)$$

where e is the sum of both components.

Change in total energy of a fluid may occur as a result of acting (GRYBOŚ 1998):

– work done by the mass forces

$$A_V = \int_V (\rho \vec{f}_V \cdot \vec{v}) dV \quad (25)$$

and surface forces (normal and tangential)

$$A_S = \int_V (\vec{f}_S \cdot \vec{v}) dS = \int_V (\vec{T} \vec{v} \cdot \vec{n}) dS \quad (26)$$

– internal heat (sources of energy)

$$Q_V = \int_V (\rho q_V) dV \quad (27)$$

and external heat, supplied to the volume V through the surface S at time dt :

$$Q_S = \int_V (\vec{q}_S^t \cdot \vec{n}) dS \quad (28)$$

The total energy change can be written as

$$\frac{d}{dt} \int_V (\rho e) dV = \int_V (\rho \vec{f}_V \cdot \vec{v}) dV + \int_S (\vec{T} \vec{v} \cdot \vec{n}) dS + \int_S (\vec{q}_S^t \cdot \vec{n}) dS + \int_V (\rho q_V) dV \quad (29)$$

After comparison of all integrals

$$\frac{d}{dt} \int_V (\rho e) dV = \int_V (\rho \vec{f}_V \cdot \vec{v}) dV + \int_V \text{div}(\vec{T} \vec{v}) dV + \int_V \text{div}(\vec{q}_S^t) dV + \int_V (\rho q_V) dV \quad (30)$$

The left-hand side of the formula (30) can be transformed using the RTT and GGOT to the form

$$\frac{d}{dt} \int_V (\rho e) dV = \int_V \frac{\partial(\rho e)}{\partial t} dV + \int_S (\rho e \vec{v} \cdot \vec{n}) dS = \int_V \frac{\partial(\rho e)}{\partial t} dV + \int_V \text{div}(\rho e \vec{v}) dV \quad (31)$$

After substituting (31) to (30) we obtain

$$\int_V \frac{\partial(\rho e)}{\partial t} dV + \int_V \text{div}(\rho e \vec{v}) dV = \int_V (\rho \vec{f}_V \cdot \vec{v}) dV + \int_V \text{div}(\vec{T} \vec{v}) dV + \int_V \text{div}(\vec{q}_s) dV + \int_V (\rho q_V) dV \quad (32)$$

This equation is equivalent to

$$\frac{\partial(\rho e)}{\partial t} + \text{div}(\rho e \vec{v}) = \rho \vec{f}_V \cdot \vec{v} + \text{div} [(-p\vec{I} + \vec{\tau}^t) \vec{v}] + \text{div}(\vec{q}_s) + \rho q_V \quad (33)$$

Energy change caused by the work of the mass forces and energy sources can be saved together in the form of total energy source $\rho s_e = \rho \vec{f}_V \cdot \vec{v} + \rho q_V$, then:

$$\frac{\partial(\rho e)}{\partial t} + \text{div}(\rho e \vec{v}) = \text{div} [(-p\vec{I} + \vec{\tau}^t) \vec{v}] + \text{div}(\vec{q}_s) + \rho s_e \quad (34)$$

Both members under divergence signs on the left side can be linked to the formulation

$$\frac{\partial(\rho e)}{\partial t} + \text{div}(\rho e \vec{v}) = \text{div} [(-p\vec{I} + \vec{\tau}^t) \vec{v} + \vec{q}_s] + \rho s_e \quad (35)$$

To simplify the notation, the bottom index s in the external heat flux will be omitted in further considerations. The total heat flux \vec{q}^t is usually the sum of the molecular heat flux \vec{q}^m and turbulent heat flux \vec{q}^R , then

$$\frac{\partial(\rho e)}{\partial t} + \text{div}(\rho e \vec{v}) = \text{div} [(-p\vec{I} + \vec{\tau}^m + \vec{\tau}^R) \vec{v} + \vec{q}^m + \vec{q}^R] + \rho s_e \quad (36)$$

Sometimes it is needed to add other fluxes, e.g. diffusive heat flux \vec{q}^{diff} or radiative heat flux \vec{q}^{rad} .

The formula (36) can be treated as the final version of the energy equation. Sometimes, however, this equation is further transformed until a form containing the enthalpy. To achieve this, the expression $-p\vec{I}$ under the sign of divergence's can be moved to the left side of the equation (34), then

$$\frac{\partial(\rho e)}{\partial t} + \text{div} (\rho e\vec{v} + \rho\vec{v}) = \text{div} [(\vec{\tau}^m + \vec{\tau}^R) \vec{v} + \vec{q}^m + \vec{q}^R] + \rho s_e \quad (37)$$

or in other form

$$\frac{\partial(\rho e)}{\partial t} + \text{div} \left[\rho \left(e + \frac{p}{\rho} \right) \vec{v} \right] = \text{div} [(\vec{\tau}^m + \vec{\tau}^R) \vec{v} + \vec{q}^m + \vec{q}^R] + \rho s_e \quad (38)$$

Note that the expression $e + \frac{p}{\rho}$ is the enthalpy. Denoting the symbol of the enthalpy h , we get the alternative version of the energy balance equation.

The vector form of balance equations

In the introduction it was said that the essence of the FVM are volume and mass balances, described by integrals (1) and (2). However, in the next part of the article the integrals were omitted, and the final shape of the obtained equations has a differential form. This is due to the specific needs of the FVM. Note that the mass, momentum and energy balances can be saved in one system of equations

$$\left\{ \begin{array}{l} \frac{\partial \rho}{\partial t} + \text{div} (\rho\vec{v}) = 0 \\ \frac{\partial(\rho\vec{v})}{\partial t} + \text{div} (\rho\vec{v} \otimes \vec{v}) = \text{div} (-p\vec{I} + \vec{\tau}^m + \vec{\tau}^R) + \rho\vec{s}_b \\ \frac{\partial(\rho e)}{\partial t} + \text{div} (\rho e\vec{v}) = \text{div} [(-p\vec{I} + \vec{\tau}^m + \vec{\tau}^R) \vec{v} + \vec{q}^m + \vec{q}^R] + \rho s_e \end{array} \right. \quad (39)$$

in which successive terms of individual equations have the same logical structure. It turns out that those terms can be treated together, and the entire system of balance equations can be solved by “columns” using the same numerical technique for all elements of a column. It is one of the most

important features of FVM, allowing, inter alia, relatively easy to add new equations, as long as they have a common structure which matches the template. In practice, which is in numeric codes, the balance equations are solved together in one loop calculation. The number of repetitions of main numerical schemes on n^{th} time level is equal to the total number of balance equations and equations of evolution (this term is explained later).

In the equation (39), the pressure member can be transferred to the left site:

$$\left\{ \begin{array}{l} \frac{\partial \rho}{\partial t} + \text{div} (\rho \vec{v}) = 0 \\ \frac{\partial (\rho \vec{v})}{\partial t} + \text{div} (\rho \vec{v} \otimes \vec{v} + p \vec{I}) = \text{div} (\vec{\tau}^m + \vec{\tau}^R) + \rho \vec{s}_b \\ \frac{\partial (\rho e)}{\partial t} + \text{div} (\rho e \vec{v} + p \vec{I}) = \text{div} [(\vec{\tau}^m + \vec{\tau}^R) \vec{v} + \vec{q}^m + \vec{q}^R] + \rho s_e \end{array} \right. \quad (40)$$

Now in divergence on the left there are only convective parts, which can convert without energy losses. In the divergence on the right there are only parts connected with energy losses: viscosity, turbulence etc. This division is convenient for implementation in numerical codes: other numerical techniques are used to the reversible and other to the dissipative terms. Therefore, it is better to save the system of equations (40) in the so-called vector form (CHMIELNIAK 1996, KUDRYŃSKI et al. 1997, LOBO 1997, WRÓBLEWSKI 2000)

$$\frac{\partial}{\partial t} U + \text{div} (F^c + F^e) = \text{div} (F^v) + S \quad (41)$$

where: U is vector of conservative variables, F^c is the convection flux vector, F^e is recoverable flux vector, F^v is the diffusive flux vector and S is the vector of sources:

$$U = \begin{Bmatrix} \rho \\ \rho \vec{v} \\ \rho e \end{Bmatrix}, F^c = \begin{Bmatrix} \rho \\ \rho \vec{v} \otimes \vec{v} \\ \rho e \vec{v} \end{Bmatrix}, F^e = \begin{Bmatrix} 0 \\ p \vec{I} \\ p \vec{I} \vec{v} \end{Bmatrix}, F^v = \begin{Bmatrix} 0 \\ \vec{\tau}^m + \vec{\tau}^R \\ (\vec{\tau}^m + \vec{\tau}^R) \vec{v} + \vec{q}^m + \vec{q}^R \end{Bmatrix}, S = \begin{Bmatrix} 0 \\ \rho s_b \\ \rho s_e \end{Bmatrix} \quad (42)$$

Only after such a transformation returning to the main idea of balances in the Control Volume is possible. This return gives the so-called integral form

of the conservation equations, which constitutes a form of output for the creation of numerical codes:

$$\frac{\partial}{\partial t} \int_V U dV + \int_V \text{div}(F^c + F^e) dV = \int_V \text{div}(F^v) dV + \int_V S dV \quad (43)$$

or (after using the GGOT and RTT):

$$\frac{\partial}{\partial t} \int_V U dV + \int_S (F^c + F^e) \vec{n} dS = \int_S (F^v) \vec{n} dS + \int_V S dV \quad (44)$$

Summary

In the area of the CFD several classes of equations can be distinguished:

- balance (or transport) equations – describe the balance of a certain size in the macrostructure level (single cell in the grid). Examples are the transport equations of mass, momentum, energy.

- evolution equations – describe the balance of a certain size of the microstructure (in the area of a single grid cell) and are usually a supplement to the basic system of equations. The role of a supplement is to add to the next equations the same structure as in formula (40). The vectors in conservation equations will consist of four, five or more elements, depending on the number of added evolution equations. Examples are the evolution equations of turbulence energy, the degree of dissipation ($k - \varepsilon$) or ($k - \varpi$) turbulence models), vorticity, intermittency and other. The equation of evolution is used generally to describe the phenomenon of turbulence and the number of equations defines a model class. For example $k - \varepsilon$ or $k - \varpi$ turbulence models are 2-equations models.

- kinematics equation – describes the kinematics properties of the fluid. There is only one equation describing the velocity of fluid element deformation. This equation is needed to calculate the viscous molecular stress tensor $\overset{\leftrightarrow}{\tau}^m$.

- constitutive equations – describe the properties of the fluid. Generally there are four types of constitutive equations:

- equation of state (connecting the basic variables, e.g. Clapeyron's equation),
- closure on the stress tensors (usually fluid model and turbulence model),
- closures of the sources (e.g. the gravity, additional heat sources),
- closures of heat transfer (e.g. Fourier law).

The set of equations (40) is the main and basic level of equations in CFD. Note that the system (40) is not complete and needs to be supplemented by many “closures”, that is models describing the individual issues. Depending on these “closures” the equation (40) can be appropriate for a wide range of fluid flows: Newtonian, non-Newtonian, laminar, turbulent, with or without heat transfer or other. It is worth noting that the set of equations (40) applies only to single-phase flow. Issues concerning “closures” and multiphase flows will be discussed on another occasion.

It should be pointed out again that the forms of equations presented in this article are not inconsistent with generally applicable laws of fluid mechanics, although it has a specific character. As already mentioned, the mass balance equation is a generalized version of the classical equation of continuity. Similarly, the momentum balance equation has its classical counterpart: it can be treated as the Navier-Stokes equation or as the reaction equation. The energy balance is in turn a generalized form of the Daniel Bernoulli equation. These compounds can be demonstrated, but it is not the purpose of the article.

The balance equations presented in this paper are very general. They should be treated as a “template” which in each case will undergo modifications depending on the specifics of the flow. It turns out that many of the mathematical models from the various literature sources can be fitted through a relatively simple transformation to the set of equations (40). This issue is very important in practice because it creates a common basis for many different fluid flow issues.

Translated by AUTORS

Accepted for print 7.10.2011

References

- BAUER H.J. 1989. *Überprüfung numerischer Ansätze zur Beschreibung turbulenter elliptischer Stromungen in komplexen Geometrien mit Hilfe konturangepasster Koordinaten*. Dissertation, Karlsruhe.
- CUHNA A.S., FERREIRA W.R. 2002. *Two-Dimensional Transient Finite Volume Difusional Approach to Transport Equations*. *Tendências em Matemática Aplicada e Computacional*, 3(1): 91–100.
- CHMIELNIAK T. 1996. *Transonic flows. Conservation equation*. IX Summer School of Fluid Mechanics, pp. 2–43, Nowa Kaletka, Poland.
- EVERSTINE C.E. 2010. *Analytical Solution of Partial Differential Equations*. Gaithersburg, Maryland, United States. On-line, URL: <http://gwu.geverstine.com/pde.pdf> (15.05.2011).
- GRYBÓŚ R. 1998. *Fundamentals of fluid mechanics*. PWN, Warsaw.
- JAMESON A., MAVRIPLIS D. 1985. *Finite Volume Solution of the Two-Dimensional Euler Equations on a Regular Triangular Mesh*. AIAA 23rd Aerospace Sciences Meeting, January 14–17, Reno, Nevada, United States.
- KUDRYŃSKI A.W., RUSANOW A.W., JERSZOW S.W. 1997. *Numerical method for calculating multi-dimensional gas flow in channels with complex geometry*. Kharkov, Ukraine.
- LOBO M. 1997. *Time-Marching (A step-by-step guide to a flow solver)*. Antony Rowe Ltd, Wiltshire.
- MUZAFERLIJA S., GOSMAN D. 1997. *Finite-Volume CFD Procedure and Adaptive Error Control Strategy*

-
- for *Grid of Arbitrary Topology*. Journal of Computational Physics, 138: 766–787, article no CP975853.
- ORZECZOWSKI Z., PRYWER J., ZARZYCKI R. 1997. *Fluid Mechanics in Environmental Engineering*. WNT, Warsaw.
- PUZYREWSKI R., SAWICKI J. 2000. *Fundamentals of fluid mechanics and hydraulics*. PWN, Warsaw.
- SHARAFUTDINOV V.A. 1994. *Integral Geometry of Tensor Fields*. VSP Utrecht, The Netherlands.
- SAOUMA V.E. 2002. *Lecture Notes*. Introduction to Mechanics of Materials II. Dept. of Civil Environmental and Architectural Engineering, University of Colorado, Boulder.
- SOLODOV V.G. 2001. *The gasdynamics of the exhaust diffusers – computational aspects*. CFD for Turbomachinery Applications, Summer School, part I, pp. 179–196, Gdańsk.
- WHITAKER S. 1976. *Elementary heat transfer analysis*. Pergamon, New York.
- WRÓBLEWSKI W. 2000. *Numerical simulation of flow phenomena in thermal turbines*. Silesian University of Technology, Energetics, 132: 9–214, Gliwice.

INFLUENCE STEEL MANUFACTURING PROCESS X2CrNiMoN25-7-4 ON ITS STRUCTURE

*Paweł Szabracki¹, Tomasz Lipiński¹, Mirosław Bramowicz¹,
Kazimierz Rychlik²*

¹ Chair of Materials and Machinery Technology
University of Warmia and Mazury in Olsztyn

² Department of Mechanised Construction
Institute of Mechanised Construction and Rock Mining

Key words: X-Ray diffraction, XRD, duplex steel.

Abstract

This paper presents results of X2CrNiMoN25-7-4 steel structure investigation. Measurements were carried out in commercial state and after additional solution heat treatment. The structure analysis was carried out based on XRD measurements. Obtained results allowed for determination of structure parameters, phase's volume and lattice defects.

Obtained results suggested, that applied finishing treatments didn't influent on structure parameters and the lattice defects.

WPLYW PROCESU WYTWARZANIA STALI X2CrNiMoN25-7-4 NA JEJ BUDOWĘ STRUKTURALNĄ

Paweł Szabracki¹, Tomasz Lipiński¹, Mirosław Bramowicz¹, Kazimierz Rychlik²

¹ Katedra Technologii Materiałów i Maszyn
Uniwersytet Warmińsko-Mazurski w Olsztynie

² Zakład Obrabiarek i Technologii Montażu
Instytut Mechanizacji Budownictwa i Górnictwa Skalnego

Słowa kluczowe: dyfraktometria rentgenowska, XRD, stal dupleks.

Abstract

W pracy przedstawiono wyniki badań struktury stali X2CrNiMoN25-7-4. Badania przeprowadzono dla stanu komercyjnego materiału oraz po procesie powtórnego przesyłania. Strukturę materiału analizowano na podstawie pomiarów dyfraktometrycznych. Określono parametry sieciowe składników, stopień zdefektowania struktury oraz wyznaczono udziały fazowe. Analiza wyników badań wykazała, że stosowane na etapie produkcji zabiegi wykańczające nie wpłynęły na parametry strukturalne oraz stopień zdefektowania struktury.

Introduction

Properties of chrome-nickel in austenitic-ferritic structure combines advantages and elimination (or substantial minimization) defects of single-phase (ferrite, austenite) stainless steels. Main advantages of this type of material are: high yield and tensile strength and high resistance to stress corrosion and pitting corrosion. These properties make this type of steel, very attractive construction material, mainly in industry: chemical, petrochemical, mining and shipbuilding. They are produced, among others through properly maintained phase proportions of shares in structure of material. In this type of stainless steels ferrite volume fraction is between 40–60%, but optimum mechanical properties and corrosion resistance is achieved with a 50% volume fraction of austenite and ferrite (LEE et al. 2002, LIPIŃSKI et al. 2010). Increase volume fraction of ferrite in stainless steel structure increases yield strength, tensile strength and hardness, while reducing corrosion resistance of material and ductility and toughness. It is particularly important to maintain appropriate phase volume fraction in welded joints in order to ensure performance of material.

During welding processes, as well as during heat treatment in temperature range from 300–1000°C in austenite and ferrite can nucleate and grow vary in terms of chemical composition and structure phases, for example, secondary austenite, many carbides and nitrides, sigma phase σ , or causing so-called. 475°C fragility rich in chromium ferrite α' (NOWACKI 2008, LAI et al. 1995). Presence of 1–2% in structure of sigma phase σ , may reduce toughness of steel by half, and with participation of this phase, more than 5% following a sharp drop in corrosion resistance and almost disappearance of plasticity (LIPIŃSKI 1993, LIPSON 2001).

These steels are produced by continuous casting followed by giving dimensions of material in hot rolling process. After rolling process is used solutioning. In some technologies, last step of production process is also used in cold rolling, as a finishing treatment. Depending on degree of deformation it can introduce stress and plastic deformation.

Production technologies are property of steel mills, and are not made available to their customers.

Through comparative researches, commercial material with material known treated technology, it can be concluded about state of material available commercially.

Aim and methodology of research

Aim of this study was to analyze impact of steel-making process on its structure.

Subject of research in this study were samples of steel X2CrNiMoN25-7-4, taken from cold-rolled sheet of steel.

Due to texture present in rolled materials, in order to consideration of a privileged orientation of crystallites on intensity of diffraction reflexes in carried out calculations taken into account all recorded diffraction reflexes.

To achieve objective of study decided to compare structural parameters of selected steel in a commercial state with steel saturated from temperature 1100°C. Austenitizing time taken for 30 minutes.

Using X-ray diffraction research (XRD) determined lattice parameters of structural components, degree of lattice defects and calculated phase volume fraction.

X-ray diffraction research (XRD)

XRD studies were carried out on X-ray diffractometer XPERT PRO with focusing rays by Bragg-Brentano and registration stepping pulses. Measurements were made in range of 2θ angles from 30–120° using $\text{CuK}\alpha$ radiation and pulse counting time at each angular position, equal to 2 seconds.

Based on recorded diffraction patterns of tested stainless steel determined lattice parameters of ferrite and austenite, determined phases volume fraction of present phases and determined size of coherently scattering regions of X-rays (mosaic blocks) and distortion of lattice, reflecting degree of defects in phase structure of individual components.

Contained in diffraction patterns data describing structure and material properties are associated with location and size of diffraction peaks, so to accurately determine angular positions of individual reflexes and to designate areas contained between curve describing profile of peak and background line was used Winfit program.

Applied program also enabled numerical correction half-width (FWHM) and intensity coming from component of $\text{K}\alpha_2$ X-ray. Profile shape of each reflexes described with Cauchy function, according to which intensity of deflected beam of X-rays are described by formula (1) (SENCZYK 1996).

$$I(\Theta) = I_0 \frac{1}{1 + kx^2} \quad (1)$$

where:

I_0 – intensity of incident beam,

k – function parameter (determined by least square method),

x – scaled value of angle θ .

Shape and position of reflexes are related to physical factors which characterize a given structure, such as: microstresses, size of mosaic blocks, lattice distortion, and instrumental factors. Width of reflexes are defined as so-called integral width expressed as ratio of area contained between curve describing profile of peak and background line to maximum intensity, or as a half-width (FWHM) reflexes (CULLITY 1964). Physical width of diffraction reflexes β is sum of three components: instrumental (β_i), coming from lattice distortion (β_z) and component related to size of crystallites (β_k) (BOJARSKI, BOLD 1970, BOJARSKI, ŁAGIEWKA 1988, CULLITY 1964).

In order to eliminate instrumental broadening, having a significant impact on half-width (FWHM) and integral intensity, thus to set size of blocks and distortions in lattice, performed using standard diffraction pattern of polycrystalline silicon, under same diffractometer operating parameters and conditions as measurement tested samples of stainless steel.

Diffraction pattern of polycrystalline silicon and influence of factors on apparatus half-width of registered reflexes as a function of angle 2θ are shown in Figure 1. For measurement conditions, change width FWHM describes determined formula (2).

$$y(2\theta) = 0,072 + 2\theta \cdot 1,418 \cdot 10^{-3} - (2\theta)^2 \cdot 1,99 \cdot 10^{-5} + (2\theta)^3 \cdot 1,207 \cdot 10^{-7} \quad (2)$$

Formula (2) allows to determine real reflexes width (β_r) which for profiles described with Cauchy function is: $\beta_r = \beta - \beta_i$ (BOJARSKI, ŁAGIEWKA 1988).

Methodology for determining lattice parameters and phase volume fractions

To determine lattice parameters of ferrite (α) and austenite (γ) used linear extrapolation of lattice parameters determined on basis of angular positions of peaks coming from various phases: α and γ and angle of reflection $\Theta = 90^\circ$. As a function of extrapolation was used as described by formula (3) function Nelson-Riley (N-R) (LIPSON 2001).

$$f(\Theta) = \frac{1}{2} \left(\frac{\cos^2(\Theta)}{\sin(\Theta)} + \frac{\cos^2(\Theta)}{\Theta} \right) \quad (3)$$

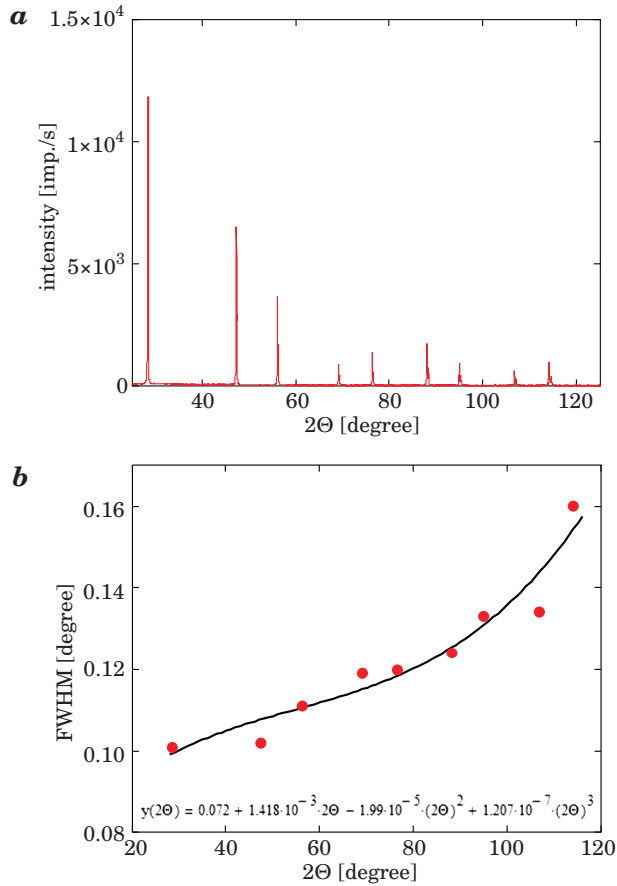


Fig. 1. Diffraction pattern (a) standard of polycrystalline silicon, and relationship (b) showing the diffractometer instrumental broadening, for the measurement conditions

Determination of phase volume fraction by X-ray phase analysis method based on principle, according to which intensity of diffraction peaks depend on fraction of various phases (BOJARSKI, ŁĄGIEWKA 1988, CULLITY 1964).

In case of material with privileged orientation, intensity of reflex coming from each phase describes relationship (4) (BOJARSKI, ŁĄGIEWKA 1988):

$$J_{hkl}^j = K_j' \frac{m_j}{\mu} P_{hkl} \quad (4)$$

where:

m_j – mass fraction of phase j in mixture,

μ – mass absorption coefficient of mixture,

- P_{hkl} – ratio of crystallites are in position satisfying Bragg condition, for planes (hkl) ,
- K' – value described by formula (5) – dependent on constant geometrical conditions (eg. diffractometer radius, cross-sectional area of original beam) during performing diffraction patterns and crystalline structure.

$$K'_j = C \cdot \frac{1}{v^2} \cdot |F_{hkl}|^2 \cdot LP \cdot p \cdot e^{-2M} \quad (5)$$

$|F_{hkl}|^2$ – square structure factor, whose value for austenite and ferrite is respectively: $16f_{sr}^2$ i $4f_{sr}^2$, where f_{sr} is average atomic scattering factor for alloy. Average atomic scattering factor take into account chemical composition of tested steel and atomic fraction of individual elements. Value of this factor for tested material describe formula (6):

$$f_{sr} = 0,62f_{Fe} + 0,27f_{Cr} + 0,06f_{Ni} + 0,02f_{Mo} + 0,01f_N + (4,53f_{Si} + 7,85f_{Mn} + 2f_{Cu} + 1,13f_{Co}) \cdot 10^{-3} + (7,83f_C + 3,93f_P \cdot 10^{-4} + (1,72f_S + 8,33f_{Nb}) \cdot 10^{-5} \quad (6)$$

Values of each atomic factors derived from constituent elements read relation $f_i = f \left(\frac{\sin\theta}{\lambda} \right)$ (i – symbol element), using for this purpose a computer program *Krystalografia2* described in paper (BOJARSKI 1988).

LP – Lorenz–Thomson factor, equal: $\frac{1 + \cos^2(1\Theta)}{\sin^2\Theta \cos\Theta} - \frac{1 + \cos^2(\Theta)}{\sin^2\Theta \cos\Theta}$

p – factor times diffraction planes – determined on basis of tables contained in (CULLITY 1964),

e^{-2M} – temperature coefficient.

Considering above equations, fraction of m-phase in mixture of α and λ can be described as (7):

$$m_{\alpha, \gamma} = \frac{\frac{1}{n} \sum_{i=1}^n \frac{J_{ihkl}^{\alpha, \gamma}}{K_{i\alpha'\gamma}^{\alpha, \gamma}}}{\frac{1}{n} \sum_{i=1}^n \frac{J_{ihkl}^{\alpha, \gamma}}{K_{i\alpha'\gamma}^{\alpha, \gamma}} + \frac{1}{k} \sum_{i=1}^n \frac{J_{ihkl}^{\alpha, \gamma}}{K_{i\alpha'\gamma}^{\alpha, \gamma}}} \quad (7)$$

where: n and k are respectively number of peaks coming respectively from phase α and γ .

Values of basic parameters necessary to carry out phase analysis and results are summarized in tables: 1 and 2.

Factor characterizing structural construction occurring phases can be also size of areas coherently scattering X-rays (mosaic blocks) and a occurring distortion of lattice (BOJARSKI, BOŁD 1970).

In order to determine those parameters was used by Williamson-Hall method (W-H) (BOJARSKI, ŁĄGIEWKA 1988). According to this method, for peak profiles described Cauchy function, total actual diffraction line broadening (β_r) is sum of extensions coming from size of blocks (β_k) and distortion of lattice (β_z), so:

$$\beta_r = \beta_k + \beta_z \quad (8)$$

β_k component is described by Scherrer relationship (8) (BOJARSKI, ŁĄGIEWKA 1988, CULLITY 1964):

$$\beta_k = \frac{K\lambda}{D_{hkl} \cos\Theta} \quad (9)$$

where:

K – Scherrer constant,

λ – X-ray wavelength,

D_{hkl} – average crystallite size (blocks) in a direction perpendicular to planes (hkl),

Θ – reflection angle,

hkl – Miller indices.

However β_z component of distortion resulting from lattice describes Taylor's relationship (10) (BOJARSKI, ŁĄGIEWKA 1988):

$$\beta_z = 4 \left\langle \frac{\Delta a}{a} \right\rangle \operatorname{tg} \theta \quad (10)$$

Taking into account dependence (9) and (10) equation for total actual broadening of diffraction peak becomes a (11) (BOJARSKI, ŁĄGIEWKA 1988):

$$\beta_r \cos \theta = \frac{K\lambda}{D} + 4 \left\langle \frac{\Delta a}{a} \right\rangle \sin \theta \quad (11)$$

By linear regression plotting relationship $\beta_r \cos \theta = f(\sin \theta)$ for several reflexes of same sample (best for several rows of reflections from same plane (hkl)) ordinate values can be determined crystallite size (mosaic blocks), while value of slope to determine distortion of lattice (stresses of second kind). Defined and further described X-ray parameters used in testing methods based on X-ray diffraction on crystal lattice can be found in papers (BOJARSKI, ŁAGIEWKA 1988, CULLITY 1964).

Research results and their analysis

Recorded during measurements of X-ray diffraction patterns (Fig. 2) and associated interdependence of reflection angles of particular diffraction reflexes clearly indicate presence of two structural components of regular lattice: ferrite (α) – with symmetry $I \frac{4}{m} \frac{3}{2}$ (space group 229) and austenite (γ) – with symmetry $F \frac{4}{m} \frac{3}{2}$ (space group 225).

Plotting relationship lattice parameters a_{hkl} , determined on basis of angular positions Bragg each reflexes, depending on value function N-R (described

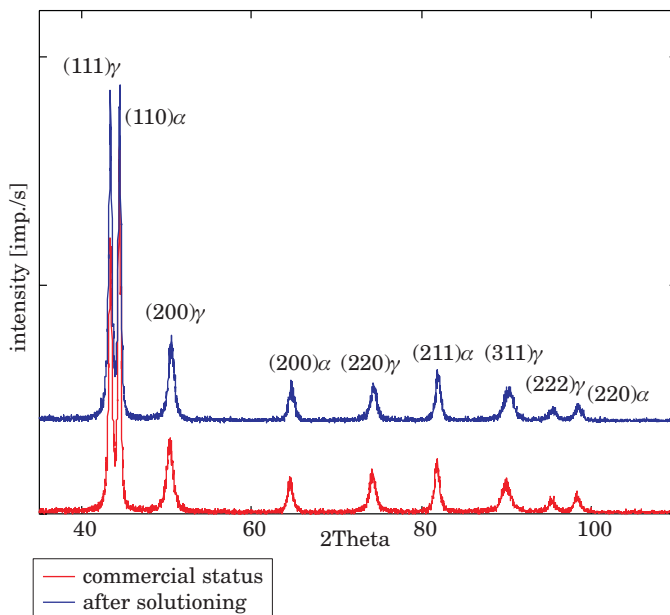


Fig. 2. Diffraction pattern of stainless steel X2CrNiMoN25-7-4: commercial status and after solutioning

by formula 3) and made linear extrapolation function N-R to a value corresponding to reflection angle θ equal 90 degree. Determined by method of extrapolation of lattice parameters of ferrite and austenite, α_0 are respectively: for commercial status 2.887 Å and 3.619 Å and after solutioning 2.882 Å and

Table 1
Summary of main parameters and XRD results for samples of stainless steel X2CrNiMoN25-7-4 in commercial status

Ferrite									
No.	hkl	2Θ	I	f_{sr}	p	LP	$ F_{hkl} ^2$	$\alpha_{0(\alpha)}$ [Å]	V_α [%]
1.	110	44.351	233	17.93	12	11.46	1285.4	2.887	46.72
2.	200	64.517	56	15.13	6	4.92	915.75		
3.	211	81.631	69	13.33	24	3.16	710.30		
4.	220	97.997	27	12.11	12	2.73	587.10		
Austenite									
No.	hkl	2Θ	I	f_{sr}	p	LP	$ F_{hkl} ^2$	$\alpha_{0(\gamma)}$ [Å]	V_γ [%]
1.	111	43.293	239	18.10	8	12.10	5244.1	3.619	53.28
2.	200	50.28	117	17.03	6	8.62	4642.1		
3.	220	74.09	57	14.04	12	3.71	3155.0		
4.	311	89.674	93	12.69	24	2.84	2575.0		
5.	222	95.088	18	12.31	8	2.74	2423.6		

Table 2
Summary of main parameters and XRD results for samples of stainless steel X2CrNiMoN25-7-4 after solutioning

Ferrite									
No.	hkl	2Θ	I	f_{sr}	p	LP	$ F_{hkl} ^2$	$\alpha_{0(\alpha)}$ [Å]	V_α [%]
1.	110	44.396	219	17.93	12	11.43	1285.4	2.882	44.91
2.	200	64.626	59	15.13	6	4.90	915.7		
3.	211	81.75	63	13.33	24	3.15	710.3		
4.	220	98.20	23	12.11	12	2.73	587.1		
Austenite									
No.	hkl	2Θ	I	f_{sr}	p	LP	$ F_{hkl} ^2$	$\alpha_{0(\gamma)}$ [Å]	V_γ [%]
1.	111	43.321	283	18.10	8	12.08	5244.1	3.607	55.09
2.	200	50.549	148	17.03	6	8.52	4642.1		
3.	220	74.303	56	14.04	12	3.70	3155		
4.	311	90.147	62	12.69	24	2.82	2575		
5.	222	95.33	20	12.31	8	2.74	2423.6		

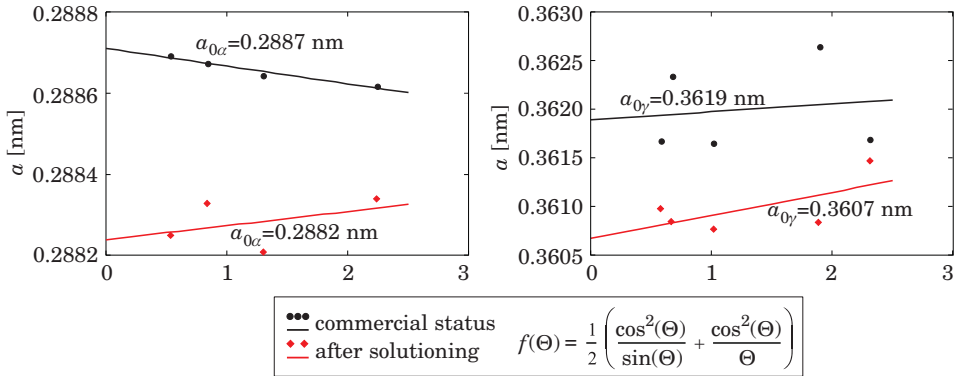


Fig. 3. Extrapolation of obtained lattice parameters: a – ferrite and b – austenite

Summary of size of mosaic blocks (D) and distortion lattice $\left\langle \frac{\Delta a}{a} \right\rangle$

Table 3

Commercial status				Solutioning			
Ferrite		Austenite		Ferrite		Austenite	
D	$\left\langle \frac{\Delta a}{a} \right\rangle$	D	$\left\langle \frac{\Delta a}{a} \right\rangle$	D	$\left\langle \frac{\Delta a}{a} \right\rangle$	D	$\left\langle \frac{\Delta a}{a} \right\rangle$
[Å]	[%]	[Å]	[%]	[Å]	[%]	[Å]	[%]
836	0.18	346	0.24	880	0.19	331	0.21

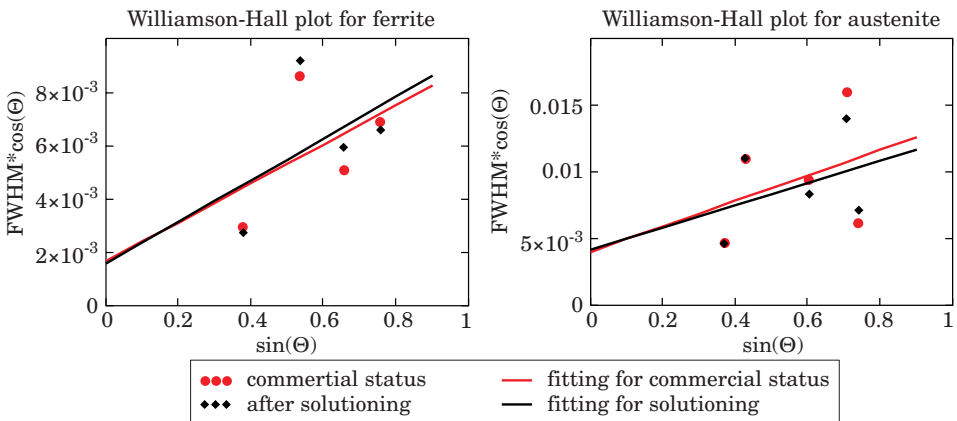


Fig. 4. Williamson-Hall plots for: a – ferrite, b – austenite

3.607 Å. Dependencies $a_{hkl} = f(N-R)$ shown in Figure 3. While detailed results of X-ray measurements and values of parameters necessary to carry out phase analysis are summarized in: table 1 and table 2.

Performed X-ray phase analysis of stainless steel samples X2CrNiMoN25-7-4 in commercial status and after solutioning gives similar results, both as to phase volume fraction and lattice parameters.

Also summarized in Table 3 size of mosaic blocks and distortions lattice derived from prepared Williamson-Hall plots (Fig. 4), show a similar degree of defects in crystal structure.

Conclusion

Obtained lattice parameters for austenite and ferrite in commercial alloy and after solutioning are similar, as well as other parameters analyzed.

Analysis of results allowed to determine:

- commercial stainless steel is shipped as solutioning,
- technological process of steel production in industrial conditions provide for its two-phase structure,
- used in production stage finishing treatments did not affect its structural parameters.

Translated by AUTORS

Accepted for print 7.09.2011

References

- BOJARSKI Z., GILA M., STRÓŻ K., SUROWIEC M. 2001. *Krystalografia. Podręcznik wspomagany komputerowo*. PWN Warszawa.
- BOJARSKI Z., BOLD T. 1970. *Rentgenograficzne metody wyznaczania zniekształceń sieciowych i wielkości bloków metali polikrystalicznych*. Prace Instytutów Hutniczych, 22.
- BOJARSKI Z., ŁĄGIEWKA E. 1988. *Rentgenowska analiza strukturalna*. Państwowe Wydawnictwo Naukowe, Warszawa.
- CULLITY B.D. 1964. *Podstawy dyfrakcji promieni rentgenowskich*. Państwowe Wydawnictwo Naukowe, Warszawa.
- LAI J.K.L., WONG K.W., LI D.J. 1995. *Effect of solution treatment on the transformation behaviour of cold-rolled duplex stainless steels*. Materials Science and Engineering, A203: 356–364.
- LEE S.C., KIM Y.H., LEE Y.D. 2002. *Analysis of creep deformation of type 2205 duplex stainless steel under continuous annealing conditions*. Journal of Materials Processing Technology, 123: 185–189.
- LIPIŃSKI T. 1993. *Analiza przyczyn pęknięcia stali 1H18N9T podczas walcowania*. Mechanika. Tom III. Wyższa Szkoła Inżynierska w Zielonej Górze. Zielona Góra, pp. 41–44.
- LIPIŃSKI T., SZABRACKI P., BRAMOWICZ M., RYCHLIK K. 2010. *Computer modelling Structural components of Duplex stainless steel*. Process innovation, Charper 5, Dniepropetrovsk, pp. 56–69.
- LIPSON H. 2001. *The study of metals and alloys by X-ray powder diffraction methods*. University College Cardiff Press.
- NOWACKI J. 2008. *Stal duplex i jej spawalność*. Przegląd Spawalnictwa, 10: 34–45.
- SENCZYK D. 1996. *Dyfraktometria rentgenowska w badaniach stanów naprężenia i własności sprężystych materiałów polikrystalicznych*. Wydawnictwo Politechniki Poznańskiej.

Reviewers

Janusz Badur, Marcin Barlik, Stanisław Borkowski, Jarosław Bosy,
Romana Cielątkowska, Bogusław Cieślikowski, Olgierd Jamroz,
Marek Łagoda, Stanisław Maciejewski, Czesław Suchocki,
Marek Szmytkiewicz, Robert Ulewicz